

UNIVERSITÉ DE LIÈGE



MATH0471 : MULTIPHYSICS INTEGRATED COMPUTATIONAL
PROJECT

CHRISTOPHE GEUZAINÉ
ROMAIN BOMAN

Heating of food in a microwave oven : coupling
of thermal and electromagnetic solvers

Anthony BOSCO
Armin BOSTEN
Michel HOUBART

Faculty of Applied Science
Master in Engineering Physics
Year 2017-2018

Contents

1	Electromagnetic solver	8
1.1	Numerical model and implementation	8
1.2	Electromagnetic solver validation	12
1.2.1	Stability criterion	13
1.2.2	Constant Electric Field E_y	13
1.2.3	Wave propagation in an homogeneous medium	15
1.2.4	1D Wave propagation in two different media	17
1.2.5	Standing wave	19
1.3	Performance	20
1.3.1	Strong scaling	20
1.3.2	Weak scaling	22
2	Heat equation solver	23
2.1	Numerical model and implementation	23
2.1.1	Discretization of the heat equation	24
2.1.2	Boundary conditions	25
2.2	Heat equation solver validation	27
2.2.1	Steady state heat equation across two different media	27
2.2.2	Transient heat conduction	29
2.2.3	Effects of a heat source	30
2.2.4	Spatial order of convergence of the numerical scheme	31
2.3	Temporal order of convergence	37
2.4	Stability analysis of the thermal solver	38
2.4.1	Test on an explicit solver ($\theta = 0$)	40
2.4.2	Test on an implicit solver ($\theta = 1$)	40
2.5	Performance	41
2.5.1	Strong scaling	41
2.5.2	Weak scaling	42
3	Coupled electromagnetic-thermal solver	43
3.1	Calculation of the dissipated power	44
3.2	Verification of the steady state	45
3.3	Phase transition	47
3.4	Implementation of the rotation	49
3.4.1	Rotation of the food	49
3.4.2	Solving of the problem after the rotation	50

3.5	Input field	56
4	Heating of realistic food	59
4.1	Unfrozen soup centered in the oven	59
4.2	Unfrozen soup not centred	65
4.3	Frozen soup	67
4.4	Heating of a chicken	72

List of Figures

1	Flow chart of the electromagnetic solver.	8
2	Positions of various field components. The E-components are in the middle of the edges and the H-components are in the center of the faces.	9
3	Representation of the spatial subdivision allocation to the various processes. . . .	10
4	Graphical illustration of the 1D CFL stability criterion. The orange area is the analytic domain of dependence. The blue area added to the orange area is the numerical domain of dependence.	13
5	Scheme of the test that was performed. Figure 6 gives the values along the cut shown in this figure.	14
6	Magnitude of the magnetic field H_z [T] on a cut along x for a constant electric field E_y of magnitude 2000 [V/m]. $L = 0.3$ [m], $\Delta x = 0.005$ [m], $\Delta t = 5 \cdot 10^{-12}$ [s] and $t = 5 \cdot 10^{-10}$ [s].	15
7	Representation of the 1D wave propagation problem.	15
8	Evolution of the y component of the electric field as a function of x for $y = 0.075$ [m] and $z = 0.075$ [m]. The snapshots have been taken after respectively 0.25 [ns], 0.5 [ns], 1 [ns] and 1.5 [ns]. The numerical parameters are: $dx = 0.005$ [m], $L = 0.6$ [m], $\ell = 0.15$ [m] and $dt = 5$ [ps].	16
9	Geometry of the two medias wave propagation problem.	17
10	Propagation of the electric field E_y in two media of different permittivity ($\epsilon_{r,1} = 1$ and $\epsilon_{r,2} = 9$) at the 1100 th timestep, with $\Delta t = 5$ ps.	18
11	Representation of the standing wave problem.	19
12	Amplitude of the electric field E_y [V/m] in function of the position along x [m]. The cut was made at $y = 0.07 = z$ [m]. Left: Results for $L = 0.5$ [m]; Right: Results for $L = 0.54$ [m]. Top: $t = 16000\Delta t + (i - 1)t_i$ [s]; Bottom: $t = 16006\Delta t + (i - 1)t_i$ [s] with $i = 1, 2, \dots, 5$. Numerical parameters: $\Delta x = 0.005$ [m] and $\Delta t = 5 \cdot 10^{-12}$ [m].	20
13	Speed up and efficiency curves of strong scaling for $N = 100$ and 300 time steps. $\Delta L = 0.005$ m and $\Delta t = 5 \times 10^{-12}$ s.	21
14	Speed up and efficiency curves of strong scaling for $N = 100$ and 300 time steps. $\Delta L = 0.005$ m and $\Delta t = 5 \times 10^{-12}$ s.	21
15	Flow chart of the heat equation solver.	24
16	Representation of a discretized interface between air and food.	26
17	Representation of the 3D steady state thermal problem without source across two different media.	27
18	Representation of the 1D steady state thermal problem without source across two different media.	27
19	Temperature field computed by the solver inside 2 adjacent cubic objects on a cut along the x axis. $L = 0.14$ [m], $\Delta t = 0.1$ [s] and $\Delta x = 0.05$ [m].	28

20	Representation of the 1D transient thermal problem without source in an homogeneous medium.	29
21	Comparison between numerical and analytic solution for the simple case of transient heat conduction. $L = 0.3[m]$, $\Delta t = 0.1[s]$, $\tau = 100[s]$ and $\Delta x = 0.01$. .	30
22	Comparison between numerical and analytic solution for the simple case of transient heat conduction. $L = 0.3[m]$, $\Delta t = 0.1[s]$ and $\Delta x = 0.01$	31
23	Representation of the geometry and of the boundary conditions of the heat transfer problem to be solved.	32
24	Comparison between the numerical and the exact steady state temperature profiles. The numerical parameters are : $k = 1 [W \cdot K^{-1} \cdot m^{-1}]$, $Q = 50000 [W \cdot m^{-3}]$, $L = 0.16 [m]$ and $dx = 0.01 [m]$	33
25	Evolution of the global error as a function of the grid spacing. The numerical parameters are : $k = 1 [W \cdot K^{-1} \cdot m^{-1}]$, $Q = 50000 [W \cdot m^{-3}]$, $L = 0.16 [m]$	34
26	Evolution of the temperature as a function of y for $x = 0.08 [m]$ for different value of the grid spacing. The numerical parameters are : $k = 1 [W \cdot K^{-1} \cdot m^{-1}]$, $Q = 50000 [W \cdot m^{-3}]$, $L = 0.16 [m]$	34
27	Comparison between the numerical and the exact steady state temperature profiles. The numerical parameters are : $k = 1 [W \cdot K^{-1} \cdot m^{-1}]$, $Q = 50000 [W \cdot m^{-3}]$, $L = 0.16 [m]$, $h = 1 [W \cdot m^{-2} \cdot K^{-1}]$ and $dx = 0.01 [m]$	35
28	Evolution of the global error as a function of the grid spacing. The numerical parameters are : $k = 1 [W \cdot K^{-1} \cdot m^{-1}]$, $Q = 50000 [W \cdot m^{-3}]$, $L = 0.16 [m]$, $h = 1 [W \cdot m^{-2} \cdot K^{-1}]$ and $dx = 0.01 [m]$	36
29	Evolution of the temperature as a function of y for $x = 0.08 [m]$ for different value of the grid spacing. The numerical parameters are : $k = 1 [W \cdot K^{-1} \cdot m^{-1}]$, $Q = 50000 [W \cdot m^{-3}]$, $L = 0.16 [m]$	36
30	Evolution of the global error as a function of the time step for both the implicit Euler and Crank–Nicholson methods.	38
31	Limit value of μ as a function of the parameter θ , according to EQ. 2.31.	39
32	Temperature as a function of time for two values of Δt when using an explicit solver ($\theta = 0$).	40
33	Temperature as a function of time for two values of Δt when using an explicit solver ($\theta = 1$).	41
34	MPI: Speed up and efficiency curves of strong scaling for $L = 0.3[m]$ and 500 time steps. $\Delta L = 0.01[m]$ and $\Delta t = 0.001[s]$	42
35	Flow chart of the coupled solver.	43
36	Evolution of the amplitude of the electric field as a function of time. The value of the complex permittivity is $75.8 + j 5$. The spatial and temporal steps were respectively equal to $5 [mm]$ and $5 \cdot 10^{-3} [ns]$	46
37	Solution of the uniform heat equation when the food undergoes phase change, with a constant heat source. — $Q = 50000 [W \cdot m^{-3}]$, $\rho_1 = 725 [kg \cdot m^{-3}]$, $c_{p,1} = 1450 [J \cdot K^{-1} \cdot kg^{-1}]$, $\rho_2 = 770 [kg \cdot m^{-3}]$, $c_{p,2} = 2770 [J \cdot K^{-1} \cdot kg^{-1}]$, $dt = 0.1 [s]$, $T_0 = -5 [^{\circ}C]$, $T_{\varphi} = 0.1795 [^{\circ}C]$	48
38	Solution of the uniform heat equation when the food undergoes phase change, with a constant heat source. — $Q = 50000 [W \cdot m^{-3}]$, $\rho_1 = 725 [kg \cdot m^{-3}]$, $c_{p,1} = 1450 [J \cdot K^{-1} \cdot kg^{-1}]$, $\rho_2 = 770 [kg \cdot m^{-3}]$, $c_{p,2} = 2770 [J \cdot K^{-1} \cdot kg^{-1}]$, $dt = 0.1 [s]$, $T_0 = -5 [^{\circ}C]$, $T_{\varphi} = 0 [^{\circ}C]$	49

39	Scheme depicting the method used to rotate the object inside the domain. $\mathbf{X} = [X \ Y]^T$ are the coordinates of point P in the reference configuration, whereas $\mathbf{x} = [x \ y]^T$ are the coordinates of point P in the current configuration. The angular displacement is denoted by θ . Here, P_1 is inside the food and P_2 is inside the air volume.	50
40	Representation of the rotation of the temperature inside a fixed thermal grid. $T^0(x, y, z)$ is the temperature field before rotation and $T^1(x, y, z)$ is the temperature field after rotation.	52
41	Representation of a cell of the thermal grid.	52
42	Representation of the rotation of the thermal grid. The black grid is the fixed electromagnetic grid, the red grid is the thermal one.	53
43	Initial temperature field for a cylinder whose axis is directed along the z direction and whose radius is equal to $0.05 [m]$. The domain is a cube of length equal $0.3[m]$ and the grid spacing is equal to $0.01[m]$	55
44	Temperature field for a cylinder whose axis is directed along the z direction and whose radius is equal to $0.05 [m]$ after a rotation of of $\frac{\pi}{2}$ radiant with a angular step of $\frac{\pi}{8}$ radiant. The domain is a cube of length equal $0.3[m]$ and the grid spacing is equal to $0.01[m]$	55
45	Temperature field for a cylinder whose axis is directed along the z direction and whose radius is equal to $0.05 [m]$ after a rotation of of 2π radiant with a angular step of $\frac{\pi}{8}$ radiant. The domain is a cube of length equal $0.3[m]$ and the grid spacing is equal to $0.01[m]$	56
46	Schematic of the wave guide. The end of the wave guide is placed on the wall of the microwave oven of coordinate $x = 0$	57
47	Representation of the geometry when the bowl of soup is centered inside the microwave oven.	60
48	Representation of the position where the temperature is evaluated inside the bowl of soup.	61
49	Representation of the temperature profile along the Cut X , without rotation, after respectively $75[s]$, $150[s]$, $225[s]$ and $300 [s]$ of simulation. The black line represent the aimed temperature level of $70^\circ[C]$	61
50	Representation of the temperature profile along the Cut Z , without rotation, after respectively $75[s]$, $150[s]$, $225[s]$ and $300 [s]$ of simulation. The black line represent the aimed temperature level of $70^\circ[C]$	62
51	Time evolution of the temperature at the temporal probe placed inside the soup without rotation.	63
52	Representation of the temperature profile along the Cut X , with a rotation of $\frac{2\pi}{5}$ radiant every $2.5[s]$, after respectively $75[s]$, $150[s]$, $225[s]$ and $300 [s]$ of simulation. The black line represent the aimed temperature level of $70^\circ[C]$	63
53	Representation of the temperature profile along the Cut Z , with a rotation of $\frac{2\pi}{5}$ radiant every $2.5[s]$, after respectively $75[s]$, $150[s]$, $225[s]$ and $300 [s]$ of simulation. The black line represent the aimed temperature level of $70^\circ[C]$	64
54	Time evolution of the temperature at the temporal probe placed inside the soup while considering a rotation of $\frac{2\pi}{5}$ radiant every $2.5[s]$	65

55	Representation of the geometry when the bowl of soup is not centred inside the microwave oven.	65
56	Representation of the temperature profile along the Cut X , with a rotation of $\frac{2\pi}{5}$ radiant every 2.5[s], after respectively 75[s], 150[s], 225[s] and 300 [s] of simulation. The black line represent the aimed temperature level of 70°C.	66
57	Representation of the temperature profile along the Cut Z , with a rotation of $\frac{2\pi}{5}$ radiant every 2.5[s], after respectively 75[s], 150[s], 225[s] and 300 [s] of simulation. The black line represent the aimed temperature level of 70°C.	67
58	Water and ice molecules under a vertical electric field. The red spheres are hydrogen atoms and the blue spheres are oxygen atoms. The dotted line represents the bonds between the molecules.	68
59	Representation of the temperature profile along the Cut X , with a rotation of $\frac{\pi}{5}$ radiant every 5[s], after respectively 75[s], 300[s], 512[s] and 600 [s] of simulation. The black line represent the aimed temperature level of 70°C.	69
60	Representation of the temperature profile along the Cut Z , with a rotation of $\frac{\pi}{5}$ radiant every 5[s], after respectively 75[s], 300[s], 512[s] and 600 [s] of simulation. The black line represent the aimed temperature level of 70°C.	70
61	Time evolution of the temperature at the temporal probe placed inside the soup while considering a rotation of $\frac{\pi}{5}$ radiant every 5[s].	71
62	Representation of the geometry and constitution of the chicken.	72
63	Temperature field at the surface and inside the chicken after a 300 [s] simulation.	73

List of Tables

1	Dimension of the different grids used to discretise the examined domain.	9
2	Electrical properties of the two medias used in the numerical simulation.	17
3	Performance analysis of the OpenMpi implementation: Weak scaling	22
4	Parameters used for the different tests concerning transient heat conduction.	29
5	Total run time: OpenMP for $L = 0.3[m]$ and 500 time steps. $\Delta L = 0.01[m]$ and $\Delta t = 0.001[s]$	42
6	Electromagnetic and thermal property of the soup placed in the microwave oven.	60
7	Order of magnitude of the electromagnetic and thermal properties of the soup placed in the microwave oven.	67
8	Electromagnetic and thermal properties of the fat, muscles and bones.	72
9	List of materials and their associated ID that is used in the input files	80

Introduction

Shortly after the second world war an American engineer called Percy Spencer invented the microwave oven. It was made possible by the development of the cavity magnetron. A device which has the ability to produce electromagnetic waves in the micrometer range. The first home use microwave oven, as we know it today, was introduced into the market in 1955 by the company *Tapan*, but its commercial success was hindered by the stove's large size and its high prize. Improvements on the original concept were made and since the beginning of the 1970's the modern microwave has found its way into most residential kitchens around the globe.

Microwave ovens are commonly used to reheat already cooked food or unfreeze. They perform well or less well depending on the shape, nature and position of the food placed inside their cavity. In this work food heating in a microwave oven is analysed. A numerical approach is chosen for this purpose.

The aim of the project is to build a numerical solver able to model the food heating in a microwave oven and use it in order to obtain relevant information on how a commercial microwave oven is best used.

There are two different physical disciplines involved: Electromagnetism and heat transfer. As it will be shown later in this work, electromagnetic quantities reach steady states in less than $1[\mu s]$, much faster than the typical time scales at which phenomena related to heat transfer occur. Therefore the two physics can be treated totally independently from each other until a final step, where the output of the electromagnetic solver is used as input for the heat equation solver. Moreover the rotational speed of the plate inside an oven is usually very slow. Therefore, the thermal computations are performed on a fixed grid and the resulting fields are rotated afterwards.

Using these two hypotheses enables the following four step approach for the construction of the complete solver: Firstly, the implementation and the validation on simple 1D configurations of an electromagnetic solver using the Finite Difference Time Domain method. Secondly, the implementation and the validation on simple 1D configurations of a heat equation solver using a Crank-Nicholson Finite Difference scheme. Thirdly, the handling of the food rotation. And finally, the coupling of both solvers.

The last part of this document is dedicated to the study of more complex 3D configurations using the fully operational solver. First, we will look at the heating of a bowl of soup. The influence of the initial physical state and its position inside the cavity is analysed. Then, the solver's ability to deal with complex geometries is displayed by simulating the cooking of a chicken with the use of a microwave oven.

Chapter 1

Electromagnetic solver

The first part of the development of a coupled thermal-electromagnetic solver consists in building a parallel solver with MPI and OpenMP that is able to solve Maxwell's equations in three dimensions. In particular, in the framework of a microwave oven, the equations have to be solved in a rectangular cavity surrounded by perfectly conducting walls.

First, the discretization of Maxwell's equations and the implementation are described. Then, the validity of the solver is discussed by evaluating the quality of the numerical results obtained for simple cases. Finally, the parallel performance of the solver is assessed using strong and weak scaling.

1.1 Numerical model and implementation

In this section, a brief description of the implementation and features is presented. First of all, the general structure of the electromagnetic solver is shown in FIGURE 1:

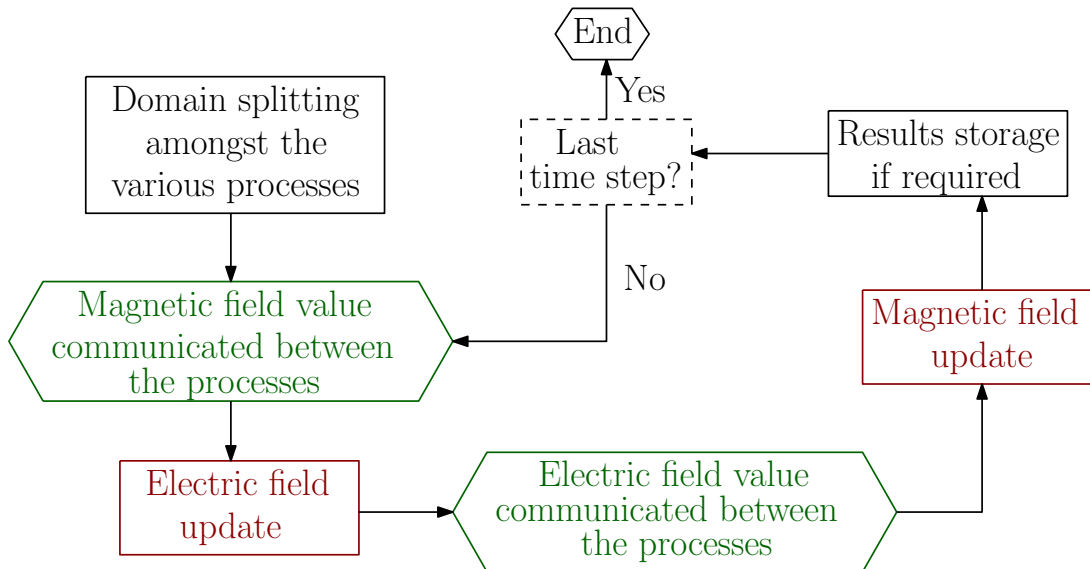


Figure 1: Flow chart of the electromagnetic solver.

As it can be seen in FIGURE 1, the first step is to define a discretization of the space. In this application, a cubic grid with a spacing dx is used for each component of the two fields of

interest. However, due to the form of the equation that has to be solved, it can be shown that each component of each field has to be computed at different locations than all the others. For this reason six different cubic grids have to be used to solve the electromagnetic problem.

Let us denote Lx , Ly and Lz the length of the spatial domain respectively in the x , y and z direction. Therefore, the exact dimensions of the six aforementioned grids are given in TABLE 1:

		Number of points		
		x direction	y direction	z direction
Fields	E_x	$\left(\frac{Lx}{dx}\right) + 2$	$\left(\frac{Ly}{dy}\right) + 1$	$\left(\frac{Lz}{dz}\right) + 1$
	E_y	$\left(\frac{Lx}{dx}\right) + 1$	$\left(\frac{Ly}{dy}\right) + 2$	$\left(\frac{Lz}{dz}\right) + 1$
	E_z	$\left(\frac{Lx}{dx}\right) + 1$	$\left(\frac{Ly}{dy}\right) + 1$	$\left(\frac{Lz}{dz}\right) + 2$
	H_x	$\left(\frac{Lx}{dx}\right) + 1$	$\left(\frac{Ly}{dy}\right) + 2$	$\left(\frac{Lz}{dz}\right) + 2$
	H_y	$\left(\frac{Lx}{dx}\right) + 2$	$\left(\frac{Ly}{dy}\right) + 1$	$\left(\frac{Lz}{dz}\right) + 2$
	H_z	$\left(\frac{Lx}{dx}\right) + 2$	$\left(\frac{Ly}{dy}\right) + 2$	$\left(\frac{Lz}{dz}\right) + 1$

Table 1: Dimension of the different grids used to discretise the examined domain.

More visually, the position at which the various components of the two fields are evaluated is represented in FIGURE 2:

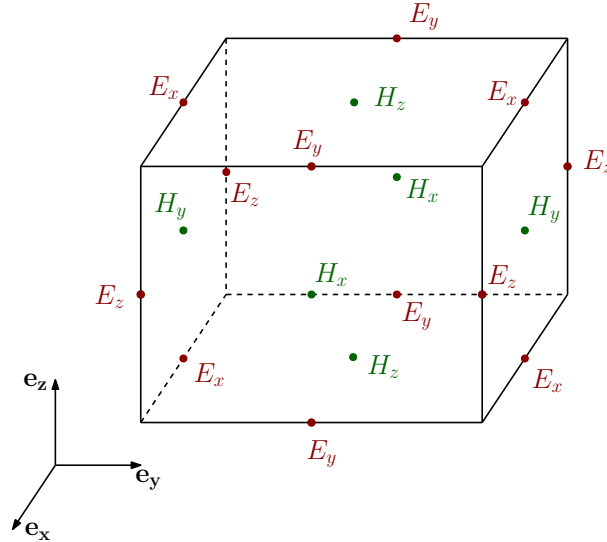


Figure 2: Positions of various field components. The E-components are in the middle of the edges and the H-components are in the center of the faces.

The spatial domain is then partitioned in subdivisions to run parallel computing. Each subdivisions are dedicated to a specific process allowing the corresponding fields value to be updated independently from the other processes. The domain subdivision is achieved by introducing three numbers, respectively noted $divx$, $divy$ and $divz$. These numbers are obtained

by decomposing the number of processes used into prime numbers and then forming the smallest combination of those prime numbers. As an example, the use of 24 processes will lead to $divx = 6$, $divy = 2$ and $divz = 2$. Therefore, each direction of the space can be split into respectively $divx$, $divy$ and $divz$ subdivisions.

Following the above, indices ip , jp and kp are created and range respectively from 0 to $divx - 1$, from 0 to $divy - 1$ and from 0 to $divz - 1$. These indices are used to identify the different spatial regions just created. Therefore, a process whose rank is equal to $myrank$ can determine the region of the space it has to handle by computing the value of ip , jp and kp using the following equations:

$$\begin{cases} ip = \frac{myrank}{divy \cdot divz}, \\ jp = (myrank \pmod{(divy \cdot divz)}) \pmod{divy}, \\ kp = \frac{myrank \pmod{(divy \cdot divz)}}{divy}, \end{cases} \quad (1.1)$$

where $\pmod{}$ is the modulo operator.

The result of this spatial domain split is shown in FIGURE 3:

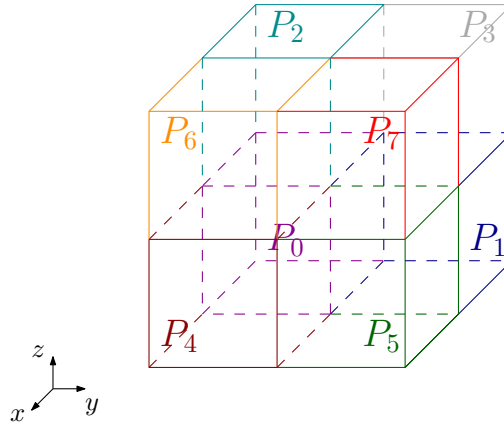


Figure 3: Representation of the spatial subdivision allocation to the various processes.

Once the spatial domain is split, each process will be able to perform a loop over several time steps to compute the evolution of the various field components. This computation is carried out by using a finite difference formulation of Maxwell's equations in which the current density has been neglected. Indeed, in the implementation the following equations have been used [1]:

$$\begin{cases}
 Ex_{i+\frac{1}{2},j,k}^{n+1} = \frac{dt}{\varepsilon \cdot dx} \left[\left(Hz_{i+\frac{1}{2},j+\frac{1}{2},k}^{n+\frac{1}{2}} - Hz_{i+\frac{1}{2},j-\frac{1}{2},k}^{n+\frac{1}{2}} \right) - \left(Hy_{i+\frac{1}{2},j,k+\frac{1}{2}}^{n+\frac{1}{2}} - Hy_{i+\frac{1}{2},j,k-\frac{1}{2}}^{n+\frac{1}{2}} \right) \right] + Ex_{i+\frac{1}{2},j,k}^n, \\
 Ey_{i,j+\frac{1}{2},k}^{n+1} = \frac{dt}{\varepsilon \cdot dx} \left[\left(Hx_{i,j+\frac{1}{2},k+\frac{1}{2}}^{n+\frac{1}{2}} - Hx_{i,j+\frac{1}{2},k-\frac{1}{2}}^{n+\frac{1}{2}} \right) - \left(Hz_{i+\frac{1}{2},j+\frac{1}{2},k}^{n+\frac{1}{2}} - Hz_{i-\frac{1}{2},j+\frac{1}{2},k}^{n+\frac{1}{2}} \right) \right] + Ey_{i,j+\frac{1}{2},k}^n, \\
 Ez_{i,j,k+\frac{1}{2}}^{n+1} = \frac{dt}{\varepsilon \cdot dx} \left[\left(Hy_{i+\frac{1}{2},j,k+\frac{1}{2}}^{n+\frac{1}{2}} - Hy_{i-\frac{1}{2},j,k+\frac{1}{2}}^{n+\frac{1}{2}} \right) - \left(Hx_{i,j+\frac{1}{2},k+\frac{1}{2}}^{n+\frac{1}{2}} - Hx_{i,j-\frac{1}{2},k+\frac{1}{2}}^{n+\frac{1}{2}} \right) \right] + Ez_{i,j,k+\frac{1}{2}}^n, \\
 Hx_{i,j-\frac{1}{2},k-\frac{1}{2}}^{n+\frac{1}{2}} = \frac{dt}{\mu \cdot dx} \left[\left(Ey_{i,j-\frac{1}{2},k}^n - Ey_{i,j-\frac{1}{2},k-1}^n \right) - \left(Ez_{i,j,k-\frac{1}{2}}^n - Ez_{i,j-1,k-\frac{1}{2}}^n \right) \right] + Hx_{i,j-\frac{1}{2},k-\frac{1}{2}}^{n-\frac{1}{2}}, \\
 Hy_{i-\frac{1}{2},j,k-\frac{1}{2}}^{n+\frac{1}{2}} = \frac{dt}{\mu \cdot dx} \left[\left(Ez_{i,j,k-\frac{1}{2}+\frac{1}{2}}^n - Ez_{i-1,j,k-\frac{1}{2}}^n \right) - \left(Ex_{i-\frac{1}{2},j,k}^n - Ex_{i-\frac{1}{2},j,k-1}^n \right) \right] + Hy_{i-\frac{1}{2},j,k-\frac{1}{2}}^{n-\frac{1}{2}}, \\
 Hz_{i-\frac{1}{2},j-\frac{1}{2},k}^{n+\frac{1}{2}} = \frac{dt}{\mu \cdot dx} \left[\left(Ex_{i-\frac{1}{2},j,k}^n - Ex_{i-\frac{1}{2},j-1,k}^n \right) - \left(Ey_{i,j-\frac{1}{2},k}^n - Ey_{i-1,j-\frac{1}{2},k}^n \right) \right] + Hz_{i-\frac{1}{2},j-\frac{1}{2},k}^{n-\frac{1}{2}},
 \end{cases} \quad (1.2)$$

where ε and μ are respectively the permittivity and the permeability of the considered medium and dt is the time step.

It should be highlighted that in these equations, the electric permittivity is always assessed at the same spatial location than the component of the electric field that is being updated. Therefore, if one considers a domain in which the electric permittivity can vary spatially, three different grids will be required to discretize it. Indeed, it results from the fact that the different electric field components are assessed at different locations as previously mentioned. The same comment can be made concerning the magnetic permeability. Nevertheless, in the framework of this project, only non magnetic materials will be placed inside the domain. Consequently, the magnetic permeability can be set to the value corresponding to vacuum everywhere in the domain.

Besides that, it should also be noticed that the suppression of the current density term in Maxwell's equations is equivalent to neglecting the dissipation of the electromagnetic energy. A further improvement of the solver could be obtained by keeping this term in the equations of update as shown in the Appendix 1.

As previously mentioned, using the equations (1.2), each process will be able to update the value of the fields inside the spatial division that was allocated to them. However, a communication between the processes is required in order to update the fields at the boundaries between the spatial subdivisions. To show that, the update of the electric field x component on the process whose rank is denoted by *myrank* is considered. In particular, focussing on the update of $Ex_{i+\frac{1}{2},j_{max},k}^{n+1}$, where j_{max} stands for the points having the largest y component in the spatial subdivision attributed to the considered process. From the first equation in 1.2 it can be deduced that this update requires the value of $Hx_{i+\frac{1}{2},j_{max}+\frac{1}{2},k}^{n+\frac{1}{2}}$ to be performed. However, as the grid corresponding to Hx on a given process stops at the index $j_{max} - \frac{1}{2}$, a communication with the process *myrank* + 1 is performed to obtain the required information. Similarly, it can be shown that the following communications are also required in order to update the electric field:

- Communication with the process *myrank* + 1 to obtain the value of $Hx_{i,j_{max}+\frac{1}{2},k+\frac{1}{2}}^{n+\frac{1}{2}}$.
- Communication with the process *myrank* + *divy* to obtain the value of $Hx_{i,j+\frac{1}{2},k_{max}+\frac{1}{2}}^{n+\frac{1}{2}}$.

and $Hy_{i+\frac{1}{2},j,k_{max}+\frac{1}{2}}^{n+\frac{1}{2}}$.

- Communication with the process $myrank + divy \cdot divz$ to obtain the value of $Hy_{i_{max}+\frac{1}{2},j,k+\frac{1}{2}}^{n+\frac{1}{2}}$ and $H_{i_{max}+\frac{1}{2},j+\frac{1}{2},k}^{n+\frac{1}{2}}$.

A similar reasoning can also be performed in order to show that a communication between the processes is also required before updating the magnetic field. Indeed, the process whose rank is denoted by $myrank$ will perform the following communications:

- Communication with the process $myrank - 1$ to obtain the value of $Ex_{i-\frac{1}{2},-1,k}^n$ and $Ez_{i,-1,k-\frac{1}{2}}^n$.
- Communication with the process $myrank - divy$ to obtain the value of $Ex_{i-\frac{1}{2},j,-1}^n$ and $Ey_{i,j-\frac{1}{2},-1}^n$.
- Communication with the process $myrank - divy \cdot divz$ to obtain the value of $Ey_{-1,j-\frac{1}{2},k}^n$ and $Ez_{-1,j,k-\frac{1}{2}}^n$.

Besides, it can also be noticed in the system of equations 1.2 that the electric and the magnetic fields have to be computed at different instants in time. This is the reason why in FIGURE 1 the communication for the updated magnetic field is performed first, then the electric field is updated, next the communication for the updated electric field is carried out and finally the magnetic field is updated.

After that, perfectly conducting walls are assumed as boundary conditions of the electromagnetic problem. These boundary conditions consist in imposing on each boundary a zero value for the components of the electric field parallel to this boundary.

Finally, it can be noticed that the electromagnetic calculation continues until reaching the final time step. The determination of this last time step consists in verifying if a steady state configuration has been reached. This verification will be further discussed in the part concerning the coupling between the solvers.

1.2 Electromagnetic solver validation

Before considering complex cases such as the propagation of electromagnetic waves inside a loaded microwave oven the quality of the solver is at first evaluated.

Firstly, the condition required to obtain a stable numerical scheme will be exposed and discussed.

Then, the quality of the numerical results provided by the solver for simple configurations will be assessed. The electrical field will be first imposed constant and unidirectional along a

line in the domain. This will enable to recover basic physical phenomena : a magnetic field should encircle the wire, and should decay as $\frac{1}{r}$ (with r being the distance from the wire). Then, the propagation of an electromagnetic wave will be looked at in both homogeneous and non homogeneous domain.

1.2.1 Stability criterion

To ensure the stability of the numerical scheme a relation between the time step Δt and the grid spacing Δx has to be satisfied. It ensures that over one increment the electromagnetic field does not vary in a significant way. A necessary convergence criterion is given by the Courant-Friedrichs-Lewy condition. It expresses the fact that the analytic domain of dependence has to be included in the numerical domain of dependence to ensure that the method has access to the information required. For the explicit scheme used in our work and considering the identical grid spacing in each direction, the condition becomes:

$$\sqrt{3}\Delta x > c\Delta t, \quad (1.3)$$

c is the speed of light in the considered medium. A schematic depiction of this condition in 1D is given in figure 4.

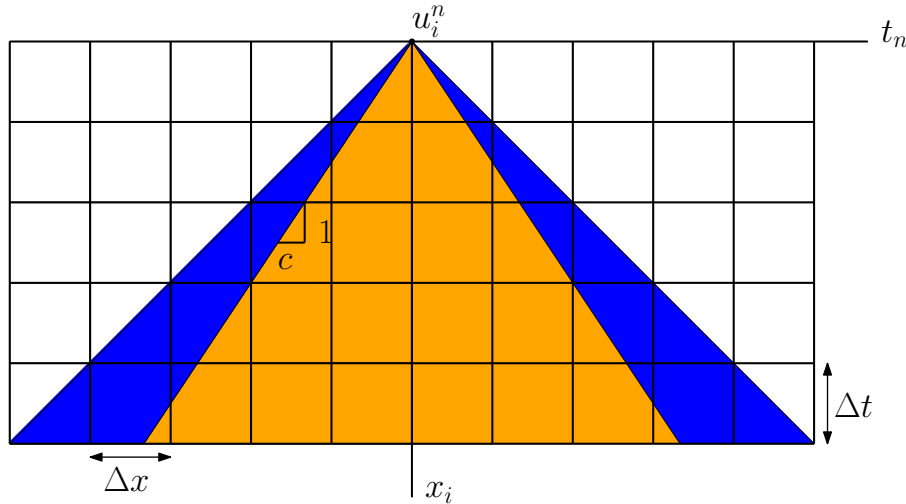


Figure 4: Graphical illustration of the 1D CFL stability criterion. The orange area is the analytic domain of dependence. The blue area added to the orange area is the numerical domain of dependence.

Starting from a set of Δt and Δx for which the implementation converges and then increasing Δt until the stability condition was not verified anymore. In fact, the implementation stopped being stable before reaching the equality in equation 1.3, thus suggesting that it is indeed a necessary condition for convergence, but not a sufficient one.

1.2.2 Constant Electric Field E_y

The first test that was run is the case of a constant electric field E_y of magnitude 2000 [V/m] going through a wire, located at $x = 0.14$ [m] of dimension $\ell = 0.3$ [m] with a grid spacing $\Delta x = 0.005$ [m] (60 grid points). A scheme is given in figure 5.

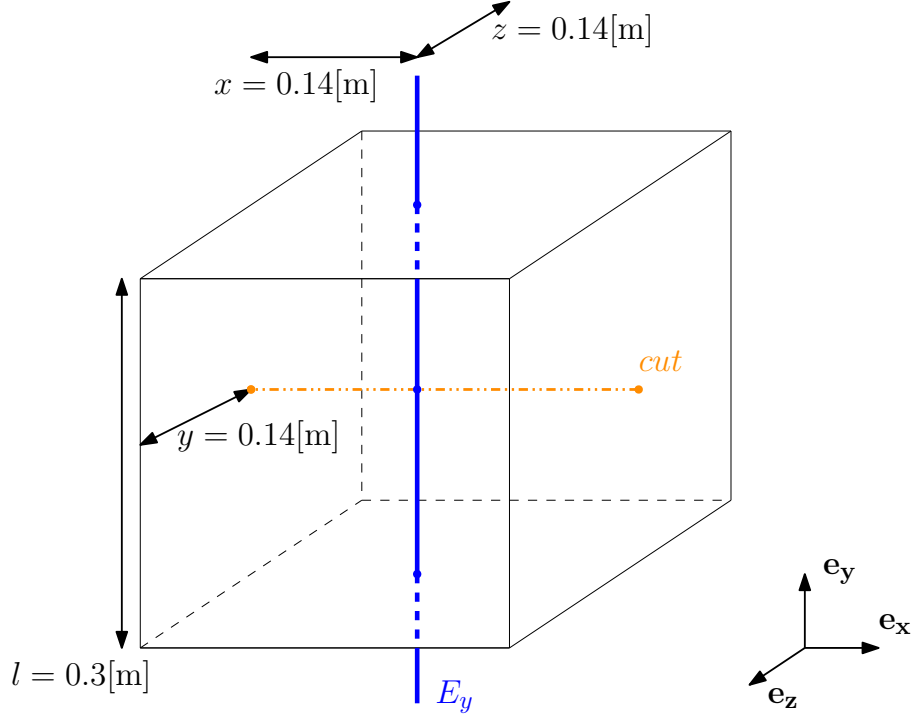


Figure 5: Scheme of the test that was performed. Figure 6 gives the values along the cut shown in this figure.

The resulting electromagnetic waves are free to propagate in the medium (vacuum with $\epsilon = \epsilon_0$ and $\mu = \mu_0$). The z component of the magnetic field should encircle the wire. Moreover the intensity of the field has to decay as $\frac{1}{R}$ where r is the distance from the wire. This is observed on a cut along the x axis as shown in figure 6.

It should be noted that the magnetic field is created by the change of the electric field from $t = 0[s]$ to $t = \Delta t[s]$. This phenomenon is described by Ampère's circuital law with Maxwell's addition that writes:

$$\nabla \times \mathbf{H} = \frac{\partial \epsilon \mathbf{E}}{\partial t}. \quad (1.4)$$

Integrating over a disc perpendicular to the wire centred in the wire and using Green's theorem yields

$$\oint_l \mathbf{H} \cdot d\vec{l} = \epsilon \frac{\partial}{\partial t} \iint_S \mathbf{E} \cdot d\vec{S}. \quad (1.5)$$

In the present case equation 1.5 becomes

$$2\pi R H_z = \epsilon \Delta x^2 \frac{\partial}{\partial t} (E_y), \quad (1.6)$$

such that

$$H_z = \frac{\epsilon \Delta x^2}{2\pi R} \frac{\partial}{\partial t} (E_y), \quad (1.7)$$

which decays as $\frac{1}{R}$ as announced.

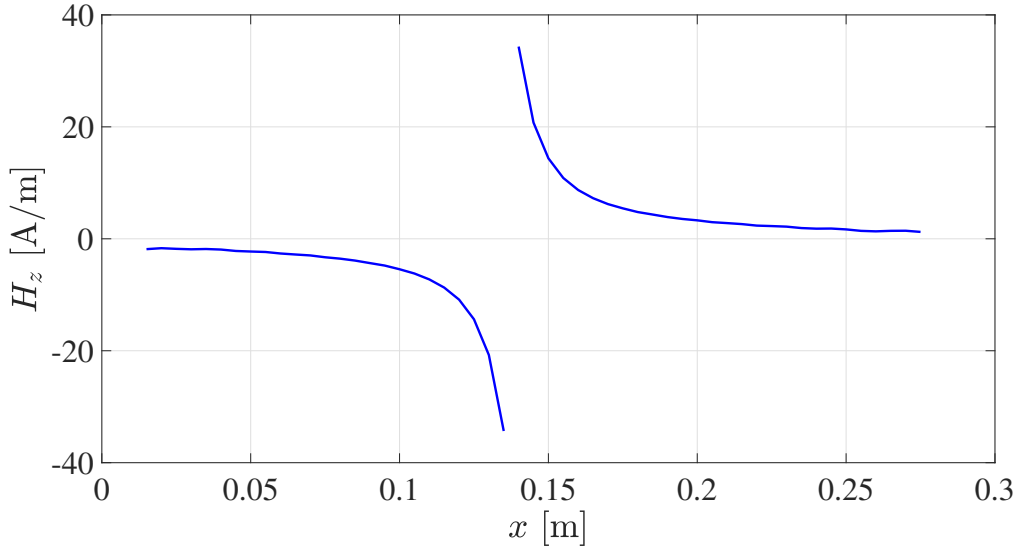


Figure 6: Magnitude of the magnetic field H_z [T] on a cut along x for a constant electric field E_y of magnitude 2000 [V/m]. $L = 0.3$ [m], $\Delta x = 0.005$ [m], $\Delta t = 5 \cdot 10^{-12}$ [s] and $t = 5 \cdot 10^{-10}$ [s].

1.2.3 Wave propagation in an homogeneous medium

The second test carried out to verify the quality of the electromagnetic solver consists in the propagation of a plane electromagnetic wave in a homogeneous medium. Indeed, the domain of interest is parallelepipedic and the y component of the electric field is imposed on a boundary of the domain as shown in FIGURE 7:

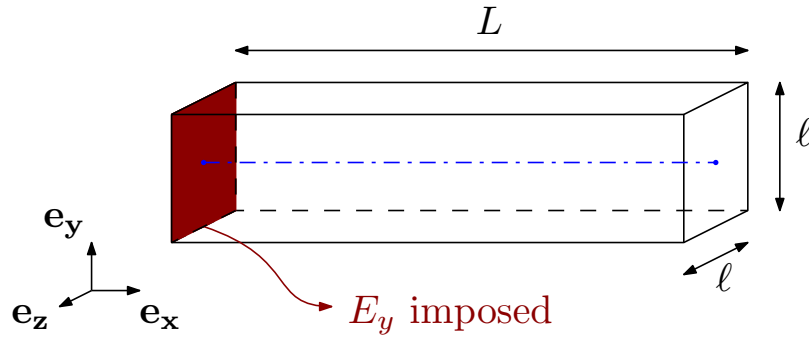


Figure 7: Representation of the 1D wave propagation problem.

The imposed component of the electric field is forced to evolve as follows:

$$E_y = E_0 \sin\left(\frac{\pi z}{\ell}\right) \sin(2\pi f t), \quad (1.8)$$

where the frequency f is fixed to 2.4 [GHz] and the amplitude E_0 is fixed to 100 [V⁻¹]. As it will be discussed in chapter 3, this form of the electric field corresponds to the evolution that can be found at a fixed location in a wave guide for which only the first mode is excited. The considered problem is therefore equivalent to the simulation of the first excited mode propagation along a wave guide.

The solver was used to compute the value of the y component of the electric field along the blue line shown in FIGURE 7 for different time. The obtained results are shown in FIGURE 8.

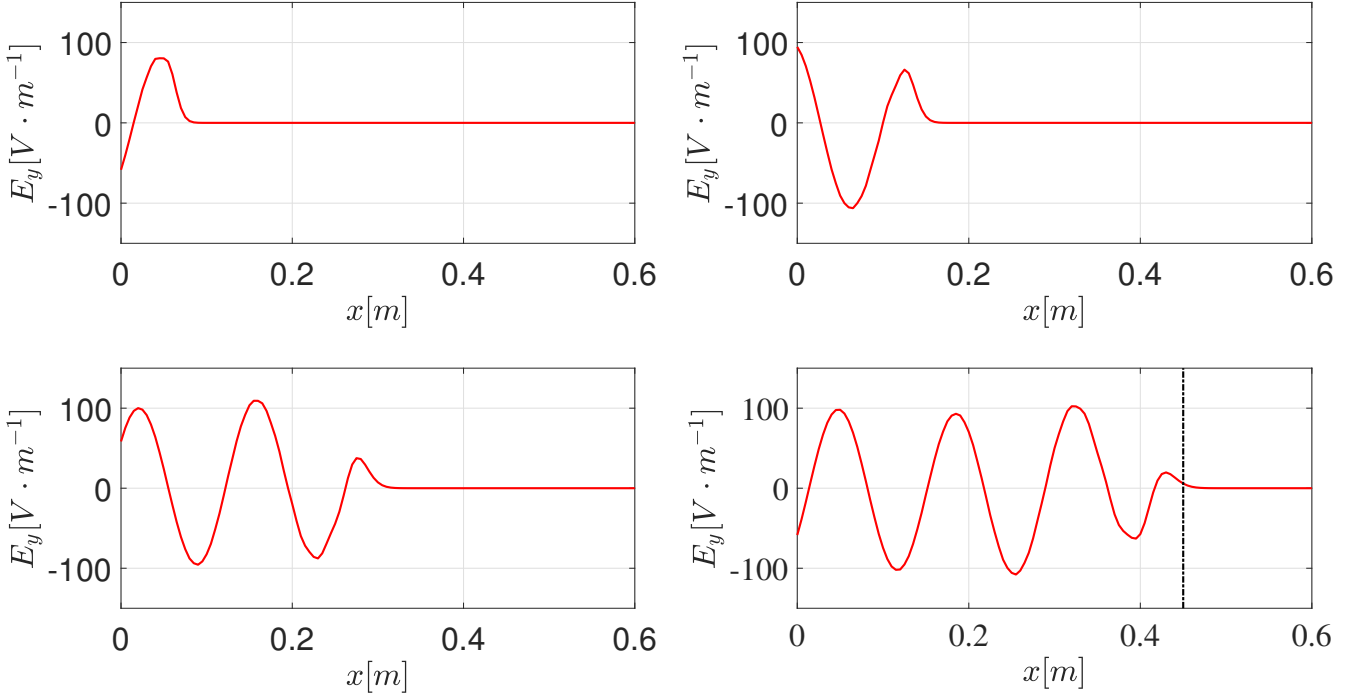


Figure 8: Evolution of the y component of the electric field as a function of x for $y = 0.075 \text{ [m]}$ and $z = 0.075 \text{ [m]}$. The snapshots have been taken after respectively 0.25 [ns] , 0.5 [ns] , 1 [ns] and 1.5 [ns] . The numerical parameters are: $dx = 0.005 \text{ [m]}$, $L = 0.6 \text{ [m]}$, $\ell = 0.15 \text{ [m]}$ and $dt = 5 \text{ [ps]}$.

It can be seen in FIGURE 8, that the wave travels as expected. Indeed, the wave length obtained numerically is equal to 0.135 [m] which is close to the expected one (0.125 [m]). Besides this, two small numerical problems should be highlighted. The first one is that by comparing the two last snapshots in FIGURE 8, it can be noticed that the amplitude of the signal decreases as the wave propagates. This dissipation is necessarily numerical as no physical dissipation has been implemented in the solver. Besides this, after 1.5 [ns] , the wave is theoretically expected to have travelled 0.45 [m] . Therefore, the fourth snapshot in FIGURE 8 highlights that the wave is propagating slightly faster than expected.

1.2.4 1D Wave propagation in two different media

An key functionality of the solver is the ability the solve Maxwell's equation for an electromagnetic wave propagating in two medias. Indeed, when considering food inside the microwave, there will be at least two medias in the cavity, air and food. In this section, the propagation of a sinusoidal wave, one one dimension, inside two medias will be studied. The geometry of the problem can be seen in FIGURE 9. The antenna emits an electric field $E_y = E_0 \sin\left(\frac{\pi z}{\ell}\right) \sin(2\pi f t)$ of amplitude $E_0 = 1$ [V/m] at a frequency $f = 2.4$ [GHz]. The grid spacing was chosen such that $\Delta x = 0.005$ m and $\Delta t = 5$ ps. The cavity in FIGURE 9 is 0.8 m meter long while the width and height measure 0.4 m.

Medium 1		Medium 2	
ε_r	1 [—]	ε_r	9 [—]
μ_r	1 [—]	μ_r	1 [—]
ℓ	0.4 [m]	ℓ	0.4 [m]

Table 2: Electrical properties of the two medias used in the numerical simulation.

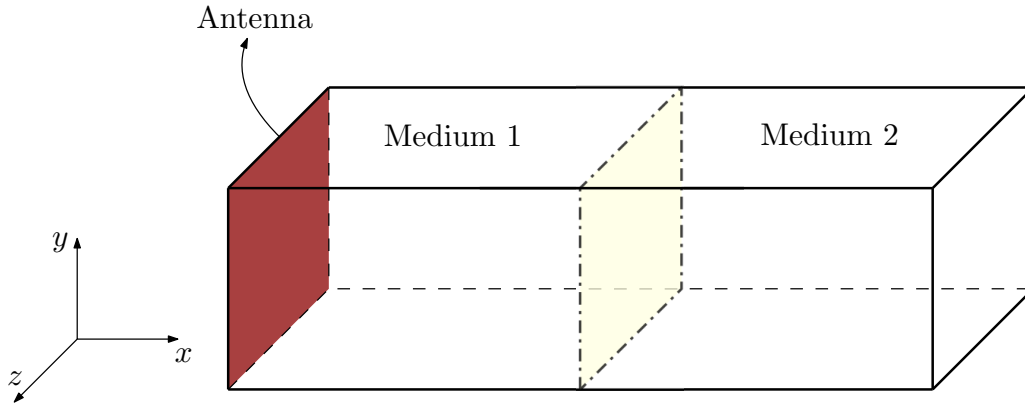


Figure 9: Geometry of the two medias wave propagation problem.

Theoretically, the speed of propagation is given by

$$v = \frac{c}{\sqrt{\epsilon_r \mu_r}},$$

where c is the speed of light in vacuum. In the first medium, the wave will be propagating at $v_1 = c$, and $v_2 = \frac{c}{3}$ in the second. Since the wavelength is defined as

$$\lambda = \frac{v}{f},$$

it is expected that the wavelength in the second medium will be three times smaller than in the first. Hence, since the wave is propagating 0.4 m in both cases, there should be three times more wavelength in the second medium.

FIGURE 10 shows the results obtained numerically.

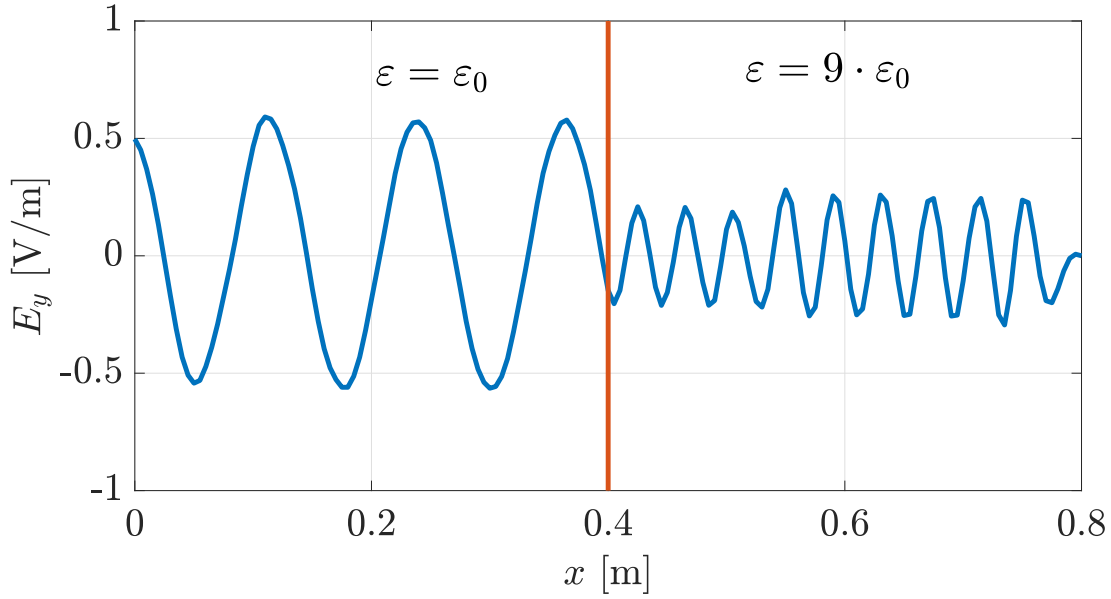


Figure 10: Propagation of the electric field E_y in two media of different permittivity ($\epsilon_{r,1} = 1$ and $\epsilon_{r,2} = 9$) at the 1100th timestep, with $\Delta t = 5$ ps.

In the first medium, the wavelength is $\lambda_1 = 0.125$ m, and $\lambda_2 = 0.0417$ m, which seems relatively close to what is shown in FIGURE 10. Moreover, there should be approximately 3.2 wavelengths in the first medium, and 9.6 in the second, which seems to fit to the numerical result.

1.2.5 Standing wave

A last numerical experiment was performed in order to confirm that the code represents the physics of electromagnetic wave propagation inside a cavity with perfectly conducting walls. A planar antenna filling out the whole cavity of dimensions $L_y = L_z = 0.15[\text{m}]$ and $L_x = 0.5[\text{m}]$ was placed on the left boundary, perpendicular to the x axis. It generates a sinusoidal electric field E_y with a frequency of $2.4 [\text{GHz}]$ as given in equation 1.8. Figure 11 illustrates the test that was performed.

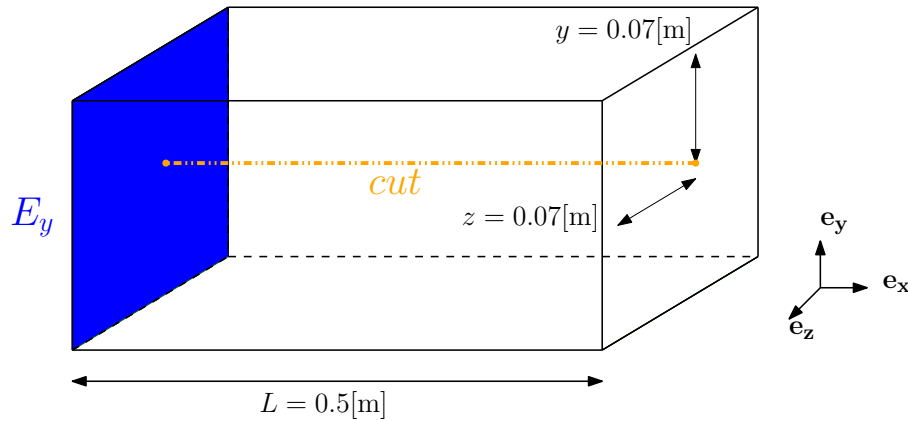


Figure 11: Representation of the standing wave problem.

Inside air the real wavelength is approximately 0.125m which is exactly one fourth of the cavity's length. A standing wave with the same wavelength is expected. The results of the simulation are shown in FIGURE 12.

The numerical wavelength obtained is $0.143[\text{m}]$. This is due to dispersion errors of the method, as well as the wave having to meet $E_y(x = L) = 0$. The wavelength obtained numerically for the wave propagating in free space was $0.135[\text{m}]$. The same experiment was repeated using a cavity of length $L = 0.54[\text{m}]$ which is exactly four times $0.135[\text{m}]$. The right graph in Figure 12 shows this second result.

As it can be observed, in the case where $L = 0.5[\text{m}]$ the nodes of the wave are not immobile. Thus the wave is not really stationary. On the other hand, using a cavity length in accordance with the numerical wavelength gives rise to a standing wave, where nodes and anti-nodes remain in the same location.

Furthermore, the amplitudes do not correspond. This is not surprising since propagation speed is the same in both numerical experiments, but the dimensions of the cavity are different. Obviously, not the same interference patterns appear.

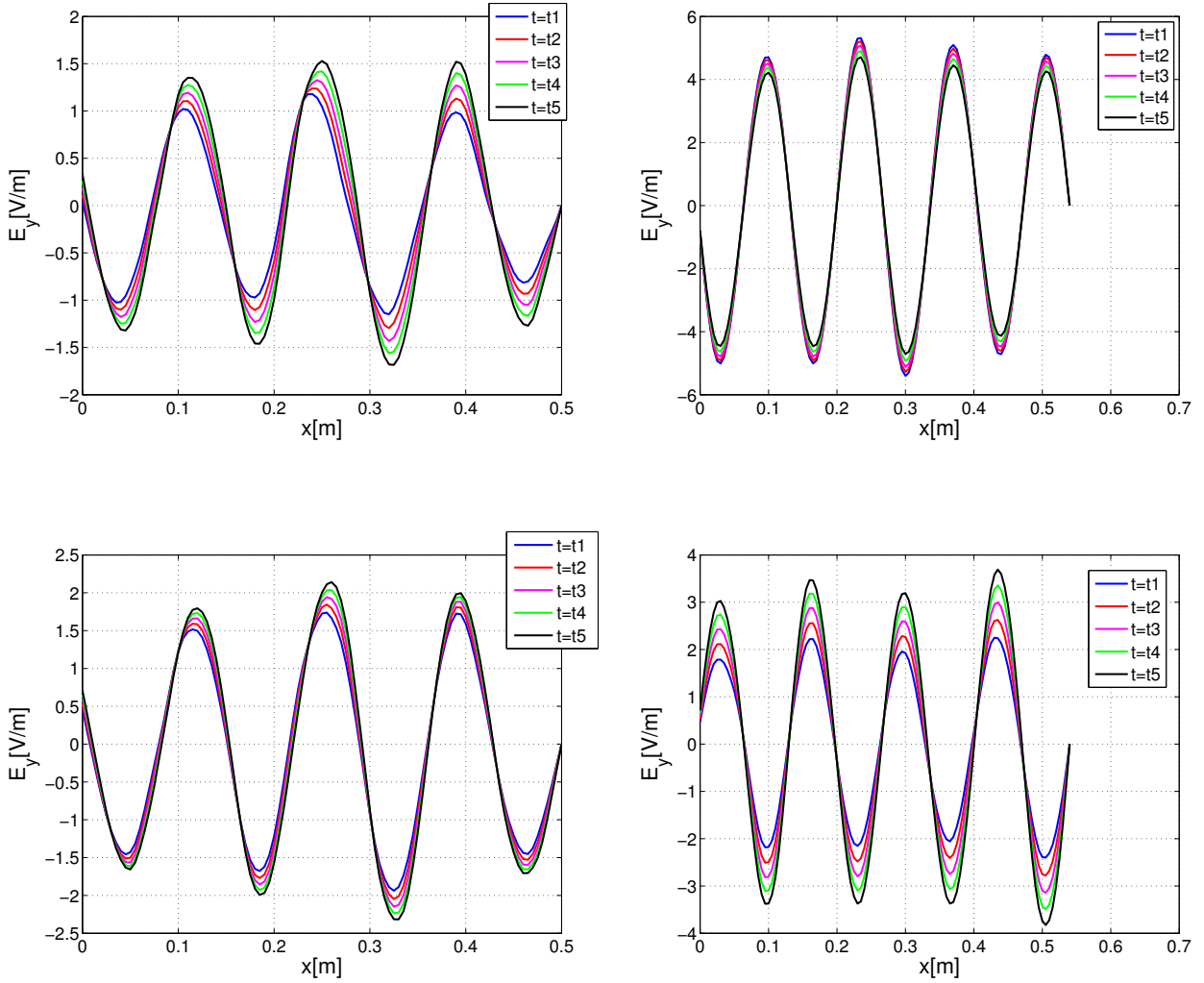


Figure 12: Amplitude of the electric field E_y [V/m] in function of the position along x [m]. The cut was made at $y = 0.07 = z$ [m]. Left: Results for $L = 0.5$ [m]; Right: Results for $L = 0.54$ [m]. Top: $t = 16000\Delta t + (i - 1)t_i$ [s]; Bottom: $t = 16006\Delta t + (i - 1)t_i$ [s] with $i = 1, 2, \dots, 5$. Numerical parameters: $\Delta x = 0.005$ [m] and $\Delta t = 5 \cdot 10^{-12}$ [m].

1.3 Performance

In this section speed up, efficiency and weak scaling of the electromagnetic implementation are analyzed. The standard test for strong scaling uses a mesh of dimensions N^3 with $N = 100$, where N is the number of points in one direction. This corresponds to a box with the following dimensions: $L_x = L_y = L_z = 0.5$ m and $\Delta L = 0.005$ m. The time step is fixed at 5×10^{-12} [s] such that it satisfies the CFL condition of the numeric scheme. Weak scaling is checked by keeping the amount of workload constant for each processor while increasing the total workload.

1.3.1 Strong scaling

The number of threads used for OpenMp is set to one while the number of processes for OpenMpi is progressively increased from 0 to 16. Speed up and efficiency curves are given in figure 13. As it can be seen, the program runs twice as fast when 2 processes are used. For a number of cores

equal to 8 the program is 6 times faster which is still acceptable. Efficiency remains slightly above 0.6 for 16 processes.

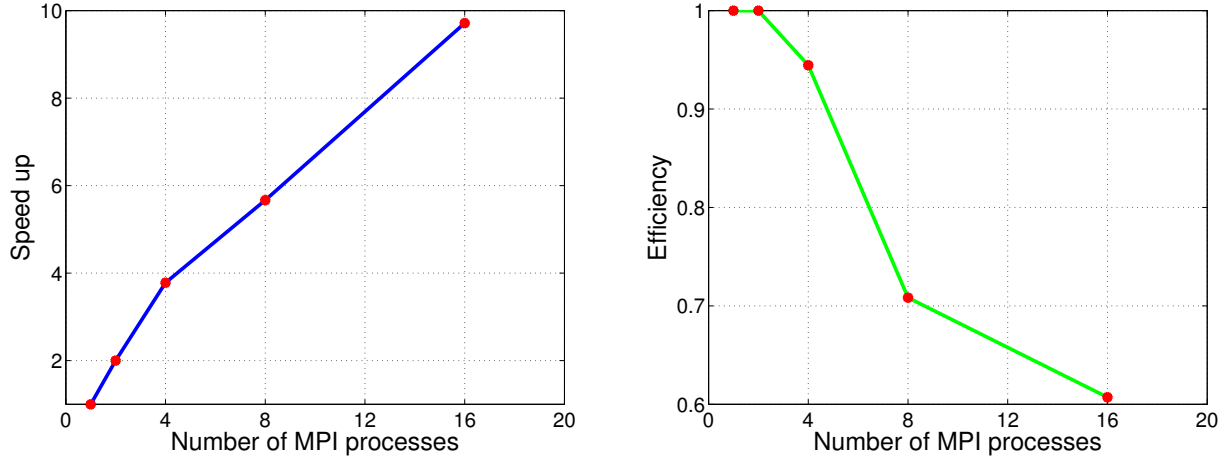


Figure 13: Speed up and efficiency curves of strong scaling for $N = 100$ and 300 time steps. $\Delta L = 0.005\text{m}$ and $\Delta t = 5 \times 10^{-12}\text{s}$.

A similar procedure was used to analyse the performance of the OpenMp implementation. While the number of cores for OpenMpi is kept at one, the number of threads for the use of OpenMp is increased from 1 to 16. FIGURE 14 shows speed up and efficiency curves of the implementation for OpenMp. As before, speed up is quite good when using 2 threads, but stagnates when the number of threads reaches 8. Efficiency drops to 0.4 for a number of threads equal to 16 as a consequence.

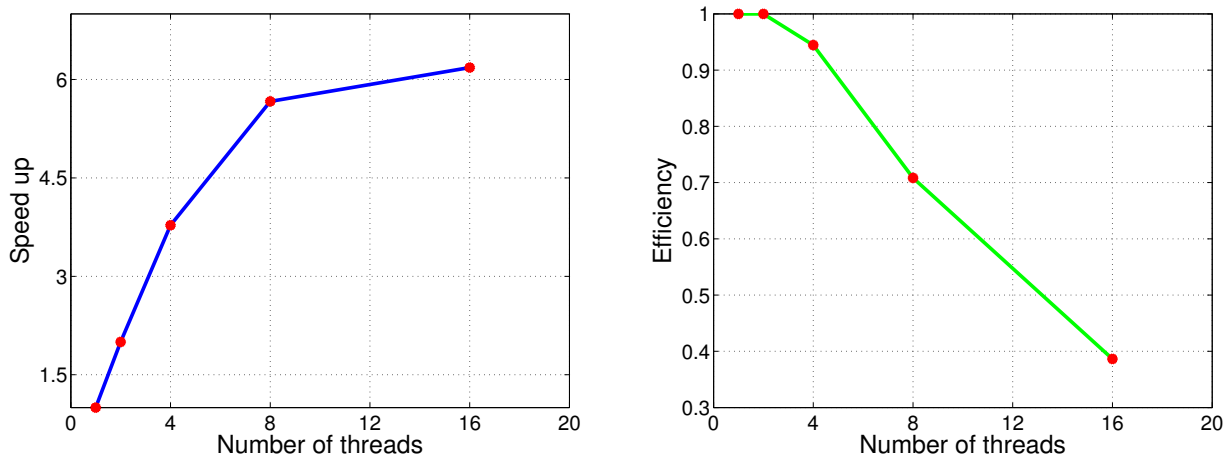


Figure 14: Speed up and efficiency curves of strong scaling for $N = 100$ and 300 time steps. $\Delta L = 0.005\text{m}$ and $\Delta t = 5 \times 10^{-12}\text{s}$.

A decent compromise between speed up and efficiency would be to launch the program using 8 processes with 8 threads.

1.3.2 Weak scaling

Weak scaling is analysed by doing a simple experiment. The box dimensions are multiplied by 2 and 3, while the number of cores used for OpenMpi is multiplied by 8 and 27. In this way the amount of data that has to be handled by each processor remains the same.

As seen in table 3 weak scaling is decent when the size of the problem is multiplied by 8. This does not hold true when the size of the problem is further increased. There is a significant jump in the time needed for communication by MPI from $N = 200$ to $N = 300$.

N	Number of cores for OpenMpi	Run time [s]
100	1	69
200	8	75
300	27	108

Table 3: Performance analysis of the OpenMpi implementation: Weak scaling

Finally, weak scaling of the OpenMp implementation is verified. For $N = 200$ and 8 threads the program runs for 116[s].

This unsatisfying scaling is mainly due to 2 reasons. The first one is the use of triple pointers to store the different components of both electric and magnetic fields. This choice was made because it better fitted our physical visualisation of the vector fields in 3D. It was undeniably a mistake, since OpenMpi is only able to transfer vectors between processes. Thus, at each time step, temporary vectors containing the values of the fields in the planes at the boundaries between 2 regions of space that were assigned to 2 different processes have to be filled. Looking at the speed up curves, it does not seem to be a major problem.

The second problem is the numerical method itself. It requires a large amount of cross process data transfer which increases with the total number of points in the grid.

Chapter 2

Heat equation solver

The second step in the development of a model of a microwave oven consists in implementing a solver for the heat equation. The aim of this solver is to compute the evolution of the temperature field inside the food from the knowledge of the power dissipated inside it. The food being possibly non homogeneous, the solver has to be able to compute a solution even for thermal properties (density, specific heat capacity and heat conductivity) that are not constant in space. Moreover, in the framework of the heating of a food in a microwave oven, it seems realistic to assume that the food exchanges heat with the environment through convection. Therefore, the solver should be able to handle Robin boundary conditions. Nevertheless, in order to dispose of a more general solver, both Robin and Dirichlet boundary conditions will be implemented.

First of all, the method used to discretize the heat equation and different features of the implementation are described. Then, similarly to what has been done for the electromagnetic solver, the quality of the model is assessed by solving numerically academic problems and comparing the results to what is theoretically expected.

Finally, the performances of the implementation is assessed by evaluating the strong and weak scaling.

2.1 Numerical model and implementation

As it will be highlighted, in the framework of this project, solving of the heat equation in time actually consists in solving a linear system of equations at each time step. More particularly, the general structure of the heat equation solver is presented in FIGURE 15.

In FIGURE 15, the matrix A is the matrix containing the coefficients appearing in the system of equations that has to be solved. The way this matrix can be constructed is explained in the following subsections.

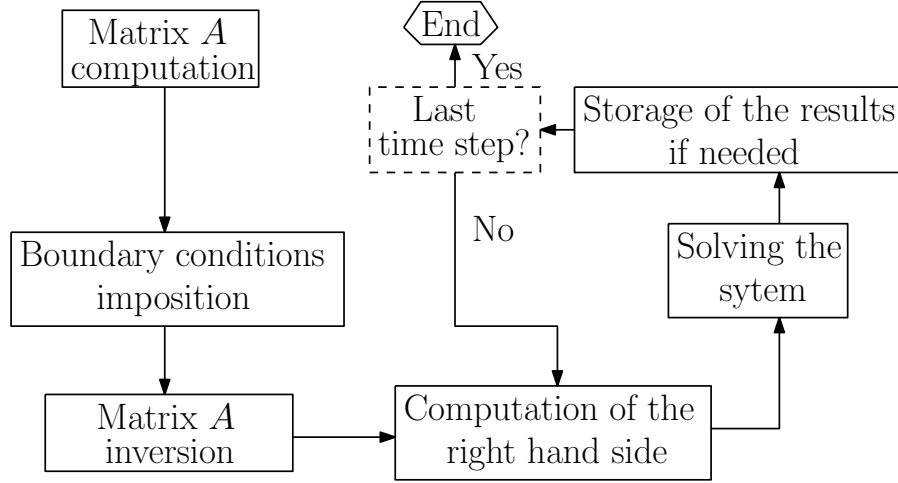


Figure 15: Flow chart of the heat equation solver.

2.1.1 Discretization of the heat equation

In general, the heat equation can be written as

$$\rho c_p \frac{\partial T}{\partial t} = \nabla \cdot (k \nabla T) + \dot{Q}_v, \quad (2.1)$$

where ρ is the density, c_p is the specific heat capacity, k is the thermal conductivity and \dot{Q}_v a volumetric heat source.

Considering a possibly non constant heat conductivity, in 1D, the derivatives operators appearing in equation (2.1) can be discretized as follows:

$$\begin{aligned}
 \frac{\partial T}{\partial t}(x = x_i, t = t_n) &\approx \frac{T_{i,j,k}^{n+1} - T_{i,j,k}^n}{\Delta t}, \\
 \frac{\partial}{\partial x} \left(k \frac{\partial T}{\partial x} \right) (x = x_i, t = t_n) &\approx \theta \left(\frac{\left(k \frac{\partial T}{\partial x} \right)_{i+1/2}^{n+1} - \left(k \frac{\partial T}{\partial x} \right)_{i-1/2}^{n+1}}{\Delta x} \right) + (1 - \theta) \left(\frac{\left(k \frac{\partial T}{\partial x} \right)_{i+1/2}^n - \left(k \frac{\partial T}{\partial x} \right)_{i-1/2}^n}{\Delta x} \right) \\
 &\approx \theta \left(\frac{k_{i+1/2}^{n+1} \left(\frac{\partial T}{\partial x} \right)_{i+1/2}^{n+1} - k_{i-1/2}^{n+1} \left(\frac{\partial T}{\partial x} \right)_{i-1/2}^{n+1}}{\Delta x} \right) + (1 - \theta) \left(\frac{k_{i+1/2}^n \left(\frac{\partial T}{\partial x} \right)_{i+1/2}^n - k_{i-1/2}^n \left(\frac{\partial T}{\partial x} \right)_{i-1/2}^n}{\Delta x} \right) \\
 &\approx \theta \left(\frac{k_{i+1/2}^{n+1} T_{i+1}^{n+1} - (k_{i+1/2}^{n+1} + k_{i-1/2}^{n+1}) T_i^{n+1} + k_{i-1/2}^{n+1} T_{i-1}^{n+1}}{(\Delta x)^2} \right) \\
 &\quad + (1 - \theta) \left(\frac{k_{i+1/2}^n T_{i+1}^n - (k_{i+1/2}^n + k_{i-1/2}^n) T_i^n + k_{i-1/2}^n T_{i-1}^n}{(\Delta x)^2} \right), \quad (2.2)
 \end{aligned}$$

where Δt is the time-step, Δx is the grid spacing and $\theta \in [0, 1]$ is a numerical parameter that determine if the scheme is explicit or implicit.

The partial derivatives with respect to the coordinates y and z can be approached in the same way as the one with respect to x . It can also be noticed that the temperature field and k are not on the same grid. Indeed, there is a shift of $\frac{\Delta x}{2}$ between them.

Therefore, replacing the derivatives operators by their discretization, one can obtain the following equation for the update of the temperature field in the bulk of the food:

$$\begin{aligned}
 T_{i,j,k}^{n+1} = & T_{i,j,k}^n \\
 & + \frac{\theta \Delta t}{\rho c_p (\Delta x)^2} \left[k_{i+1/2,j,k}^{n+1} T_{i+1,j,k}^{n+1} - (k_{i+1/2,j,k}^{n+1} + k_{i-1/2,j,k}^{n+1}) T_{i,j,k}^{n+1} + k_{i-1/2,j,k}^{n+1} T_{i-1,j,k}^{n+1} \right. \\
 & \quad + k_{i,j+1/2,k}^{n+1} T_{i,j+1,k}^{n+1} - (k_{i,j+1/2,k}^{n+1} + k_{i,j-1/2,k}^{n+1}) T_{i,j,k}^{n+1} + k_{i,j-1/2,k}^{n+1} T_{i,j-1,k}^{n+1} \\
 & \quad \left. + k_{i,j,k+1/2}^{n+1} T_{i,j,k+1}^{n+1} - (k_{i,j,k+1/2}^{n+1} + k_{i,j,k-1/2}^{n+1}) T_{i,j,k}^{n+1} + k_{i,j,k-1/2}^{n+1} T_{i,j,k-1}^{n+1} \right] \\
 & + \frac{(1-\theta) \Delta t}{\rho c_p (\Delta x)^2} \left[k_{i+1/2,j,k}^n T_{i+1,j,k}^n - (k_{i+1/2,j,k}^n + k_{i-1/2,j,k}^n) T_{i,j,k}^n + k_{i-1/2,j,k}^n T_{i-1,j,k}^n \right. \\
 & \quad + k_{i,j+1/2,k}^n T_{i,j+1,k}^n - (k_{i,j+1/2,k}^n + k_{i,j-1/2,k}^n) T_{i,j,k}^n + k_{i,j-1/2,k}^n T_{i,j-1,k}^n \\
 & \quad \left. + k_{i,j,k+1/2}^n T_{i,j,k+1}^n - (k_{i,j,k+1/2}^n + k_{i,j,k-1/2}^n) T_{i,j,k}^n + k_{i,j,k-1/2}^n T_{i,j,k-1}^n \right] + \frac{\Delta t}{\rho c_p} Q_{v;i,j,k}^{n+1}. \quad (2.3)
 \end{aligned}$$

In practice this equation is implemented using 4 different grids. One for the temperature and 3 for k having an offset of $\frac{\Delta x}{2}$ respectively in the x , y and z direction.

As centered-in-space finite difference approximation has been used to discretize the spatial derivatives, the numerical scheme is expected to be convergent of order 2 in space. The order of convergence in time depends on the chosen value for θ , which will be further discussed later.

Equation 2.3 can be rewritten in matrix form, that is

$$[\mathbb{I} - A] \mathbf{T}^{n+1} = [\mathbb{I} + A] \mathbf{T}^n + \frac{1}{\rho c_p} \mathbf{q}^{n+1}, \quad (2.4)$$

where $[\mathbb{I}]$ is the identity matrix and $[A]$ is a sparse matrix of dimension $(N_x \times N_y \times N_z) \times (N_x \times N_y \times N_z)$ where N_i is the number of temperature grid points in direction i .

2.1.2 Boundary conditions

First of all, it should be highlighted that the heat equation will be solved only inside the food. Indeed, the temperature of the surrounding air will not be updated and has therefore no physical meaning. Therefore, in order to have a well posed problem, one has to add some boundary conditions to the problem.

The first considered boundary condition is the simplest to implement practically: Dirichlet boundary condition. Indeed, it simply consists in imposing the value of the temperature on the boundary of the food to a known value. By doing so, the user has no control on the heat flux passing through the boundary of the food. This kind of boundary condition will be very useful during the validation. Nevertheless, it will not be used afterwards as it is not physically

consistent with the heating of food inside a microwave oven.

Besides that, one can also impose a Robin boundary condition. This condition consists in imposing the following relation on the surface of the food:

$$k \nabla T \cdot \mathbf{n} = h (T - T_\infty), \quad (2.5)$$

where \mathbf{n} is the unit outward normal of the surface of the food, h is the heat transfer coefficient (in $W \cdot m^{-2} \cdot K^{-1}$) and T_∞ is the temperature of the air in the far field.

This kind of boundary conditions allows the user to have a control on the heat flux passing through the boundary of the food and are better suited to model the phenomena actually happening inside the microwave oven. It should be highlighted that homogeneous Neumann boundary conditions can be obtained by imposing $h = 0$.

In practice, the boundary conditions are managed as follows in the implementation. First of all a loop is performed over all the thermal grid points. For each point, a condition verifies if this point belongs to the air volume or if it belongs to the food. The points belonging to the food are handled by applying the discretized heat equation (eq. 2.3) to them.

Then, for the remaining points, a condition verifying if the point is next to the surface of the food or not is checked. This is done by verifying if the closest neighbouring points belong to the volume of air or of the food. For the points being next to the surface, the equation (2.5) is imposed. As an example, consider the configuration represented in FIGURE 16:

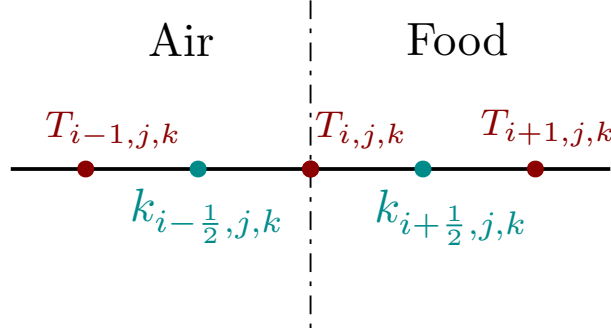


Figure 16: Representation of a discretized interface between air and food.

In such a situation, the following equation will be imposed for the point $(i - 1, j, k)$:

$$k_{i+\frac{1}{2},j,k} \frac{(T_{i+1,j,k}^{n+1} - T_{i-1,j,k}^{n+1})}{2 \Delta x} = h (T_{i,j,k}^{n+1} - T_\infty). \quad (2.6)$$

It is important to notice that centered-in-space finite difference approximation has also been used to discretize the spatial derivative appearing in equation (2.5). Consequently, the order of convergence of the numerical scheme is not expected to be affected by the imposition of Robin boundary conditions.

Finally, no equation is solved for the remaining point in the air and their temperature are thus meaningless. Therefore, the following equation can be simply imposed for those points:

$$T_{i,j,k}^{n+1} = T_{air} . \quad (2.7)$$

2.2 Heat equation solver validation

Similarly to the reasoning followed for the electromagnetic solver, the heat equation solver is not used directly to solve very complex problems. Indeed, as a first step, the solver is employed to compute numerical solutions for problems whose analytic solutions are known. By doing this, the validity of the implementation can be verified. Furthermore, the accuracy and the order of convergence of the numerical scheme can be looked at.

2.2.1 Steady state heat equation across two different media

A first test consists in solving a steady state heat equation on a domain, where 2 parallelepipedic foods with different thermal conductivities are placed. For the first medium, $k_1 = 1[\text{W/Km}^3]$ and for the second one, $k_2 = 2[\text{W/Km}^3]$. Dirichlet boundary condition is imposed on the left boundary where the temperature is set to $50^\circ[\text{C}]$. Dirichlet boundary condition is also imposed on the right boundary where the temperature is set to $0^\circ[\text{C}]$. A homogeneous Neumann boundary condition is applied on the 4 other boundaries of the food. The considered problem is represented in FIGURE 17:

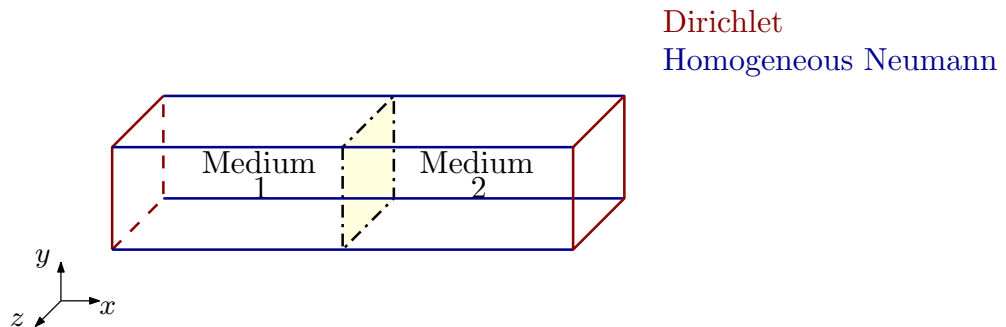


Figure 17: Representation of the 3D steady state thermal problem without source across two different media.

Such a problem can be treated as a 1D heat conduction. The geometry therefore simplifies as shown in FIGURE 18:

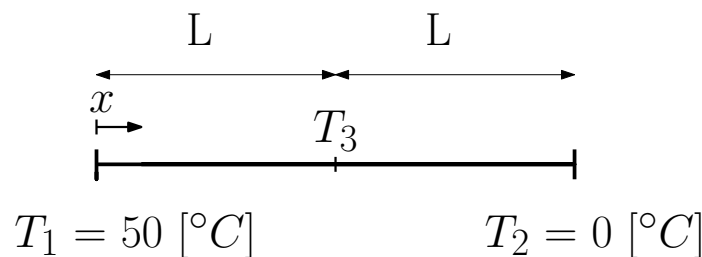


Figure 18: Representation of the 1D steady state thermal problem without source across two different media.

Theoretically, a constant temperature gradient across each object should appear, with a discontinuity at the interface. The following reasoning justifies this result. The temperature fields inside both cubes is given by:

$$\begin{cases} T_a(x) = c_1 \cdot x + A \\ T_b(x) = c_2 \cdot x + B. \end{cases} \quad (2.8)$$

The heat flux should be continuous across the interface. Thus the following equality has to be satisfied:

$$k_1 \frac{T_2 - T_1}{L} = k_2 \frac{T_3 - T_2}{L}, \quad (2.9)$$

which can also be written as

$$\frac{k_1}{k_2} = \frac{c_2}{c_1}. \quad (2.10)$$

Therefore, this problem was solved numerically and the results are shown in FIGURE 19:

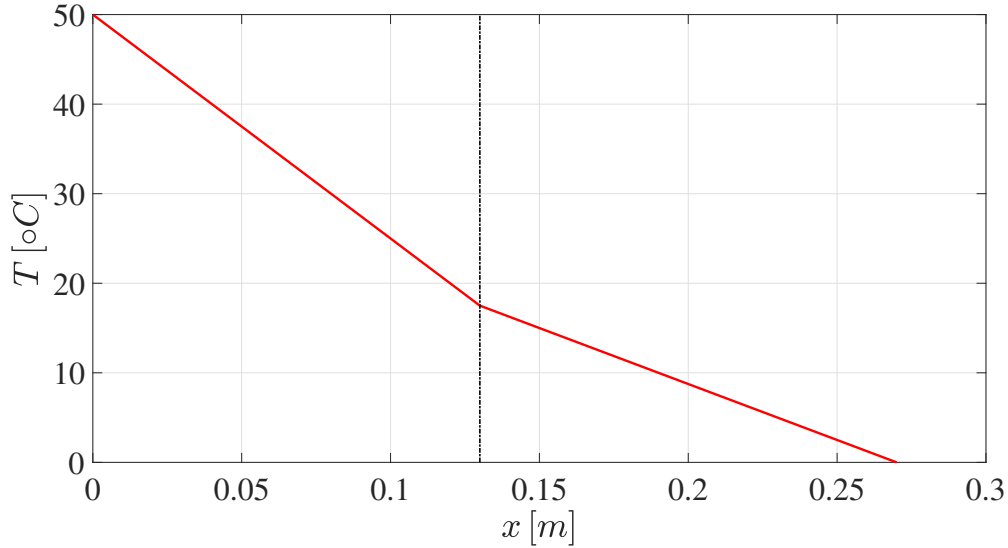


Figure 19: Temperature field computed by the solver inside 2 adjacent cubic objects on a cut along the x axis. $L = 0.14[m]$, $\Delta t = 0.1[s]$ and $\Delta x = 0.05[m]$.

As anticipated, the numerical solution takes the form of 2 straight lines. Their slopes are $-250[^\circ\text{C}/\text{m}]$ and $-125[^\circ\text{C}/\text{m}]$. As expected their ratio is equal to $\frac{k_2}{k_1}$.

Using equation (2.9) it is possible to predict the temperature at the interface T_2 . Since $T_3 = 0$ this relation becomes:

$$\frac{T_1}{T_2} = 3. \quad (2.11)$$

In the present case $T_2 = 16.7[^\circ\text{C}]$ as expected.

2.2.2 Transient heat conduction

The second test that was performed concerned the transient heat equation inside a parallelepipedic domain. Once again, Dirichlet boundary conditions are imposed on 2 opposing faces and homogeneous Neumann boundary conditions are imposed on the remaining boundary of the domain. Heat capacity, density and thermal conductivity are constant over the entire domain. Again, this problem can be simplified to a 1D configuration as shown in FIGURE 20:

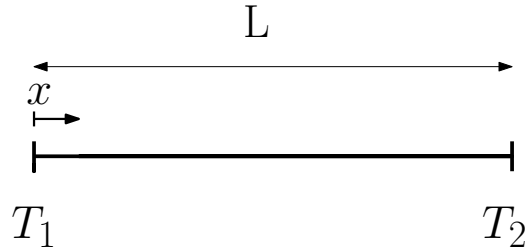


Figure 20: Representation of the 1D transient thermal problem without source in an homogeneous medium.

In such conditions, the governing equations write:

$$\begin{cases} \frac{\partial T}{\partial t} = \alpha \frac{\partial^2 T}{\partial x^2} & \text{in } x \in]0; L[\times t \in [0; +\infty[, \\ T(x, 0) = 0 & \text{on } x \in]0; L[\times \{t = 0\}, \\ T(0, t) = T_1 & \text{on } \{x = 0\} \times t \in [0; +\infty[, \\ T(L, t) = T_2 & \text{on } \{x = L\} \times t \in [0; +\infty[. \end{cases} \quad (2.12)$$

Using separation of variables one can show that the solution is given by

$$T(x, t) = (T_1 + T_2) \left(1 - \frac{x}{L}\right) - 2 \sum_{k=1}^{+\infty} \frac{T_1 + T_2}{k\pi} \exp\left(-\left(\frac{k\pi}{L}\right)^2 \alpha t\right) \sin\left(\left(\frac{k\pi}{L}\right) x\right). \quad (2.13)$$

Figure 21 compares analytic and numerical solutions. The parameters that were used are given in table 4.

Configuration	Thermal diffusivity $\alpha[\text{m}^2/\text{s}]$	$T_1[^\circ\text{C}]$	$T_2[^\circ\text{C}]$
1	$2 \cdot 10^{-4}$	100	50
2	$2 \cdot 10^{-4}$	100	0
3	$4 \cdot 10^{-4}$	100	50
4	$4 \cdot 10^{-4}$	100	0

Table 4: Parameters used for the different tests concerning transient heat conduction.

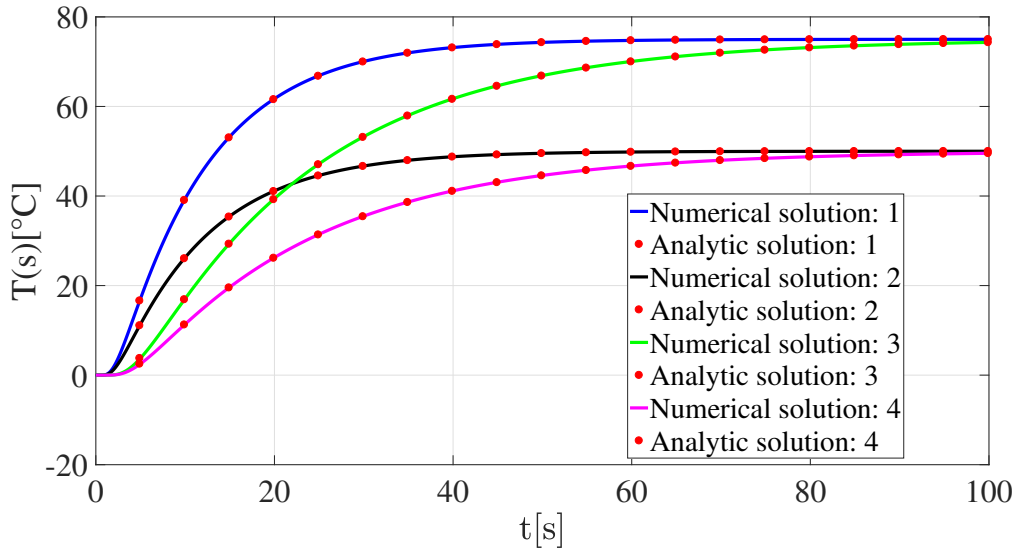


Figure 21: Comparison between numerical and analytic solution for the simple case of transient heat conduction. $L = 0.3[m]$, $\Delta t = 0.1[s]$, $\tau = 100[s]$ and $\Delta x = 0.01$

The solutions provided by the solver are in good agreement with the analytic solution in all the tested configurations.

2.2.3 Effects of a heat source

The third test that was performed concerned the steady state heat equation with a constant source term. Again, Dirichlet boundary conditions are imposed on 2 opposing faces and Neumann boundary conditions are imposed on the remaining boundary of the food. The thermal conductivity is constant over the whole domain and is set to $2[W/Km^3]$. The problem can be treated as one dimensional, as already shown in FIGURE 20.

This time, the governing equations that have to be solved are:

$$\begin{cases} k \frac{d^2 T}{dx^2} = -Q \\ T(x=0) = T_1 \\ T(x=L) = T_2, \end{cases}$$

where Q is the heat source in $[W/m^3]$.

Integrating the governing equation twice and using both boundary conditions one gets:

$$T(x) = -\frac{Q}{2k}x^2 + \frac{QL}{2k}x + \frac{T_2 - T_1}{L}x + T_1. \quad (2.14)$$

In the test that was carried out T_1 and T_2 were both fixed to $0[^\circ C]$. Defining a dimensionless length $X = \frac{x}{L}$, one can rewrite the solution as:

$$T(X) = \frac{QL^2}{2k}(1-X)X. \quad (2.15)$$

Figure 22 shows a comparison between the analytic solution and the solution provided by the solver.

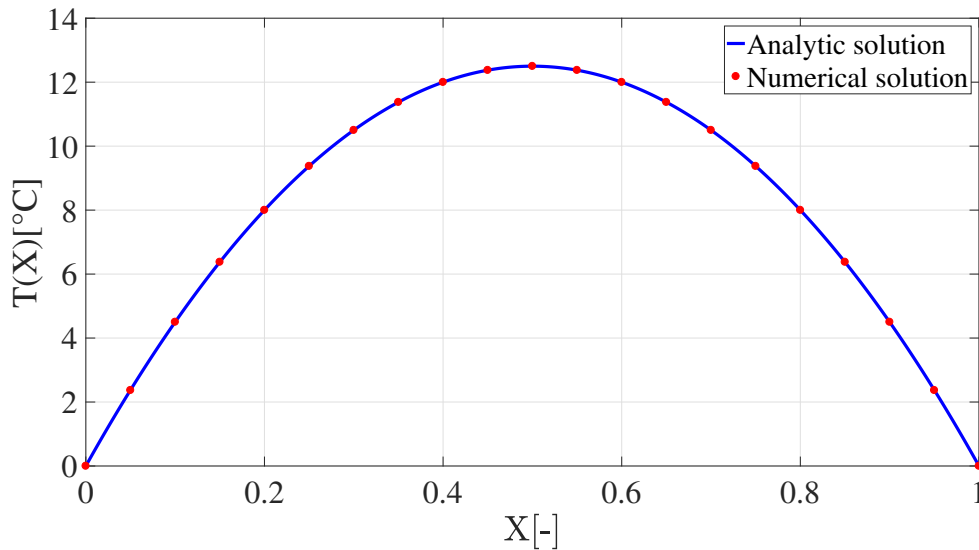


Figure 22: Comparison between numerical and analytic solution for the simple case of transient heat conduction. $L = 0.3[m]$, $\Delta t = 0.1[s]$ and $\Delta x = 0.01$.

As it can be seen the numerical solution fits quite well the analytic solution.

2.2.4 Spatial order of convergence of the numerical scheme

As a reminder, the numerical scheme used to implement the heat equation as well as the boundary conditions are supposed to be convergent of order 2 in space. The previous tests were too simple to assess this order of convergence. Indeed, in these cases, the exact solution is in fact recovered by the numerical scheme.

In this section, the aim is to consider slightly more complex problems whose exact solutions are still known but which can not be solved exactly by the solver. Therefore, the evolution of the numerical error with respect to the spatial discretization will give an information on the order of convergence of the numerical scheme.

In this framework, two 1D problems were considered in order to highlight that neither Dirichlet nor Robin boundary conditions alter the order of convergence of the numerical scheme.

Dirichlet boundary conditions

Let us consider the solving of the heat equation inside a cubic domain for which Dirichlet boundary conditions are imposed on two opposing faces and homogeneous Neumann boundary conditions are imposed on the four remaining faces. As previously done, this problem can be reduced to a 1D problem whose parameters are represented in FIGURE 23:

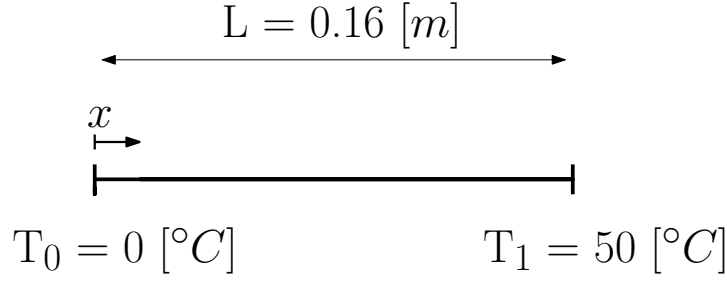


Figure 23: Representation of the geometry and of the boundary conditions of the heat transfer problem to be solved.

In the framework of the convergence order verification, steady state condition can be considered to solve the heat equation. Therefore, the equation to be solved inside the domain is the following:

$$-k \frac{\partial^2 T}{\partial x^2} = Q(x), \quad (2.16)$$

where k is the heat conductivity of the medium and $Q(x)$ is the volumetric heat source. In order to highlight the convergence of the scheme, the considered problem has to be sufficiently complicated so that an error in the numerical solution is observed. Consequently, the considered profile of the heat source used here is as follows:

$$Q(x) = Q \cdot \sin\left(\frac{\pi}{L} x\right), \quad (2.17)$$

where Q is a constant.

Using the boundary conditions shown in FIGURE 23, the exact solution of this problem can be written as:

$$T(x) = \frac{L^2 Q}{k \pi^2} \sin\left(\frac{\pi}{L} x\right) + \frac{50}{L} x. \quad (2.18)$$

Firstly, this simple problem was solved numerically by using a grid spacing $dx = 0.01 \text{ [m]}$ in order to verify the accordance between the numerical solution and the exact one. The obtained results are shown in FIGURE 24:

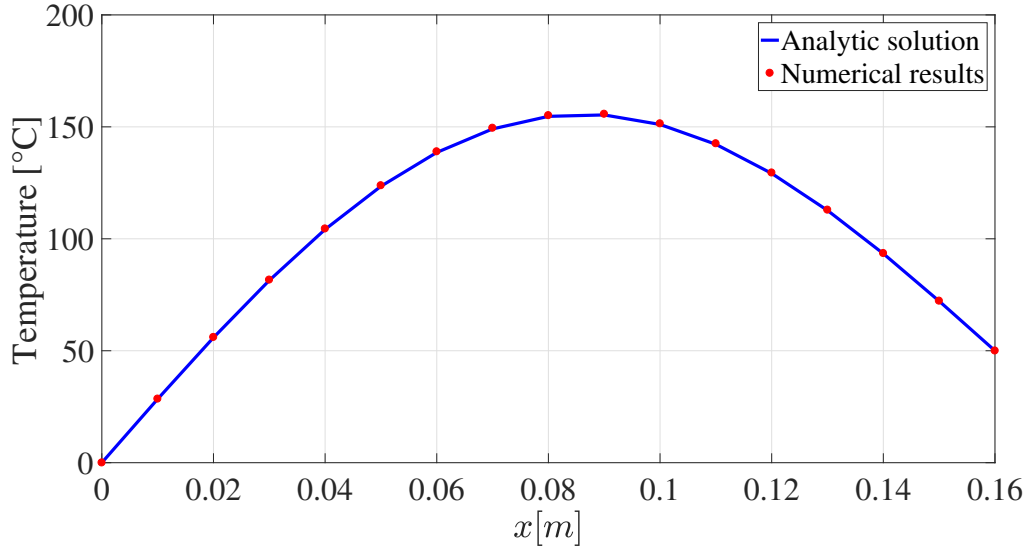


Figure 24: Comparison between the numerical and the exact steady state temperature profiles. The numerical parameters are : $k = 1 [W \cdot K^{-1} \cdot m^{-1}]$, $Q = 50000 [W \cdot m^{-3}]$, $L = 0.16 [m]$ and $dx = 0.01 [m]$.

As it can be seen, the numerical solution fits quite well on the exact one despite some small deviations.

After that, the same problem has been solved by using a grid spacing of $0.02 [m]$ and $0.005 [m]$. For each case, the global error committed in the numerical solution has been assessed as follows:

$$\varepsilon = \max_{0 \leq j \leq \frac{L}{dx}} (|T_j - T(x_j)|), \quad (2.19)$$

where T_j is the numerical solution at the node j and $T(x_j)$ is the exact solution evaluated at $x = j \cdot dx$.

Therefore, the obtained evolution of the global error as a function of the grid spacing as well as its linear regression are represented in FIGURE 25. These results seem to fit quite well on the linear regression. Furthermore, the slope of the straight line obtained with the linear regression is equal to 2.0052 meaning that the numerical scheme is indeed convergent of order 2. Finally, the solver capacity of maintaining the problem 1D property is verified. Indeed, the temperature evolution as a function of the y for $x = 0.08 [m]$ is represented in FIGURE 26:

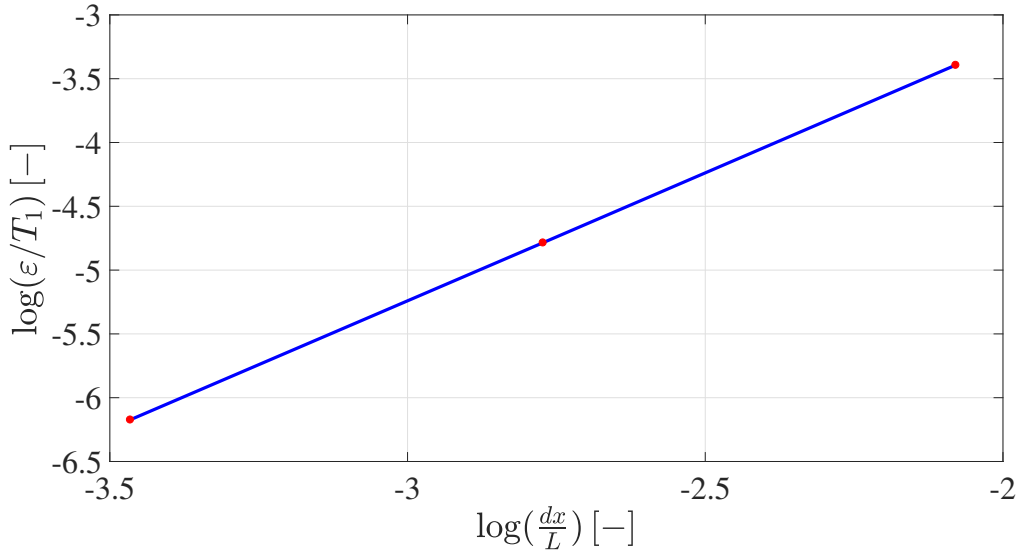


Figure 25: Evolution of the global error as a function of the grid spacing. The numerical parameters are : $k = 1 [W \cdot K^{-1} \cdot m^{-1}]$, $Q = 50000 [W \cdot m^{-3}]$, $L = 0.16 [m]$.

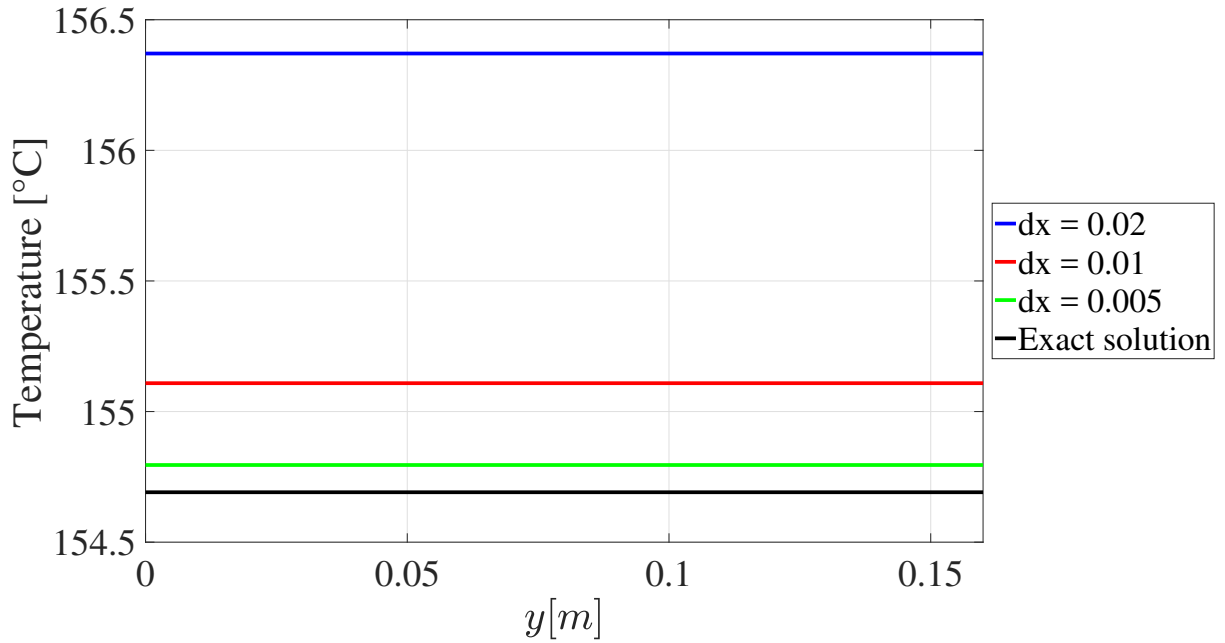


Figure 26: Evolution of the temperature as a function of y for $x = 0.08 [m]$ for different value of the grid spacing. The numerical parameters are : $k = 1 [W \cdot K^{-1} \cdot m^{-1}]$, $Q = 50000 [W \cdot m^{-3}]$, $L = 0.16 [m]$.

As it has already been observed, the difference between the exact and the numerical solution decreases when the grid spacing decreases. Besides this, it can also be seen in FIGURE 26 that the temperature is independent of the y coordinate as expected. The same reasoning in the z direction can be carried out in order to show that the temperature does not depend on the z coordinate neither. Therefore, the 1D property of the problem is indeed conserved by the

numerical scheme.

Robin Boundary conditions

The aim of this subsection is to verified if the numerical scheme convergence order is conserved when solving a problem with non homogeneous boundary conditions. Therefore, the same problem that in the previous subsection is numerically solved the only difference consisting in changing the boundary condition imposed at $x = L$. Indeed, here, a convection relation will be imposed at the boundary:

$$-k \frac{\partial T}{\partial x} \Big|_{x=L} = h (T - T_{\infty}), \quad (2.20)$$

where h is the heat transfer coefficient [$W \cdot m^{-2} \cdot K^{-1}$] and T_{∞} is the temperature in the far field.

The exact solution of this new problem can be expressed as follows:

$$T(x) = \frac{Q L^2}{k \pi^2} \sin\left(\frac{\pi}{L} x\right) + \frac{\frac{Q L}{\pi} + h T_{\infty}}{k + h L} x. \quad (2.21)$$

The problem was therefore solved using the solver. The numerical results are compared to the exact solution in FIGURE 27:

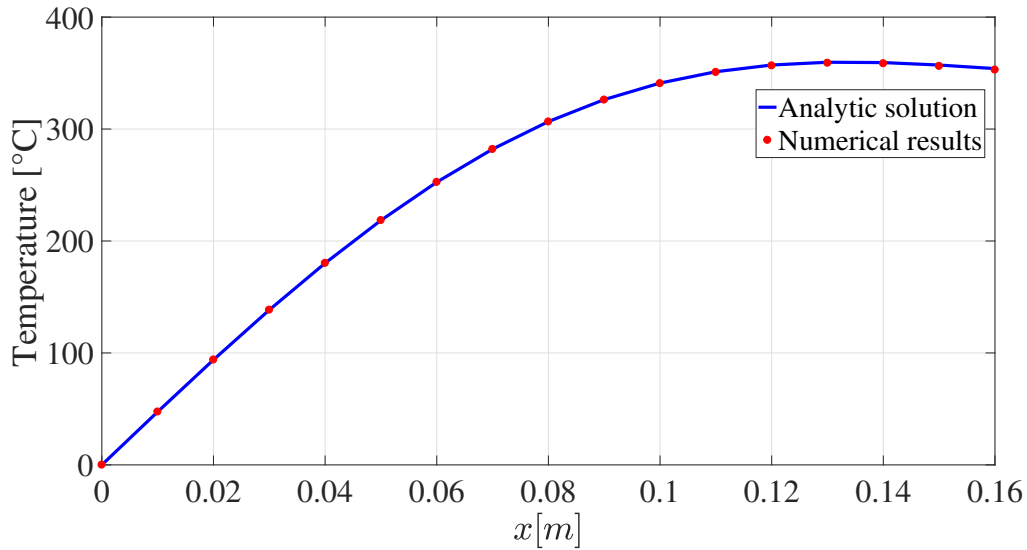


Figure 27: Comparison between the numerical and the exact steady state temperature profiles. The numerical parameters are : $k = 1$ [$W \cdot K^{-1} \cdot m^{-1}$], $Q = 50000$ [$W \cdot m^{-3}$], $L = 0.16$ [m], $h = 1$ [$W \cdot m^{-2} \cdot K^{-1}$] and $dx = 0.01$ [m].

As it can be seen in FIGURE 27 the correspondence between the numerical results and the exact solution is quite satisfying. Therefore, the same way of measuring the amplitude of the numerical error is used to assessed the numerical scheme convergence order. The evolution of the error as a function of the grid spacing as well as its linear regression are shown in FIGURE 28:

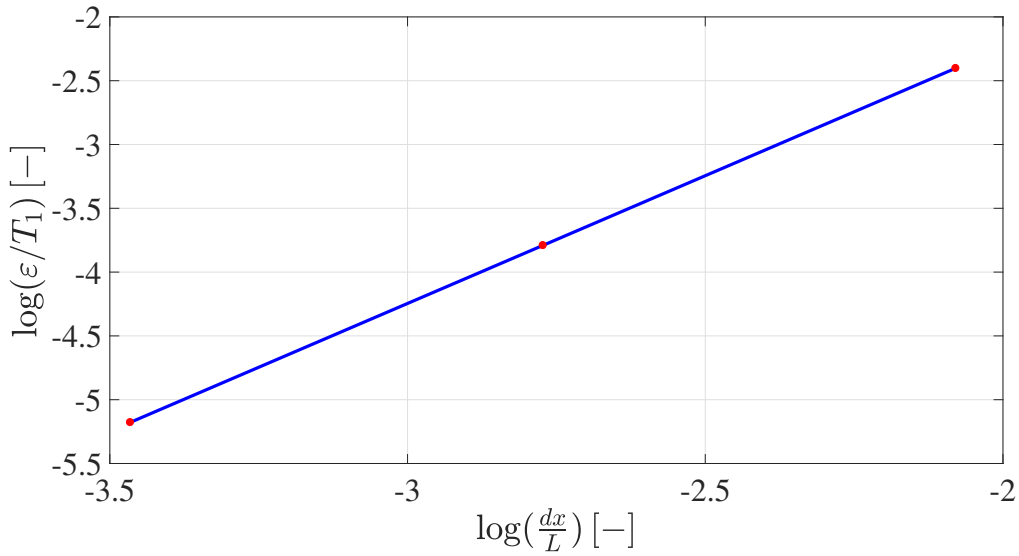


Figure 28: Evolution of the global error as a function of the grid spacing. The numerical parameters are : $k = 1 [W \cdot K^{-1} \cdot m^{-1}]$, $Q = 50000 [W \cdot m^{-3}]$, $L = 0.16 [m]$, $h = 1 [W \cdot m^{-2} \cdot K^{-1}]$ and $dx = 0.01 [m]$.

Once again, a straight line with a slope equal to 2 is recovered meaning that the numerical scheme is still convergent of order 2 in such conditions. Finally, the conservation of the 1D property of the problem is also verified by plotting the profile of temperature in a perpendicular direction:

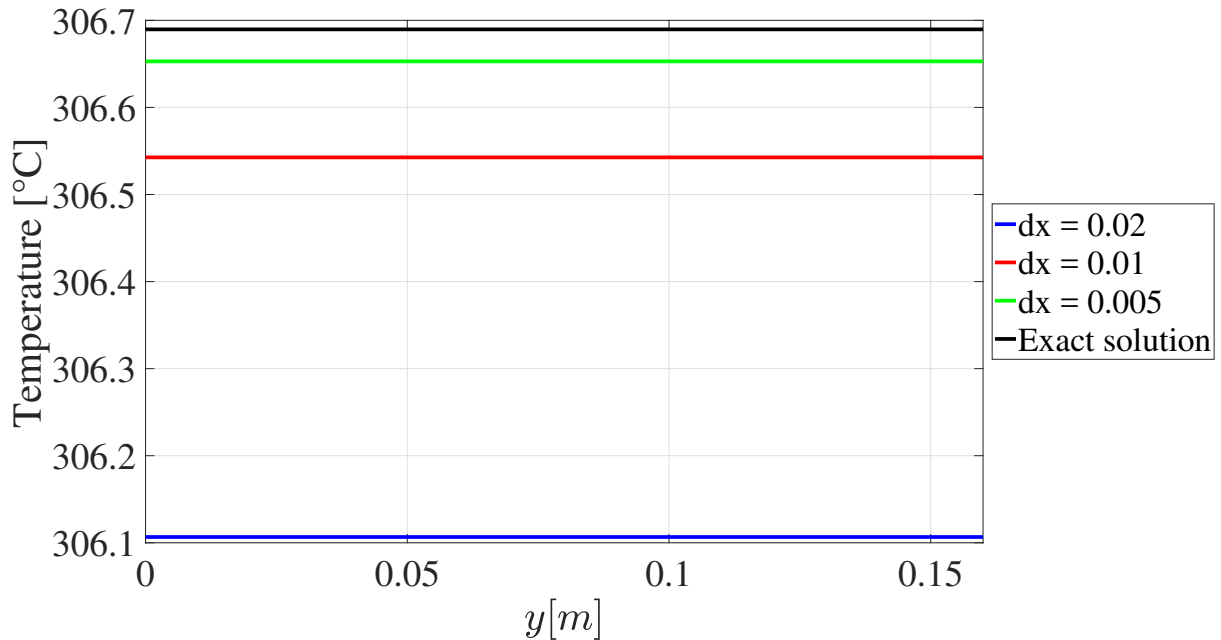


Figure 29: Evolution of the temperature as a function of y for $x = 0.08 [m]$ for different value of the grid spacing. The numerical parameters are : $k = 1 [W \cdot K^{-1} \cdot m^{-1}]$, $Q = 50000 [W \cdot m^{-3}]$, $L = 0.16 [m]$.

The obtained profile being constant, the 1D property is indeed well conserved by the numerical scheme even when solving a problem with Robin boundary conditions.

2.3 Temporal order of convergence

In this section, the temporal order of convergence of the thermal solver is looked at. As it will be highlighted, this order of convergence depends on the chosen value for theta, two different possibilities are considered in this section. The first one is the case in which $\theta = 1$, leading to the implicit Euler numerical scheme, which should be of order 1 in time. Besides this, the case $\theta = 0.5$, corresponding to the Crank–Nicholson method is also considered. This second method is supposed to be of order 2 in time.

Once again, the analysis of the temporal order of convergence requires to consider a sufficiently complex problem. For this purpose, the heat equation will be solved on a cubic domain inside which a source varying in a sinusoidal way in time and homogeneous in space is applied. Furthermore, homogeneous Neumann boundary conditions are applied on all boundaries. Analytically, the heat equation for each point of the domain writes:

$$\rho c_p \frac{\partial T}{\partial t} = Q \sin(\omega t). \quad (2.22)$$

In this section, both ρ and c_p are set to unity and Q is set to 50000 [W^{-3}]. Furthermore, the value of ω is fixed to $\frac{2\pi}{10}$. This choice for the value of ω is motivated by the fact that a characteristic time for the microwave oven (different than the thermal and electromagnetic characteristic time) is the period of rotation of the food inside the oven. Typically, this period is of the order of 10 [s].

The exact solution of the problem can be derived easily and is given by:

$$T = \frac{Q}{\rho c_p \omega} (1 - \cos(\omega t)). \quad (2.23)$$

The problem was solved numerically and the global error has been evaluated as follows:

$$\varepsilon = \max_{0 \leq n \leq T_f} (|T^n - T(t_n)|), \quad (2.24)$$

where T_f is the total duration of the simulation and is in this case equal to 100 [s]. The evolution of the error as a function of the time step is represented in Figure 30

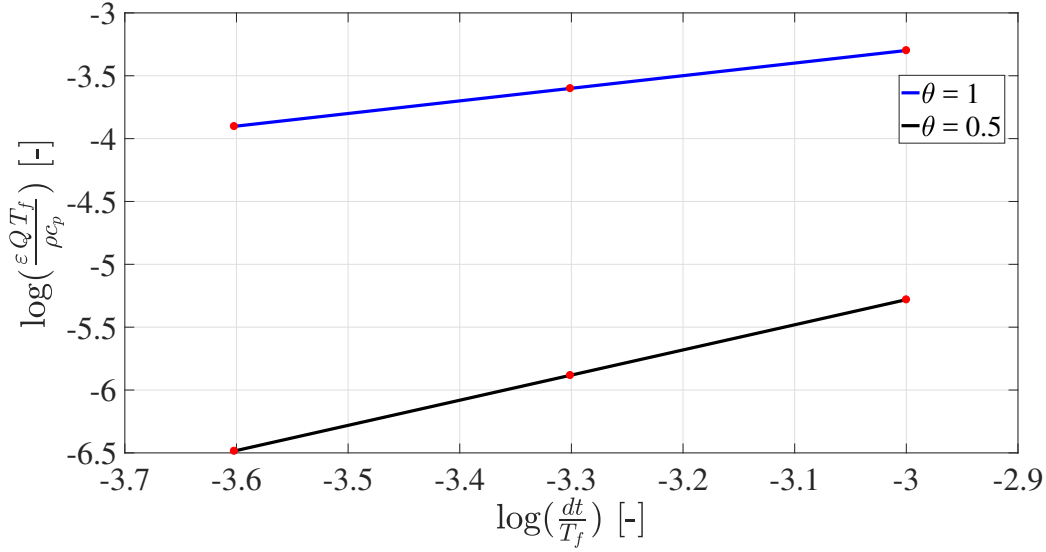


Figure 30: Evolution of the global error as a function of the time step for both the implicit Euler and Crank–Nicholson methods.

A careful analysis of Figure 30 can lead to the conclusion that the temporal order of convergence of both method are indeed the expected one.

2.4 Stability analysis of the thermal solver

In this section, the stability of the numerical scheme used will be assessed, using Von Neumann analysis, which consists of analysing the effect of the numerical scheme on a Fourier component of the solution. The aim of this section is to establish a criterion at which the numerical scheme is supposedly unstable, leading to a discussion on the parameter θ that was defined when discretising the heat equation. Moreover, this analysis will be performed considering that the thermal conductivity k is constant, and it will be assumed that there is no heat source. Under those assumptions, the heat equation reads

$$\frac{\partial T}{\partial t} = \alpha \nabla^2 T, \quad (2.25)$$

and the numerical scheme becomes

$$\begin{aligned} T_{i,j,k}^{n+1} = & T_{i,j,k}^n + \theta \frac{\overbrace{\alpha \Delta t}^{\mu}}{\Delta x^2} \left(T_{i+1,j,k}^{n+1} + T_{i-1,j,k}^{n+1} + T_{i,j+1,k}^{n+1} + T_{i,j-1,k}^{n+1} + T_{i,j,k+1}^{n+1} + T_{i,j,k-1}^{n+1} - 6T_{i,j,k}^{n+1} \right) \\ & + (1 - \theta) \frac{\alpha \Delta t}{\Delta x^2} \left(T_{i+1,j,k}^n + T_{i-1,j,k}^n + T_{i,j+1,k}^n + T_{i,j-1,k}^n + T_{i,j,k+1}^n + T_{i,j,k-1}^n - 6T_{i,j,k}^n \right). \end{aligned} \quad (2.26)$$

Defining $\boldsymbol{\xi} = [\xi_1, \xi_2, \xi_3]^T$ as the wave number vector and $\mathbf{s} = [i, j, k]^T$, the solution can be expressed in terms of Fourier components as

$$T_{i,j,k}^n = \exp(i\Delta x \boldsymbol{\xi} \cdot \mathbf{s}), \quad T_{i,j,k}^{n+1} = \gamma(\boldsymbol{\xi}) \exp(i\Delta x \boldsymbol{\xi} \cdot \mathbf{s}), \quad (2.27)$$

where $\gamma(\boldsymbol{\xi})$ is called the amplification factor. This factor should be smaller than one, in order to achieve stability. Plugging this solution into the numerical scheme yields

$$\begin{aligned} \gamma(\boldsymbol{\xi}) = 1 + \gamma(\boldsymbol{\xi})\theta\mu [\exp(i\xi_1\Delta x) + \exp(-i\xi_1\Delta x) + \exp(i\xi_2\Delta x) + \exp(-i\xi_2\Delta x) + \exp(i\xi_3\Delta x) \\ + \exp(-i\xi_3\Delta x) - 6] + (1 - \theta)\mu [\exp(i\xi_1\Delta x) + \exp(-i\xi_1\Delta x) + \exp(i\xi_2\Delta x) \\ + \exp(-i\xi_2\Delta x) + \exp(i\xi_3\Delta x) + \exp(-i\xi_3\Delta x) - 6]. \end{aligned} \quad (2.28)$$

Using trigonometric relations, the amplification factor can be written as

$$\gamma(\boldsymbol{\xi}) = \frac{1 - 4\mu(1 - \theta) \sum_{i=1}^3 \sin^2\left(\frac{\xi_i h}{2}\right)}{1 + 4\mu\theta \sum_{i=1}^3 \sin^2\left(\frac{\xi_i h}{2}\right)}. \quad (2.29)$$

In the limit case where $\sum_{i=1}^3 \sin^2\left(\frac{\xi_i h}{2}\right) = 3$, the condition under which the numerical scheme is stable is given by

$$\left| \frac{1 - 12\mu(1 - \theta)}{1 + 12\mu\theta} \right| \leq 1. \quad (2.30)$$

This inequality is satisfied if

$$\mu \leq \frac{1}{6(1 - 2\theta)}, \quad (2.31)$$

i.e. the numerical scheme is conditionally stable when $\theta < 0.5$, and it becomes unconditionally stable when $\theta \geq 0.5$, since μ is positive by definition. For instance, this relation is shown in FIGURE 31. As long as the value of μ is located under this curve, the scheme is stable.

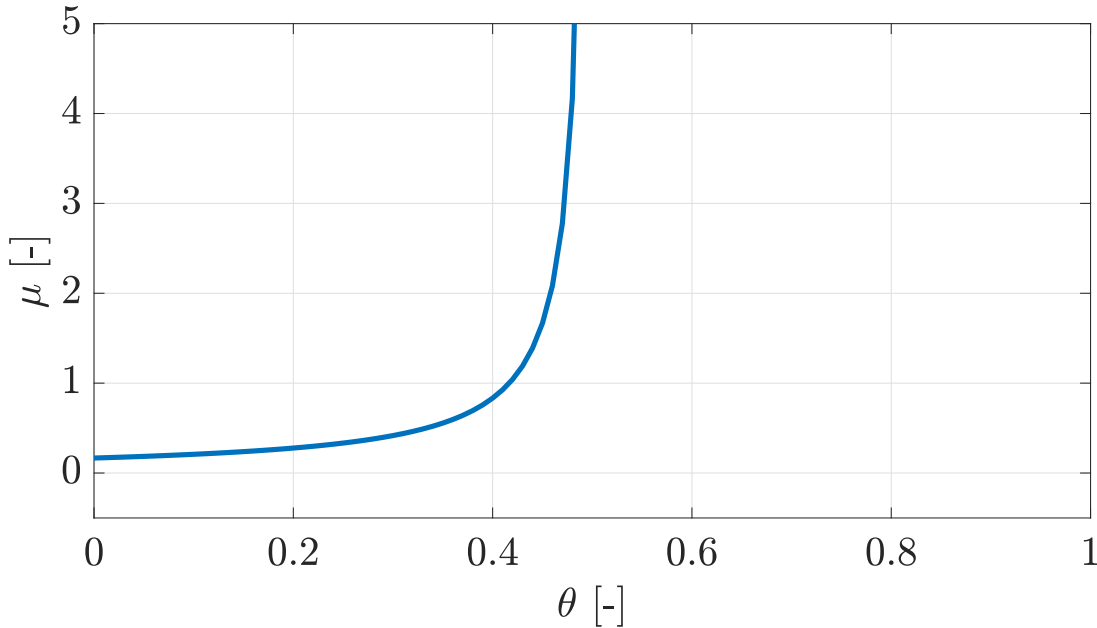


Figure 31: Limit value of μ as a function of the parameter θ , according to Eq. 2.31.

‘ When using physical properties, this criterion does not seem to be too constraining. However, since the numerical scheme needs to handle changes in the properties of the material with temperature, hence changes in the stability criterion, it seems more convenient to work with an unconditionally stable scheme. Moreover, it has been shown that working with $\theta = 0.5$ results in a numerical scheme that is convergent of order two in space and in time.

2.4.1 Test on an explicit solver ($\theta = 0$)

Setting $\theta = 0$, the stability criterion becomes

$$\frac{\alpha \Delta t}{\Delta x^2} \leq \frac{1}{6}$$

Using $\alpha = 1$ and $\Delta x = 0.01$, one finds that the temporal step has to be such that

$$\Delta t \leq 1.66 \cdot 10^{-5}.$$

FIGURE 32b shows the effect of taking values of Δt that do not meet this criterion. As expected, taking a time increment that is not small enough leads to spurious results, compared to FIGURE 32a, which respects the condition. Indeed, the result obtained seems to oscillate, as well as growing over time, which leads to absurd values for the temperature field.

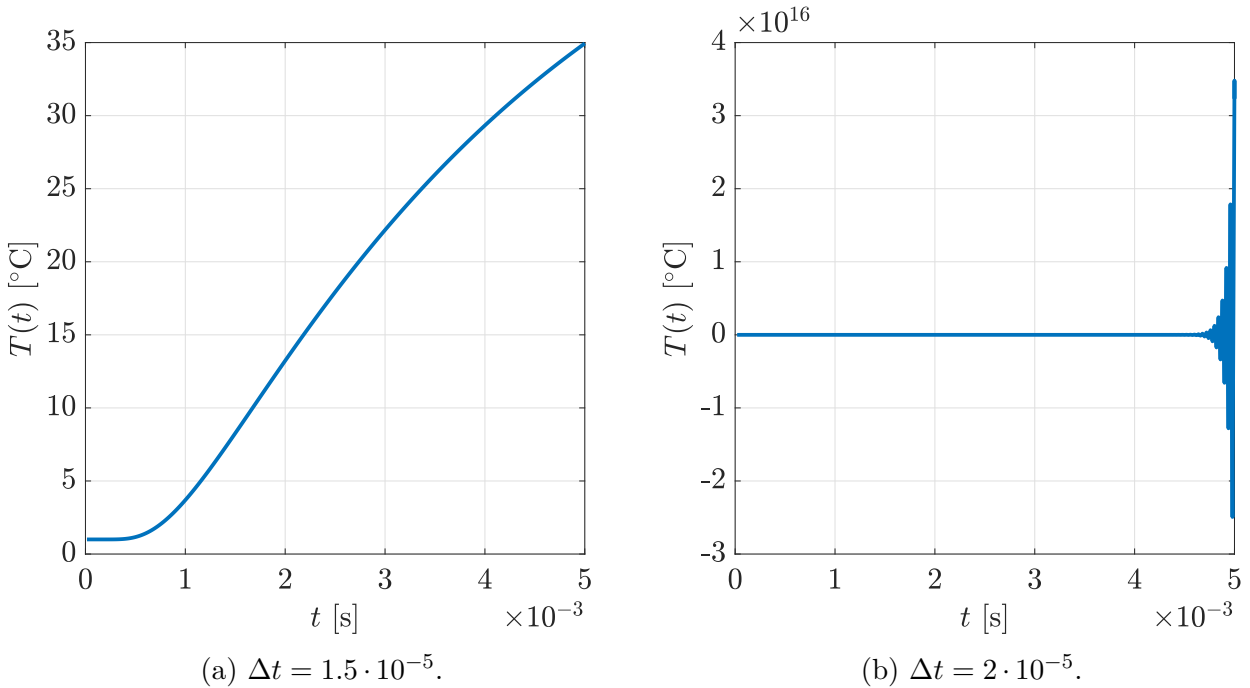


Figure 32: Temperature as a function of time for two values of Δt when using an explicit solver ($\theta = 0$).

2.4.2 Test on an implicit solver ($\theta = 1$)

In this part, the same test as previously is made using an implicit solver ($\theta = 1$). This implies that there should be no restriction in the choice of Δt , as per the criterion that was established.

FIGURE 33 shows the evolution of the temperature as a function time for the same Δt considered previously. However, in both cases, the expected behaviour seems to be recovered, which was not the case with $\theta = 0$

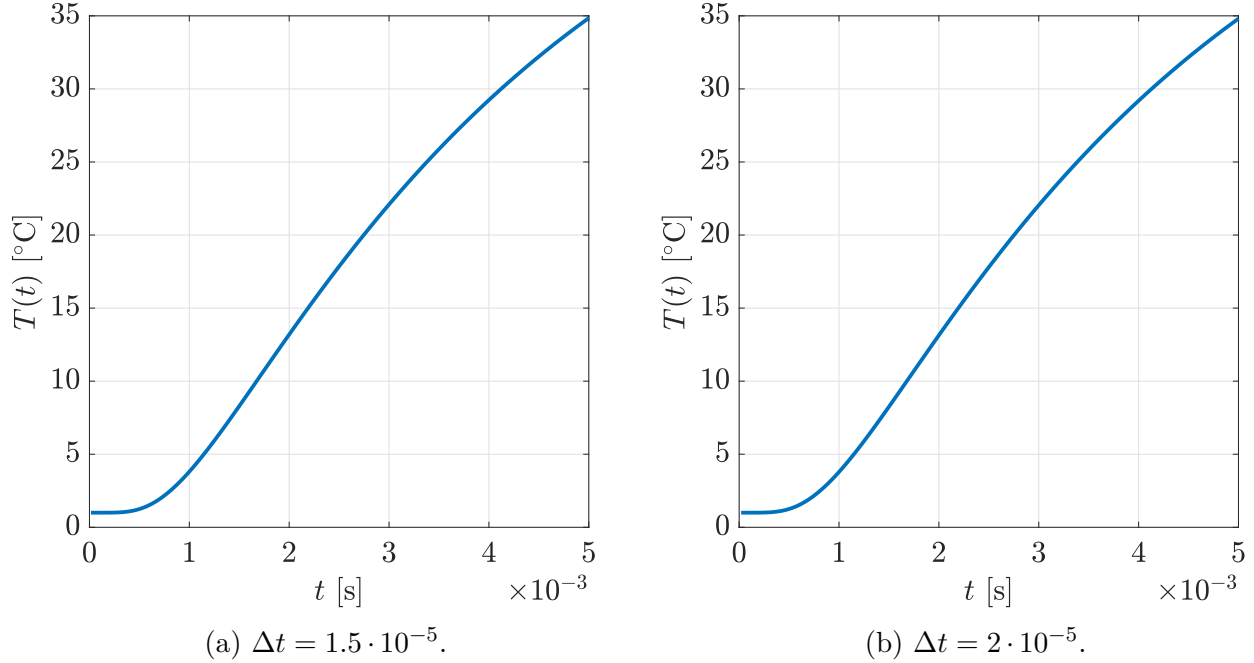


Figure 33: Temperature as a function of time for two values of Δt when using an explicit solver ($\theta = 1$).

2.5 Performance

In this section speed up, efficiency and weak scaling are analyzed. The standard test for strong scaling uses a mesh of dimensions N^3 with $N = 30$, where N is the number of points in one direction. This corresponds to a box with the following dimensions: $L_x = L_y = L_z = 0.3[m]$ and $\Delta L = 0.01[m]$. The time step is fixed at $0.001[s]$.

2.5.1 Strong scaling

The number of threads used for OpenMP is set to one while the number of processes for OpenMPI is progressively increased from 1 to 8. Speed up and efficiency curves are given in figure 34. The total running time was used to derive them. It contains the filling of the premultiplying matrices as well as the computation of the right hand side. As it can be seen, efficiency decreases rapidly with the increase of the number of cores. Note that speed up is around 1.3 for 8 processes. As a comparison, for the same number of processes the electromagnetic solver has a speed up of 6. Scaling with OpenMP is extremely disappointing as can be observed in table 5.

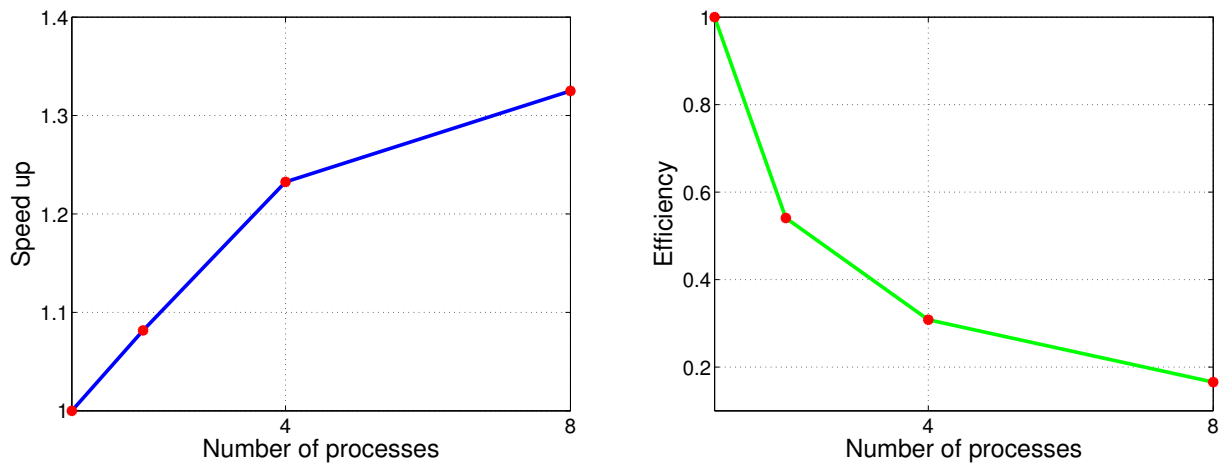


Figure 34: MPI: Speed up and efficiency curves of strong scaling for $L = 0.3[m]$ and 500 time steps. $\Delta L = 0.01[m]$ and $\Delta t = 0.001[s]$.

Number of threads for OpenMP	Run time [s]
1	53
2	52
4	52
8	51
16	51

Table 5: Total run time: OpenMP for $L = 0.3[m]$ and 500 time steps. $\Delta L = 0.01[m]$ and $\Delta t = 0.001[s]$.

2.5.2 Weak scaling

The cube's characteristic length was multiplied by t_0 , while the number of cores used by OpenMPI was multiplied by 8. The total running time was 848[s], which is significantly longer than expected.

Chapter 3

Coupled electromagnetic-thermal solver

At this stage two independant solvers were implemented, one solving the electromagnetic equations and the other solving thermal problems. The aim of this chapter is to take advantage of these two solvers and make them communicate. By doing so, the obtained implementation will be able to model the heating of food inside a microwave oven. Indeed, the aforementioned model can be obtained by following the flowchart shown in FIGURE 35:

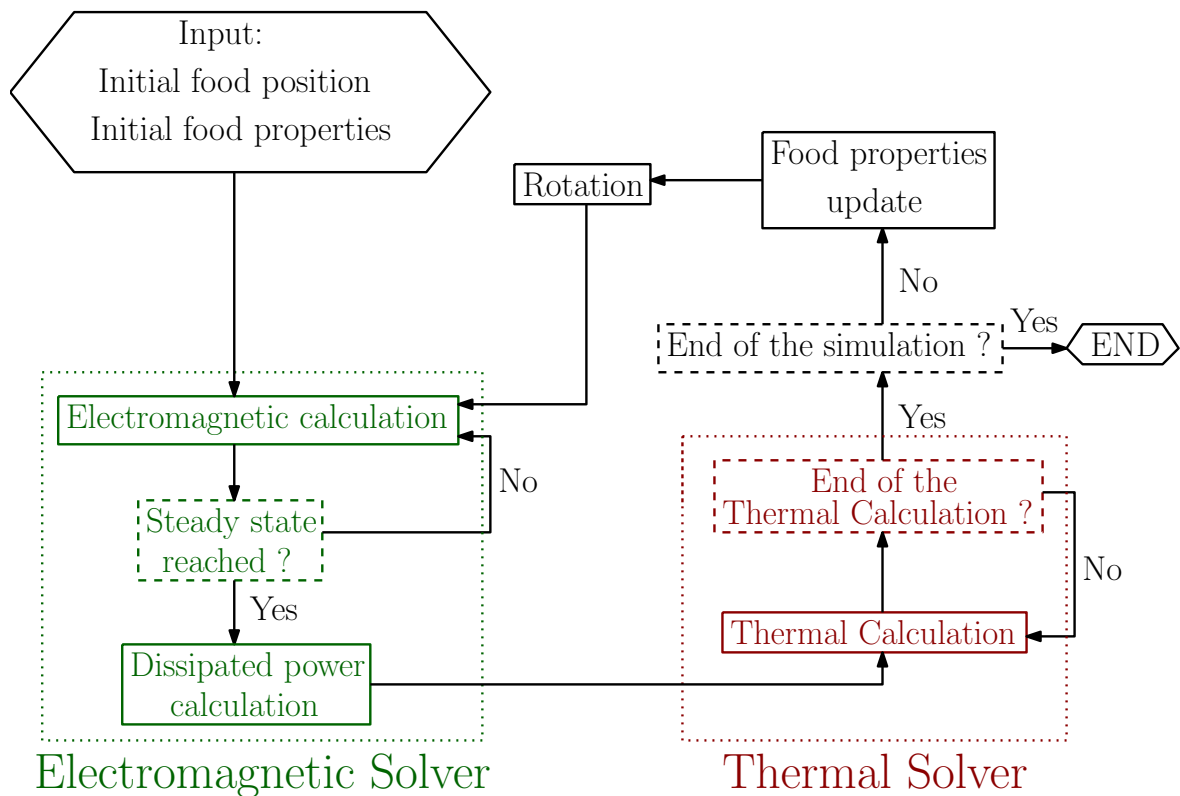


Figure 35: Flow chart of the coupled solver.

In this graph, it can be noticed that the food is maintained at the same position during the electromagnetic calculations. This can be justified by considering that the steady state is

reached much faster than the time needed to make the food rotate by a small angle, which will be shown later. Furthermore, as already mentioned during a whole thermal calculation, the electromagnetic field is assumed to remain the same. Once again, this assumption is justified by considering that the electromagnetic steady state is reached very fast and remains thus constant afterwards.

In the following, the main steps involved in the coupled solver are thus presented and discussed. Indeed, first of all, the calculation of the dissipated power inside the food from the knowledge of the electric and magnetic fields is discussed. After that, the method used to verify if the steady state configuration has been reached is also presented. Then, the way the possible phase transitions of the food is implemented as well as the handling of the rotation of the food inside the microwave oven field are discussed. Finally, the model used for representing a realistic input electromagnetic field is detailed.

3.1 Calculation of the dissipated power

As it has been previously mentioned, the aim of the electromagnetic calculation is to find the value of the electric and magnetic field in the steady state configuration. From this knowledge the power dissipated in the food can be deduced as it is shown in this section. This dissipated power is generated because of the electromagnetic field and two different phenomena contribute to it. The first one is the Joule effect which is linked to a current flow inside the food and can be computed as follows:

$$P_{Joule} = \vec{J} \cdot \vec{E} = \sigma E^2, \quad (3.1)$$

where \vec{J} is the current density, σ is the conductivity and E denotes the amplitude of the electric field.

However, in the framework of this project, the food placed inside the domain will have very low conductivity and consequently, the power dissipated by Joule effect will be very small. Therefore, in order to simplify the calculation, this contribution to the dissipated power will be neglected which is equivalent to assume that the conductivity of the food is equal to zero.

Besides that the second contribution consists in the dielectric losses inside the food. These losses are associated to the periodic re-orientation of dielectric dipoles induced by the electric field. They can be modelled by adding an imaginary part to the relative permittivity of the food:

$$\varepsilon_r = \varepsilon' - j \varepsilon'', \quad (3.2)$$

where ε' is linked to the polarization of the food, and ε'' stands for the dielectric losses.

The value of ε'' can be found in tables for different materials. Therefore, the volumic dissipated power associated to the dielectric losses can be expressed as follows:

$$P_{diel} = 2 \pi f \varepsilon_0 \varepsilon'' E^2, \quad (3.3)$$

where f is the frequency of the signal and ε_0 is the electric permittivity of vacuum.

Therefore, using this last relation, the value of the dissipated power can be computed at some grid points. Indeed, as a reminder, the value of the different fields at each step is supposed to be known at some grid points as shown in FIGURE 2.

Using the same indices as before, one can approximate the amplitude of the electric field at the center of the cubic cell shown in FIGURE 2 as follows:

$$\begin{aligned}
 E_{i,j,k}^2 = & \frac{\left(Ex_{i+\frac{1}{2},j,k}\right)^2 + \left(Ex_{i+\frac{1}{2},j+1,k}\right)^2 + \left(Ex_{i+\frac{1}{2},j,k+1}\right)^2 + \left(Ex_{i+\frac{1}{2},j+1,k+1}\right)^2}{4} \\
 & + \frac{\left(Ey_{i,j+\frac{1}{2},k}\right)^2 + \left(Ey_{i+1,j+\frac{1}{2},k}\right)^2 + \left(Ey_{i,j+\frac{1}{2},k+1}\right)^2 + \left(Ey_{i+1,j+\frac{1}{2},k+1}\right)^2}{4} \\
 & + \frac{\left(Ez_{i,j,k+\frac{1}{2}}\right)^2 + \left(Ez_{i+1,j,k+\frac{1}{2}}\right)^2 + \left(Ez_{i,j+1,k+\frac{1}{2}}\right)^2 + \left(Ez_{i+1,j+1,k+\frac{1}{2}}\right)^2}{4}.
 \end{aligned} \tag{3.4}$$

It can also be highlighted that this calculation is made in order to know the value of the dissipated power inside the food. Therefore, if the food is not too close to the boundary, the equation (3.4) can always be used and no particular case has to be taken into account. Furthermore, this calculation gives the strength of the electric field at a given step. However, the interesting quantity is the average value of the dissipated power. Therefore, one can compute the average value of the strength of the electric field by averaging the value obtained in (3.4) over several number of periods of the input signal. It has to be highlighted that this average is computed once the electromagnetic steady state is reached. After that, the obtained power grid can be used by the heat equation solver as a source term.

As already mentioned, it is important to notice that the numerical scheme employed by the electromagnetic solver does not take into account any physical dissipation. Therefore, the electromagnetic steady state configuration is actually computed by assuming that there is no dissipation at all. It is only once this steady state configuration has been computed that the results are used in order to compute a dissipated power. Consequently, a further improvement of the electromagnetic solver can be to introduce some dissipation in the scheme.

3.2 Verification of the steady state

As previously mentioned, a criterion is required in order to determine if the electromagnetic computation has to continue or if the steady state has been reached. However, the establishment of this criterion is not straightforward. Indeed, the evolution of the electric field as a function of time inside the micro wave oven appears to be very complex and strongly dependent on the food placed inside. As an illustration, FIGURE 36 shows the time evolution of the amplitude of the electric field at the centre of a cubic food of dimension $0.05 \times 0.05 \times 0.05[m^3]$ placed at the centre of the microwave oven:

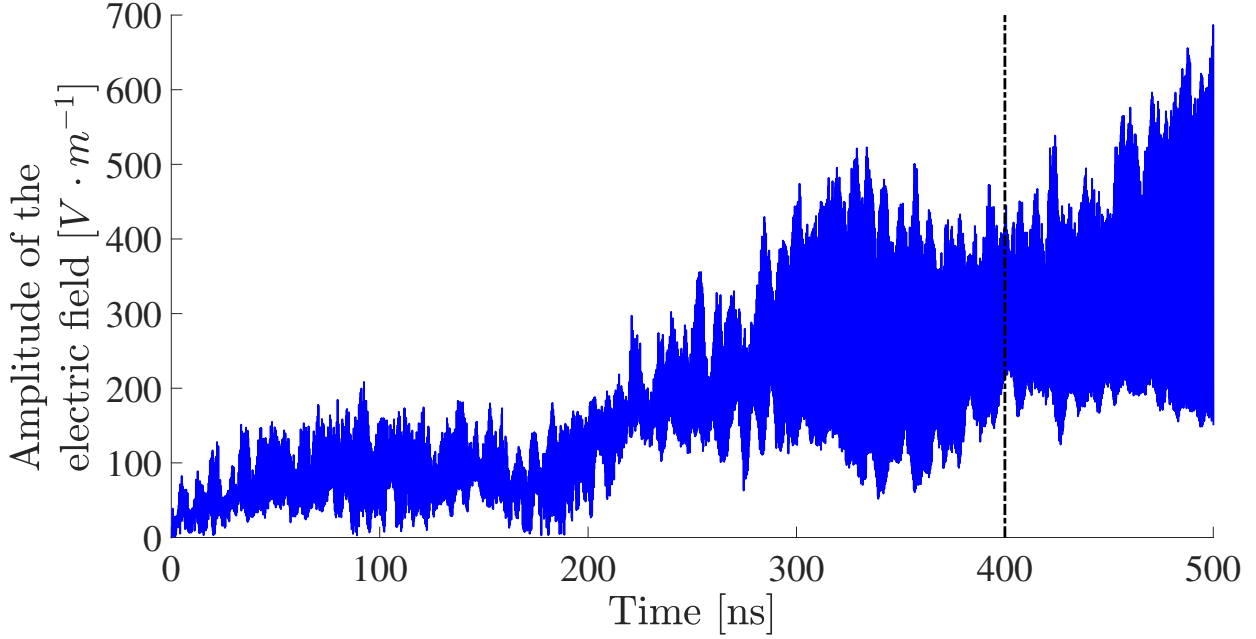


Figure 36: Evolution of the amplitude of the electric field as a function of time. The value of the complex permittivity is $75.8 + j5$. The spatial and temporal steps were respectively equal to $5 [mm]$ and $5 \cdot 10^{-3} [ns]$.

This evolution has been obtained by choosing a wave guide as input for the electromagnetic solver as explained in a following section. The amplitude E_0 of the fields for the wave guide was set to $500 [V \cdot m^{-1}]$.

Therefore, the general method used to determine if the steady state has been reached or not consists in computing an average dissipated power at some grid points and evaluate the moment at which this average power becomes quite stationary. More precisely, a grid of dissipated power is computed at each time step as explained in the previous section. Then, the result is integrated over a time which is large compared to the period of the input electric fields in order to obtain a grid of average dissipated power. Finally, each time the end of an integration period is reached, the difference between the average dissipated power at the current integration period and the previous one is evaluated as follows:

$$\Delta P = \sum_i \sum_j \sum_k \left(P_{i,j,k}^n - P_{i,j,k}^{n-1} \right)^2, \quad (3.5)$$

where $P_{i,j,k}^n$ is the average dissipated power for the current period of integration and $P_{i,j,k}^{n-1}$ stands for the average dissipated power for the previous period of integration.

Finally, the steady state is considered to be reached when ΔP is sufficiently small compared to the amplitude of the average dissipated power for the previous period of integration. More precisely, the following criterion is verified:

$$\frac{\Delta P}{||P^{n-1}||^2} < \varepsilon, \quad (3.6)$$

where ε is a dimensionless tolerance. This tolerance strongly affects the computation time, it is fixed to 10% in the implementation which generally leads to an acceptable electromagnetic calculation time. In equation (3.6) the amplitude of the average dissipated power is computed as follows:

$$||P^{n-1}||^2 = \sum_i \sum_j \sum_k (P_{i,j,k}^{n-1})^2 \quad (3.7)$$

Applying this criterion to the illustration case considered above with an integration period of 50 [ns] leads to stop the electromagnetic calculations at the time highlighted by the black vertical line in FIGURE 36. As it can be noticed, at this time, the amplitude of the electric field still varies with time but the mean value does not vary much anymore.

3.3 Phase transition

In this section the way the solver handles the temperature dependence of the different parameters is detailed. Indeed, after having carried out a thermal calculation, the temperature field changes. Therefore, if the permittivity, the thermal conductivity, the density and the specific heat capacity depend on temperature, they have to be updated.

In the framework of this project, only the change of properties occurring in the neighbourhood of a phase transition inside the food are taken into account. These modifications are the most significant, but a further improvement of the solver can consist in updating continuously the different properties with the temperature. Furthermore, a very simple model of phase transition is used here. Indeed, it simply consists in assessing the temperature of every points of the food after each thermal calculation and updating the properties accordingly. Once more, a more complex model of the phase transition, taking into account the latent heat could be developed to improve the implementation.

Finally, it should also be highlighted that the update of the properties is carried out only after the whole thermal calculation. Therefore, if the thermal simulation is too long, it could occur that a point heats up above the phase transition temperature without seeing its properties changed. This problem could be solved by updating the properties at each step during the thermal calculation. Nevertheless, this way of updating the properties would require to invert the matrix $[\mathbb{I} - A]$ (see heat equation solver) at each step, which would increase significantly the computational cost of the simulation. With the current implementation, it is however possible to change the rate at which the properties are updated by changing the duration of a single thermal calculation without modifying the total duration of the whole simulation.

After that, a simple simulation was run in order to test the handling of phase change. It consisted in solving the heat equation inside a cube with a uniform heat source inside, submitted to homogeneous Neumann boundary condition. Using those assumption, the heat equation reduces to

$$\frac{\partial T}{\partial t} = \frac{Q}{\rho_i c_{p,i}},$$

where $i = 1, 2$ are the thermal properties taken before and after the phase change. It can be

solved, leading to the following exact solution:

$$\begin{cases} T(t) = \frac{Q}{\rho_1 c_{p,1}} t + T_0 & \text{for } 0 < t < t_1, \\ T(t) = \frac{Q}{\rho_2 c_{p,2}} t + T_\varphi - (T_\varphi - T_0) \frac{\rho_1 c_{p,1}}{\rho_2 c_{p,2}} & \text{for } t > t_1, \end{cases}$$

where $t_1 = (T_\varphi - T_0) \frac{\rho_1 c_{p,1}}{Q}$ is the time at which the phase change occurs, T_0 is the initial temperature, and T_φ is the phase change temperature.

The exact solution, as well as the numerical solution are shown in FIGURE 37. Note that, in the analytic model, the phase change temperature was chosen such that it fits to the one given by the numerical model, since the properties are not updated at every thermal step. The numerical solution seems to fit in a relatively accurate way.

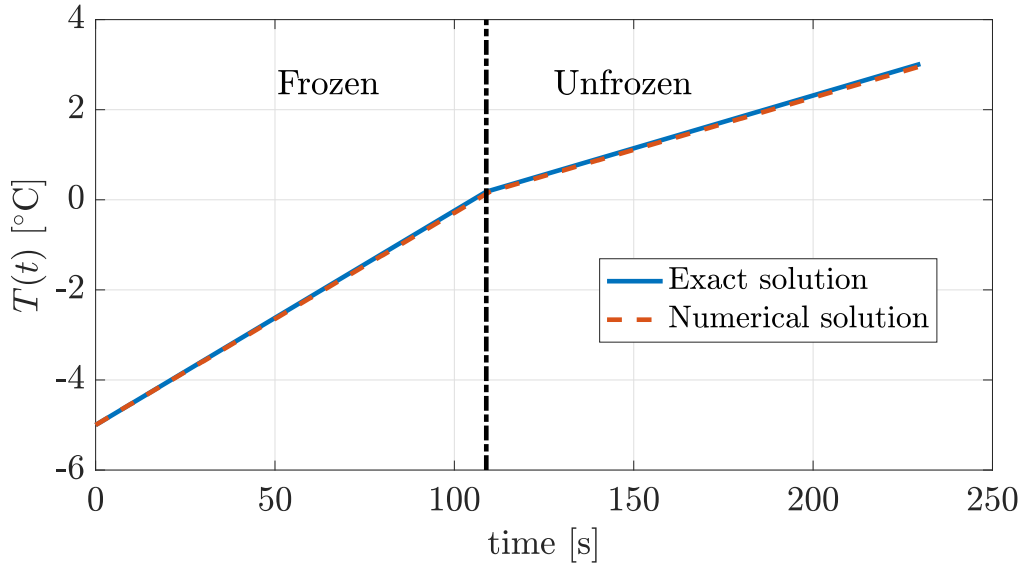


Figure 37: Solution of the uniform heat equation when the food undergoes phase change, with a constant heat source. — $Q = 50000 \text{ [W} \cdot \text{m}^{-3}]$, $\rho_1 = 725 \text{ [kg} \cdot \text{m}^{-3}]$, $c_{p,1} = 1450 \text{ [J} \cdot \text{K}^{-1} \cdot \text{kg}^{-1}]$, $\rho_2 = 770 \text{ [kg} \cdot \text{m}^{-3}]$, $c_{p,2} = 2770 \text{ [J} \cdot \text{K}^{-1} \cdot \text{kg}^{-1}]$, $dt = 0.1 \text{ [s]}$, $T_0 = -5 \text{ [}^\circ\text{C]}$, $T_\varphi = 0.1795 \text{ [}^\circ\text{C]}$

Furthermore, FIGURE 38 shows the exact solution that is obtained when setting $T_\varphi = 0 \text{ [}^\circ\text{C]}$. It is interesting that, in this case, the numerical result still fits in an accurate way, despite having a change of slope that occurs later (when $T_{\varphi,\text{num}} = 0.1795 \text{ [}^\circ\text{C]}$).

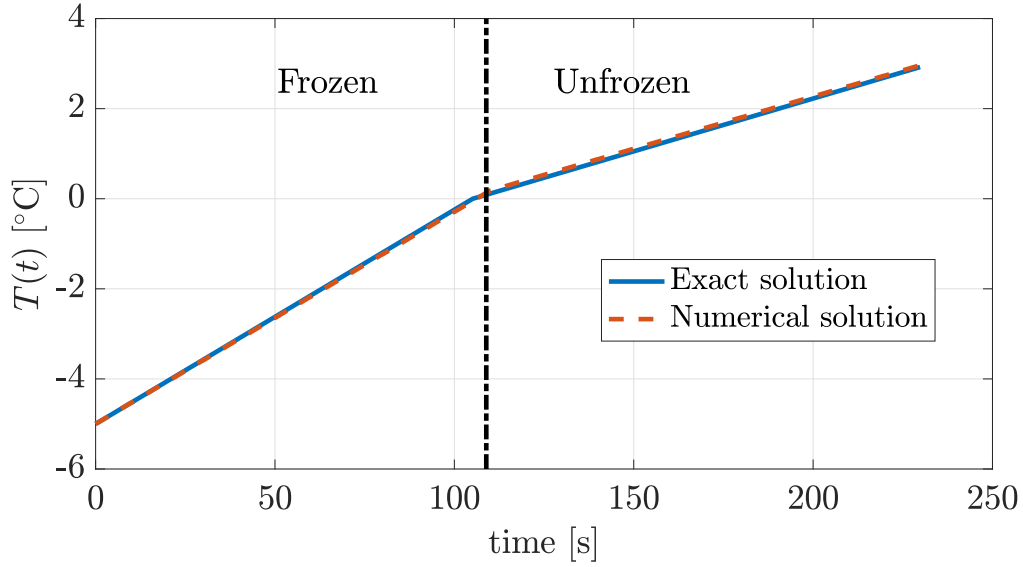


Figure 38: Solution of the uniform heat equation when the food undergoes phase change, with a constant heat source. — $Q = 50000 \text{ [W} \cdot \text{m}^{-3}]$, $\rho_1 = 725 \text{ [kg} \cdot \text{m}^{-3}]$, $c_{p,1} = 1450 \text{ [J} \cdot \text{K}^{-1} \cdot \text{kg}^{-1}]$, $\rho_2 = 770 \text{ [kg} \cdot \text{m}^{-3}]$, $c_{p,2} = 2770 \text{ [J} \cdot \text{K}^{-1} \cdot \text{kg}^{-1}]$, $dt = 0.1 \text{ [s]}$, $T_0 = -5 \text{ [}^\circ\text{C]}$, $T_\varphi = 0 \text{ [}^\circ\text{C]}$

However, this is not the behaviour that is expected in a microwave oven. Indeed, only the variation of the thermal parameters was considered in the calculation, when, for instance, dielectric properties of the food that undergoes a phase change also vary with temperature, hence changing the heat source.

Besides that, it should also be highlighted that for this simple case, only two different value of the properties were considered for the phase transition. In practice, the implementation is able to handle a larger number of discrete value for the properties in the neighbourhood of the phase transition.

3.4 Implementation of the rotation

An other complexity encountered when trying to model the functioning of a microwave oven is to handle the rotation. In this section, the method employed to implement it is exposed in two steps. The first one is the explanation of the rotation of the food itself. After this, the solving of the heat equation on a domain which is actually moving in space is not straight forward. Two different approaches will be considered and discussed to overcome this difficulty.

3.4.1 Rotation of the food

This section exposes the approach used to rotate the object inside the electromagnetic grid. In the implementation, the object is defined by a matrix in which the components that are equal to zero correspond to grid points in air and in which the non zero components correspond to grid points inside an other material.

The general idea consists in rotating the configuration at the current time step back to where it was in the initial configuration, where the location of the food is supposed to be known. Then it is checked if a given point belonged to the food or to the volume containing air in this initial

configuration. It should be highlighted that inside the microwave oven, the rotation occurs around the z axis, which simplifies the equations as the z coordinate is not modified during the rotation. The general reasoning used to carry out the rotation is illustrated on a cubic food in FIGURE 39:

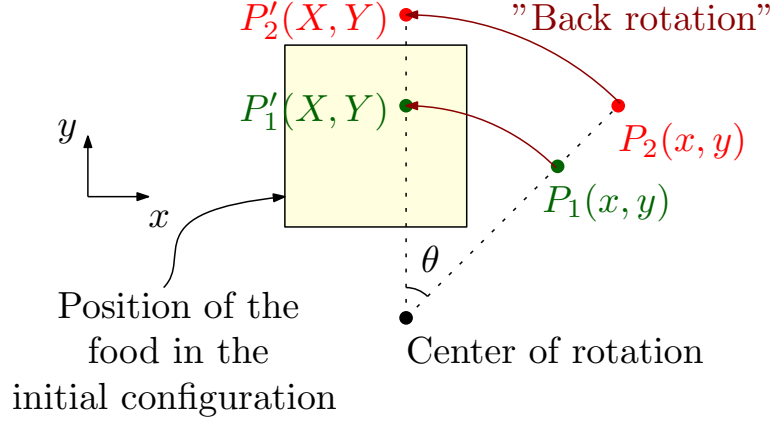


Figure 39: Scheme depicting the method used to rotate the object inside the domain. $\mathbf{X} = [X \ Y]^T$ are the coordinates of point P in the reference configuration, whereas $\mathbf{x} = [x \ y]^T$ are the coordinates of point P in the current configuration. The angular displacement is denoted by θ . Here, P_1 is inside the food and P_2 is inside the air volume.

Let $\mathbf{x} = [x \ y]^T$ be the position of a point P in the current configuration. There is no need for taking component z into account, since the rotation is around the z axis and the z component of any point will therefore remain the same during the rotation. Knowing the angular velocity $\dot{\Theta}$ one can compute the angular displacement of each point using $\Theta = \dot{\Theta}T$, where T is the time elapsed since the beginning of the simulation. If $\mathbf{X} = [X \ Y]^T$ denotes the position of P in the reference configuration (before any rotation), then the relation between \mathbf{X} and \mathbf{x} is given by a simple rotation matrix:

$$\begin{bmatrix} X \\ Y \end{bmatrix} \begin{bmatrix} \cos \Theta & \sin \Theta \\ -\sin \Theta & \cos \Theta \end{bmatrix} = \begin{bmatrix} x \\ y \end{bmatrix} \quad (3.8)$$

Since the position of the object is supposed to be known in the reference configuration one can now check if P was inside the object or not. This is done by going back to the cartesian equation that defines the object. Let us consider the example of a sphere. $P(x, y)$ will be considered inside the object if $(X - X_c)^2 + (Y - Y_c)^2 + (Z - Z_c)^2 \leq R^2$, where $C(X_c, Y_c, Z_c)$ is the center of the sphere in the initial configuration and R is the radius of the sphere. Using this method does not deform the object from time step to time step, since the geometry is always defined in the same way.

3.4.2 Solving of the problem after the rotation

First of all, it can be highlighted that the rotation will not bring any new difficulties for the electromagnetic part of the problem. Indeed, the aim of the electromagnetic solver is to determine the steady state configuration in order to infer the value of the dissipated power as a function of the position inside the domain. Therefore, the electromagnetic grid can be kept fixed and the geometry can simply be rotated inside this grid as explained in the previous section.

Finally, the steady state configuration using the new geometry can be found by employing the electromagnetic solver with rest initial condition. Consequently, the initial condition of the problem after the rotation can be chosen completely independently from the final configuration of the system before carrying out the rotation. Therefore, there is no need to compute any link between the components of the electric and the magnetic fields before and after the rotation.

However, things are different for the thermal part of the problem. Indeed, the initial temperature field inside the food after the rotation has to be the same as the final one before the rotation. Because of that, the initial condition of the thermal problem for a given position of the food can not be chosen independently from the final condition of the problem for the previous position of the food. Consequently, a method to link the rotated and the unrotated configuration is required to solve the thermal problem. In this section, two possible solutions will be presented and compared in terms of complexity and accuracy. Nevertheless, before that, a first short section is dedicated to the difference between the Eulerian and Lagrangian representation of the problem.

Eulerian and Lagrangian representation of the heat equation

If one wants to solve a problem in which there is a non negligible motion of a body using conservation laws, there are two well known approaches that can be considered. The first one consists in solving the problem by using a control volume which is moving with the body of interest and is called the Eulerian approach. In this framework, let us consider the equation governing the conservation of the thermal energy for a system in which there is a volumetric power source denoted Q . If one performs the integrals on moving control volumes, the conservation law can be expressed as follows:

$$\frac{d}{dt} \int_{\Omega(t)} \rho c_p T dV - \int_{\partial\Omega(t)} k \nabla T \cdot \mathbf{n} dS = \int_{\Omega(t)} Q dV, \quad (3.9)$$

$$\Leftrightarrow \int_{\Omega(t)} \rho c_p \frac{DT}{Dt} dV - \int_{\partial\Omega(t)} k \nabla T \cdot \mathbf{n} dS = \int_{\Omega(t)} Q dV, \quad (3.10)$$

where ρ is the density, c_p is the specific heat capacity, \mathbf{n} is the unit outward normal and where the Reynold theorem was used to obtain the second expression. Using Gauss theorem, the local version of this equation can be written as follows:

$$\rho c_p \frac{DT}{Dt} - \operatorname{div}(k \nabla T) = Q. \quad (3.11)$$

Therefore, the classical heat equation is recovered with this reasoning. It should be highlighted that the time derivative appearing in this equation is the total time derivative, but it corresponds to a simple time derivative in the frame which is moving with the body. However, it will not be the case anymore if one uses a Lagrangian approach. Indeed, let us consider the same conservation equation but this time expressed on a fixed control volume:

$$\frac{d}{dt} \int_{\Omega} \rho c_p T dV + \int_{\partial\Omega} (\rho c_p T \mathbf{v} - k \nabla T) \cdot \mathbf{n} dS = \int_{\Omega} Q dV, \quad (3.12)$$

$$\Leftrightarrow \frac{\partial(\rho c_p T)}{\partial t} + \operatorname{div}(\rho c_p T \mathbf{v}) - \operatorname{div}(k \nabla T) = Q, \quad (3.13)$$

where \mathbf{v} is the velocity and where the Gauss theorem was applied to obtained the second expression. Therefore, it appears that if one wants to use a Lagrangian approach, a new term has to be added in the equation which is called the convective term. The two approaches that are presented in the next sections are both Eulerian and consequently, this convective term will not be considered.

Fixed temperature grid

A first method to solve the heat equation can be obtained by following exactly the same reasoning as with the rotation of the geometry in the electromagnetic grid. Indeed, the thermal grid could be kept fixed and the final temperature field before rotation could be rotated the same way as the geometry as shown in FIGURE 40:

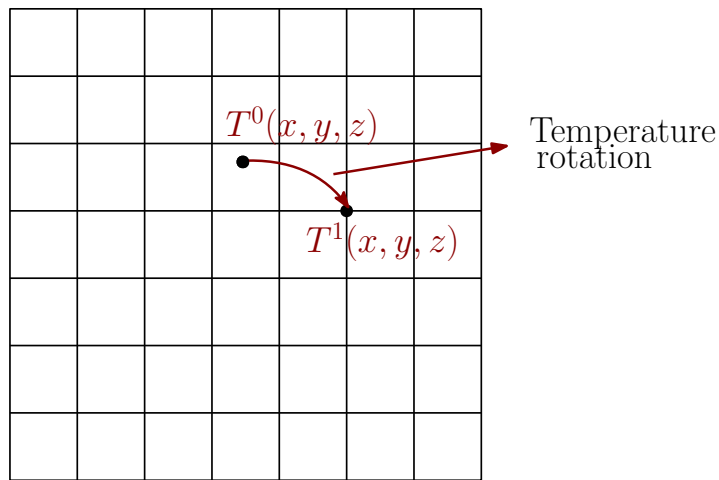


Figure 40: Representation of the rotation of the temperature inside a fixed thermal grid. $T^0(x, y, z)$ is the temperature field before rotation and $T^1(x, y, z)$ is the temperature field after rotation.

By doing so, a difficulty can be found in the fact that the thermal grid points after the rotation do not necessarily correspond to grid points before being rotated as it can be seen in FIGURE 40. Therefore, an interpolation algorithm has to be used to compute the value of the temperature inside a cell of the thermal grid. As the z -component of any point does not change during the rotation, a bi-linear interpolation can be used for this purpose. Indeed, let us consider the calculation of the temperature inside the following cell:

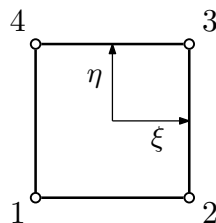


Figure 41: Representation of a cell of the thermal grid.

Knowing the value of the temperature at each corner of the cell, the bi-linear interpolation consists in approximating the temperature at any point inside the cell by the following expression:

$$T^0(\xi, \eta) = \frac{1}{4} \left(T_1^0 (1 - \xi) (1 - \eta) + T_2^0 (1 + \xi) (1 - \eta) + T_3^0 (1 + \xi) (1 + \eta) + T_4^0 (1 - \xi) (1 + \eta) \right) \quad (3.14)$$

Once this interpolation has been carried out, the rotated temperature field can be used as initial condition and the thermal problem can be solved. The advantage of this method is that the thermal and the electromagnetic grid are always oriented the same way and because of that the mapping between those two grids will not present any particular difficulty.

Rotating thermal grid

A second approach consists in making the thermal grid rotate with the food inside the electromagnetic grid as shown in FIGURE 42:

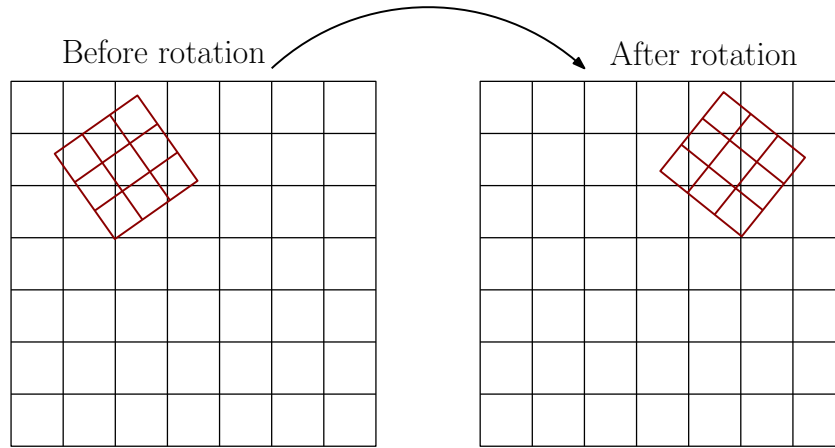


Figure 42: Representation of the rotation of the thermal grid. The black grid is the fixed electromagnetic grid, the red grid is the thermal one.

By doing this, the position and the orientation of the food inside the thermal grid will always remain the same which will greatly simplify the solving of the thermal problem as it will be discussed in the next subsection. However, using this reasoning, the thermal and the electromagnetic grid will not always correspond and moreover, their relative orientation will change with time. Therefore, an interpolation algorithm will be required to map the values of the dissipated power computed with the electromagnetic grid on the thermal grid. Once more, as the z -component of any point remains the same during the rotation, a bi-linear interpolation can be used.

Comparison between the two approaches

The two aforementioned ways of handling the rotation in the frame of the thermal solver have been implemented and the second approach seems to be the best suited for different reasons.

First of all, in terms of complexity, it has to be noticed that with the first method, the thermal problem that one has to solve changes each time the geometry rotates. Indeed, as the food changes its relative position in the thermal grid, the application of the Neumann boundary condition on the surface of the food changes as well. Consequently, the system of

equation is modified at each rotation and as a result, a new matrix inversion has to be carried out. On the other hand, as in the second approach the food does not change its relative position and orientation with respect to the grid, only the right hand side of the heat equation will be modified by the rotation. Because of that, the inversion of the matrix $[\mathbb{I} - A]$ (see the heat equation solver) has to be computed only once during the whole simulation which will be a non negligible gain of computation time.

Besides, in practice, it is easier to handle a grid in which the object is fixed. Indeed, as an example, let us consider the evolution of the temperature as a function of time inside the food. If the first method is used, one has to implement a way of probing the temperature at a location which is rotating with the food. However, if the second method is used, one can just probe the temperature at a fixed location on the thermal grid which is simpler to implement. This difference in difficulty is even more pronounced if one is interested in the evolution of the temperature as a function of the position inside the food along a line which is initially aligned with the x axis for example.

Finally, in terms of accuracy of the results, the second approach is also expected to be more appropriate. Indeed, if an object which has a different temperature than the ambient air is inserted inside the domain, the interpolation of the temperature field required for the first method will induce a non negligible numerical heat diffusion each time the food is rotated, which is not physical.

In order to highlight this unwanted diffusion, the following test has been carried out : a cylinder of initial temperature of 0°C is placed inside a domain of initial temperature equal to 20°C . The heat equation is not solved during the test, only the temperature field is being rotated and interpolated. Therefore, it is expected that the cylinder moves in the domain but remains at 0°C and that the environment also remains at its initial temperature. The initial configuration and the configuration after having carried out a rotation of respectively $\frac{\pi}{2}$ and 2π radian are presented in FIGURES 43, 44 and 45:



Figure 43: Initial temperature field for a cylinder whose axis is directed along the z direction and whose radius is equal to $0.05 [m]$. The domain is a cube of length equal $0.3[m]$ and the grid spacing is equal to $0.01[m]$.

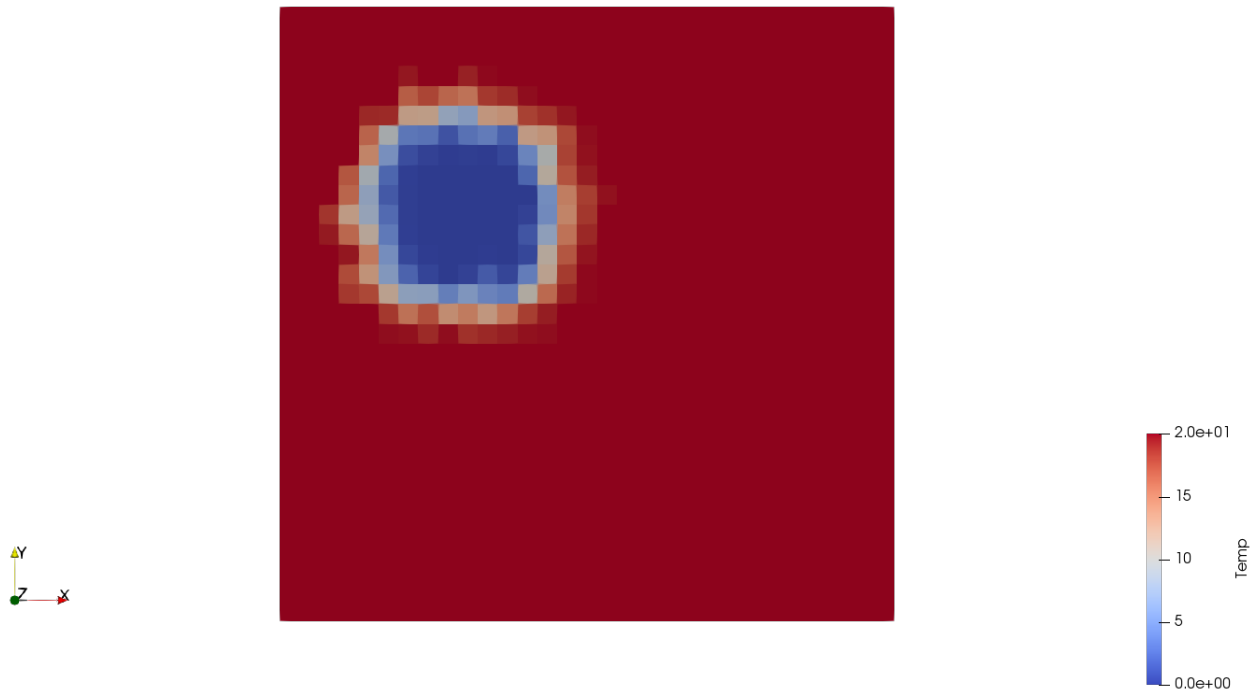


Figure 44: Temperature field for a cylinder whose axis is directed along the z direction and whose radius is equal to $0.05 [m]$ after a rotation of of $\frac{\pi}{2}$ radiant with a angular step of $\frac{\pi}{8}$ radiant. The domain is a cube of length equal $0.3[m]$ and the grid spacing is equal to $0.01[m]$.

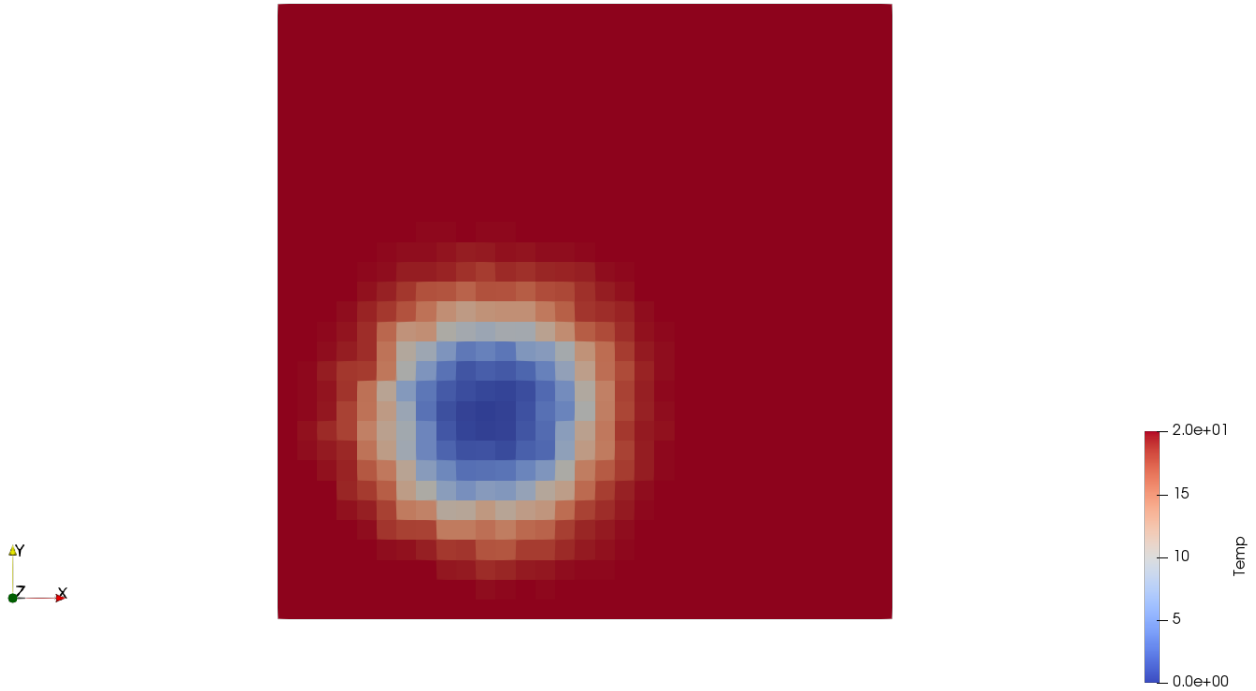


Figure 45: Temperature field for a cylinder whose axis is directed along the z direction and whose radius is equal to $0.05 [m]$ after a rotation of 2π radiant with a angular step of $\frac{\pi}{8}$ radiant. The domain is a cube of length equal $0.3[m]$ and the grid spacing is equal to $0.01[m]$.

As it can be seen in those FIGURES, even if no equation is solved by the solver, a purely numerical heat diffusion linked to the rotation of the food tends to smooth out the temperature field inside the domain. It can also be seen that the more the object is rotated, the more important the diffusion is. Therefore, if one uses this method to carry out the rotation, this numerical diffusion would add to the physical one and this could lead to completely wrong results.

Therefore, for all the reasons previously mentioned, the second approach will be used to handle the rotation for the thermal part of the problem.

3.5 Input field

At this stage, the coupled solver is able to solve an electromagnetic wave propagation problem and use the results as inputs to solve a heat propagation problem. The implementation being also able to handle rotation and phase transition, the last remaining step in order to obtain a numerical model for the microwave oven is to implement a realistic electromagnetic input. Actually, in a microwave oven, the input fields are generated thanks to a magnetron and are then transported through a waveguide. However, in the framework of this project, the functioning of the magnetron will not be modelled. The only quantity of interest will be the shape of the electromagnetic field at the end of the wave guide and everything occurring before will be assumed to work as theoretically expected. The position of the waved guide inside the oven as well as different geometrical parameters are presented in FIGURE 46:

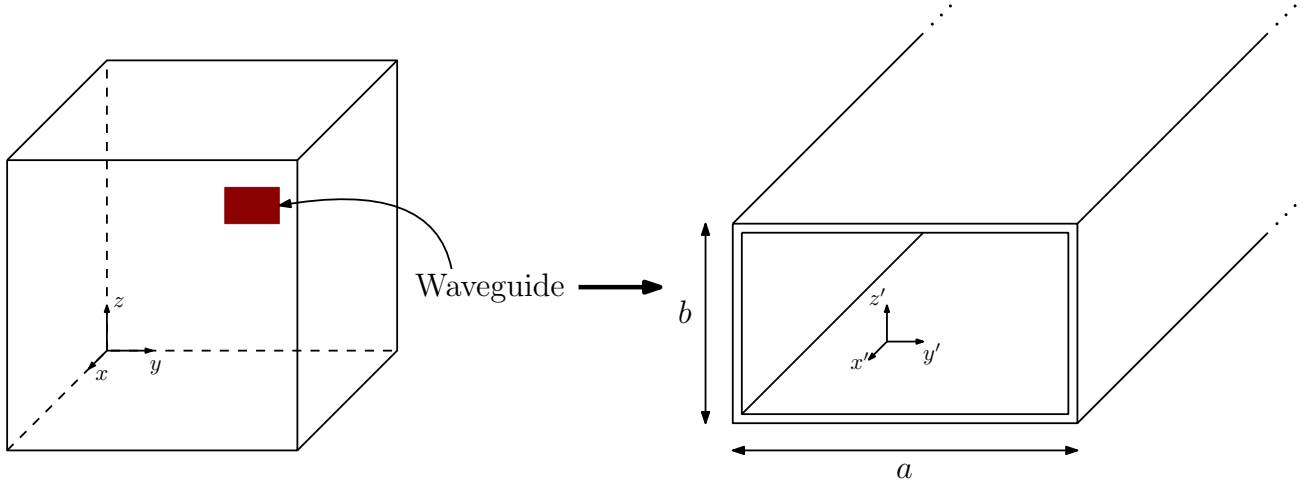


Figure 46: Schematic of the wave guide. The end of the wave guide is placed on the wall of the microwave oven of coordinate $x = 0$.

As a reminder, if the walls of the waveguide are assumed to be perfectly conducting, the only mode of propagations that can appears are transverse electric or transverse magnetic (TEM modes are not allowed). Here, it will be assumed that tranerse electric modes have been generated earlier and that there is a propagation along the waveguide. It can be shown analytically that such modes can propagate without being exponentially attenuated only if the frequency of the signal is sufficiently high [2]. More precisely, the exact shape of the modes considered at the end of the wave guide as well as the minimum frequency required to have a propagation are given in equations (3.15):

$$\begin{cases} E_{y;m,n}(y', z') = E_0 \cos\left(\frac{m\pi y'}{a}\right) \sin\left(\frac{n\pi z'}{b}\right), \\ E_{z;m,n}(y', z') = E_0 \sin\left(\frac{m\pi y'}{a}\right) \cos\left(\frac{n\pi z'}{b}\right), \\ f_{m,n}^c = \frac{1}{2\sqrt{\mu\epsilon}} \sqrt{\left(\frac{m}{a}\right)^2 + \left(\frac{n}{b}\right)^2}, \end{cases} \quad (3.15)$$

where m and n are positive integers.

Therefore, for simplicity purpose, the value of a and b were chosen in order to let only the first modes propagate. Indeed, a square waveguide of dimension $6.5 [cm] \times 6.5 [cm]$ with air inside of it leads to the following limit frequency:

$$\begin{aligned} f_{1,0}^c &= f_{0,1}^c = 2.3 [\text{GHz}], \\ f_{2,0}^c &= f_{0,2}^c = 4.6 [\text{GHz}], \\ f_{1,1}^c &= 3.3 [\text{GHz}]. \end{aligned} \quad (3.16)$$

It appears therefore that choosing an input frequency of $2.4 [\text{GHz}]$ will indeed lead to a propagation of the first modes only.

After that, as the geometry of the waveguide, the shape of the mode and the input frequency are now known, the only remaining quantity that has to be determined is the amplitude E_0 , which is not straight forward. Indeed, this amplitude is actually computed in order to impose

the total dissipated power inside the oven to be roughly equal to 750 [W], which is a typical order of magnitude for common microwave oven. However, as no dissipation has been taken into account in the numerical scheme, the whole food will strongly contribute to the dissipated power as the fields are not attenuated as they enters in the food. Therefore, it results that for a given amplitude E_0 , the total dissipated power obtained numerically will strongly depend on the volume of the food. Therefore, before launching a test on a new geometry of the food, a first step is always required which consist in running electromagnetic simulations in order to adjust the value of E_0 to obtained the desired total dissipated power at steady state.

Chapter 4

Heating of realistic food

Up to now, the coupled electromagnetic-thermal solver has been implemented and tested on simple configurations. Therefore, using the properly the implementation should allow us to solve numerically more realistic problems. By doing so, it is possible to highlight and interpret some interesting physical process actually occurring inside a microwave oven during the heating of some food.

In this chapter, a first case study is considered, which consists in the heating of a cylindrical bowl of soup. As it will be discussed, even for this quite simple problem, depending on the way the bowl is placed inside the microwave oven, the initial conditions and the type of microwave oven, the heating process can occur quite differently.

More particularly three different cases are considered in this chapter. Firstly, the bowl of soup will be placed at the center of the plate of the microwave oven and its initial temperature will be set to $10^{\circ}[C]$. Then, using the same initial temperature of the soup, the bowl will be placed away from the center. Finally, an initial temperature of $-5^{\circ}[C]$, will be considered in order to highlight the effect of a phase transition during the heating process. For each case, the time needed to make the temperature of the soup raise to $70^{\circ}[C]$ as well as the homogeneity of the temperature field will be discussed.

After this, the ability of the solver to handle more complex geometry of food is highlighted through the presentation of numerical results obtained for the heating of a chicken inside a microwave oven. For all the tests of this chapter, it should be highlighted that the simulations are carried out in a cubic microwave oven of 30 [cm] in side.

4.1 Unfrozen soup centered in the oven

As previously mentioned, the bowl is at first centered in the microwave oven and the initial temperature is set to $10^{\circ}[C]$. The geometry of the considered problem is shown in FIGURE 47. The exact value of the geometrical parameter of the bowl are respectively set to $R = 60\text{[cm]}$ and $H = 80\text{[cm]}$. In a first step, let us also consider that the microwave oven is not able to make the food inside of it rotate. Nevertheless, the effect of the rotation will be highlighted afterwards in this section, consequently the axis of rotation is already shown in FIGURE 47.

Before solving this problem numerically, it is necessary to find realistic value for the elec-

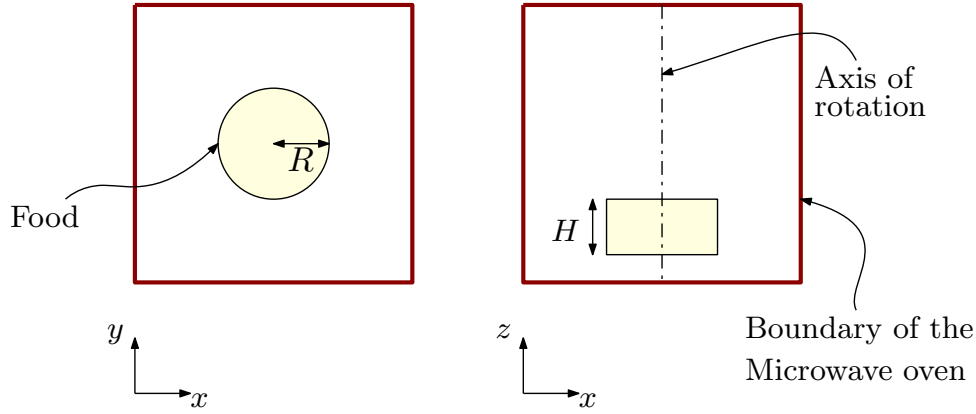


Figure 47: Representation of the geometry when the bowl of soup is centered inside the microwave oven.

tromagnetic and thermal properties of the soup. A simple approach is used here consisting in using the properties of water for the soup. This simplification is however reasonable as common soup usually contains more than 90% of water. The exact values used during the simulations are given in TABLE 6:

ε'	75.8 [—]
ε''	5 [—]
ρ	1000 [$kg \cdot m^{-3}$]
c_p	4200 [$J \cdot kg^{-1} \cdot K^{-1}$]
k	0.6 [$W \cdot m^{-1}$]

Table 6: Electromagnetic and thermal property of the soup placed in the microwave oven.

After that, for this configuration as well as for all the cases considered in this chapter, Robin boundary conditions are imposed on the surface of the food. Indeed, inside a real microwave oven, a fan induces an air motion. Therefore, imposing a convection condition on the surface of the food seems to be the best suited model of the heat transfer actually occurring between the air and the food. In order to impose this condition, the temperature of the air in the far field is set to 20°C and the convective heat transfer coefficient is set to 10 [$W \cdot m^{-2} \cdot K^{-1}$] which is a typical value for ambient air.

As a reminder, it should be highlighted that the amplitude of the input electric field is adjusted in order to dissipate roughly 750 [W] inside the soup. This condition leads to an input field amplitude of 2300 [$V \cdot m^{-1}$].

Therefore, using the previously mentioned parameter, a grid spacing of 5[mm] for both the electromagnetic and thermal problem and a temporal step of 5[ps] and 0.1[s] for the electromagnetic and thermal problem respectively, a simulation of 300 [s] was run. As already mentioned, the bowl was not rotated during the first simulation. During the analysis, the evolution of the temperature profile along two different directions as well as the time evolution of the temperature at a given point are considered. The exact position where the temperature is evaluated inside the bowl is shown on the initial configuration in FIGURE 48:

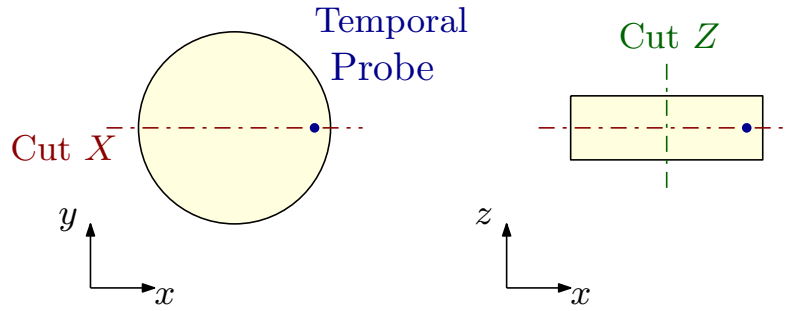


Figure 48: Representation of the position where the temperature is evaluated inside the bowl of soup.

The temperature profile along the two cuts obtained numerically for different time is represented in FIGURES 49 and 50:

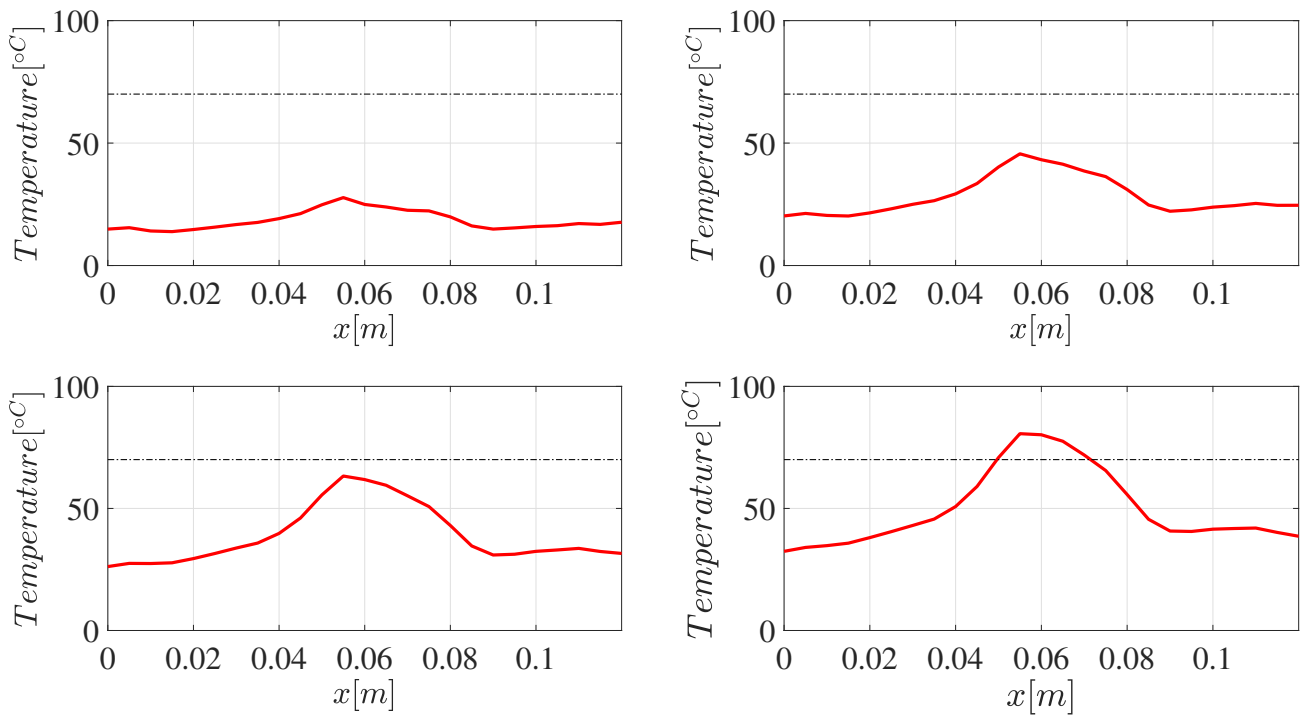


Figure 49: Representation of the temperature profile along the Cut X, without rotation, after respectively 75[s], 150[s], 225[s] and 300 [s] of simulation. The black line represent the aimed temperature level of 70°[C].

As it can be seen in FIGURE 49, the temperature of some points of the soup has reached 70°[C] after 300 [s] of heating. Nevertheless, it should also be highlighted that without rotation, the temperature inside the soup is not homogeneous at all such that most of the point inside the soup are still much cooler than 70°[C].

This observation can be understood by considering that the heat source generated by the microwave is not homogeneous in space. Indeed, this source can be quite high at some points

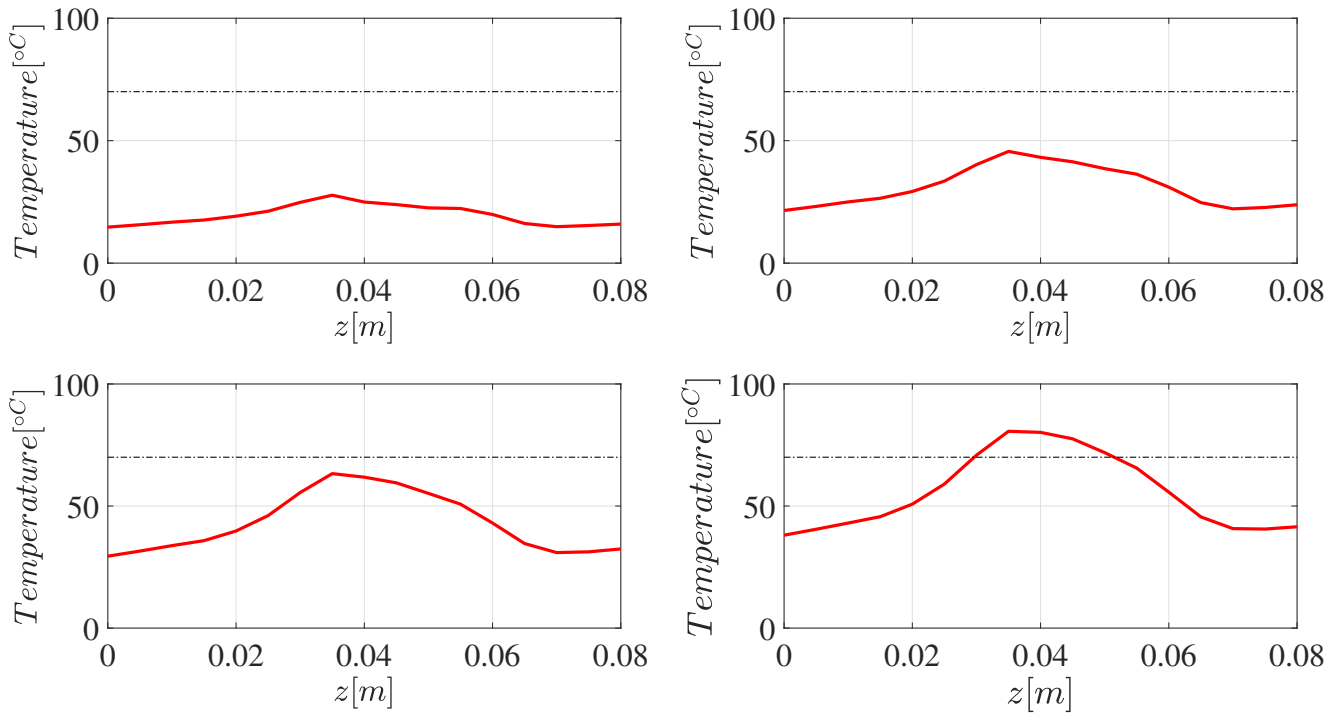


Figure 50: Representation of the temperature profile along the Cut Z, without rotation, after respectively 75[s], 150[s], 225[s] and 300 [s] of simulation. The black line represent the aimed temperature level of $70^{\circ}[C]$.

and almost vanish for some other points. Furthermore, without rotation, the spatial distribution of the heat source remain the same during the whole simulation and the position of the food inside this dissipated power field remains also identical. Because of that some points are mostly heated through conduction inside the soup explaining why their temperature rises at a slower rate. The evolution of the temperature at the temporal probe also highlights that the heat source does not change with time at this point. Indeed, as it can be seen in FIGURE 51 the time evolution temperature at this point does not present any irregularities.

After that, in order to attenuate this phenomenon of irregular temperature profile, one can make the bowl of soup rotate during the heating process. Indeed, the same simulation as the previous one has been run, the only difference consisting in the rotation of $\frac{2\pi}{10}$ radiant of the bowl every 2.5[s]. The resulting temperature profiles along the two considered cuts at different time are presented in FIGURES 52 and 53.

Therefore, it appears clearly that the rotation of the bowl has a direct impact on the homogeneity of the temperature profile. Indeed, it can be observed in FIGURE 52 and 53 that even if the temperature has not reached $70^{\circ}[C]$ everywhere in the bowl, the temperature is globally much closer to this level than without rotation. Nevertheless, the heating process still presents some non homogeneity. For instance, it seems that the center of the soup heats up more than the center.

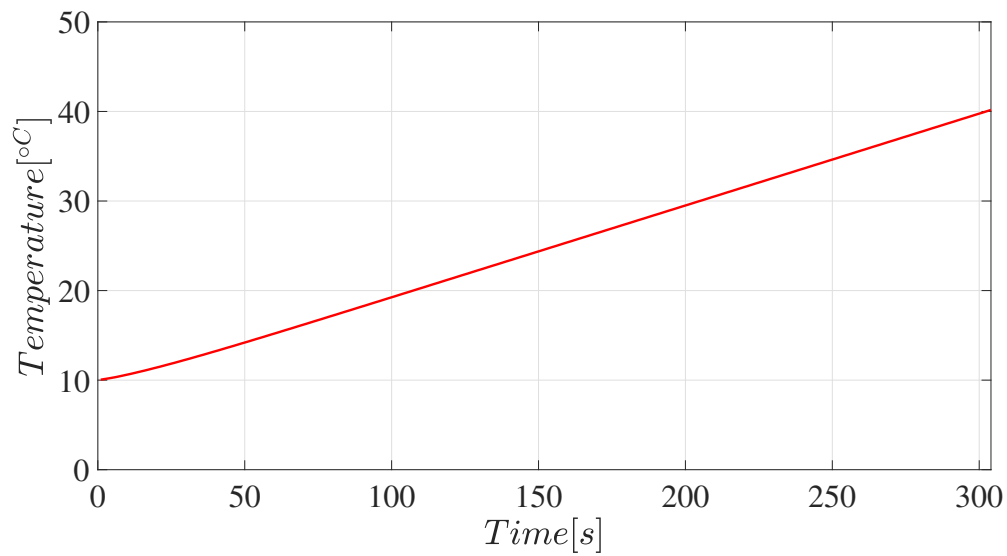


Figure 51: Time evolution of the temperature at the temporal probe placed inside the soup without rotation.

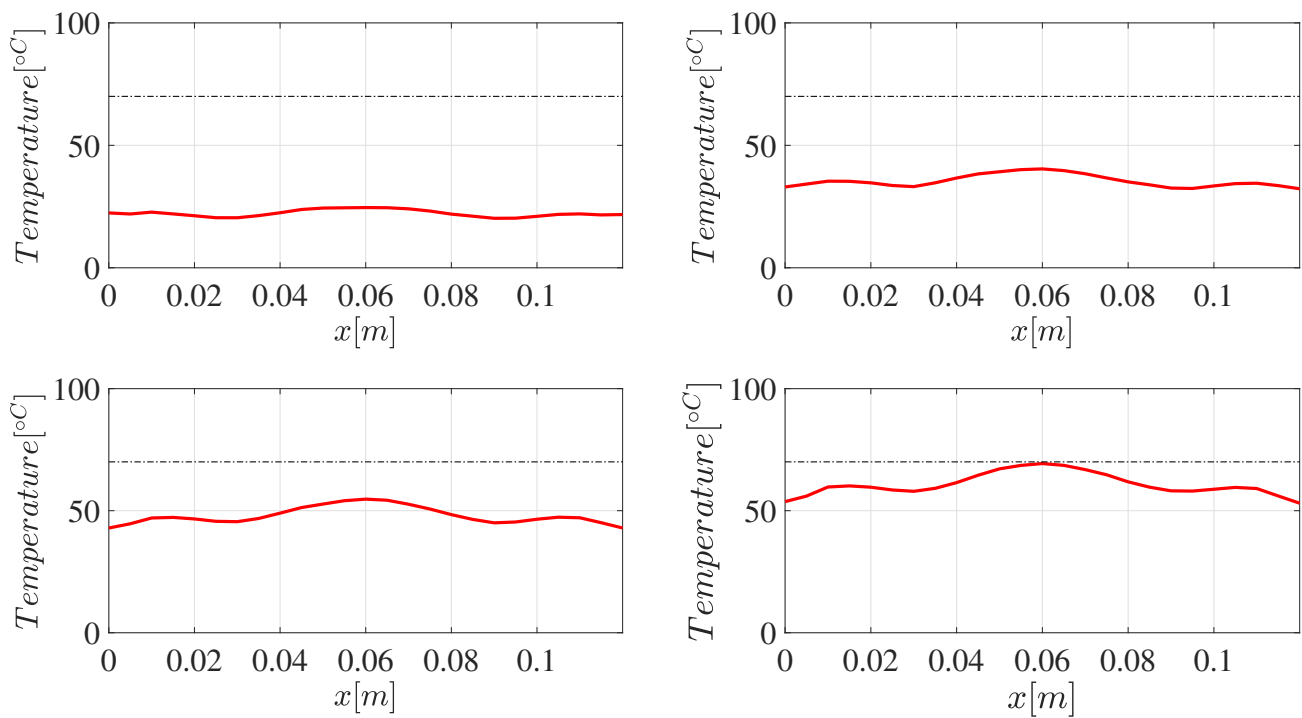


Figure 52: Representation of the temperature profile along the Cut X, with a rotation of $\frac{2\pi}{5}$ radian every 2.5[s], after respectively 75[s], 150[s], 225[s] and 300 [s] of simulation. The black line represent the aimed temperature level of 70°[C].

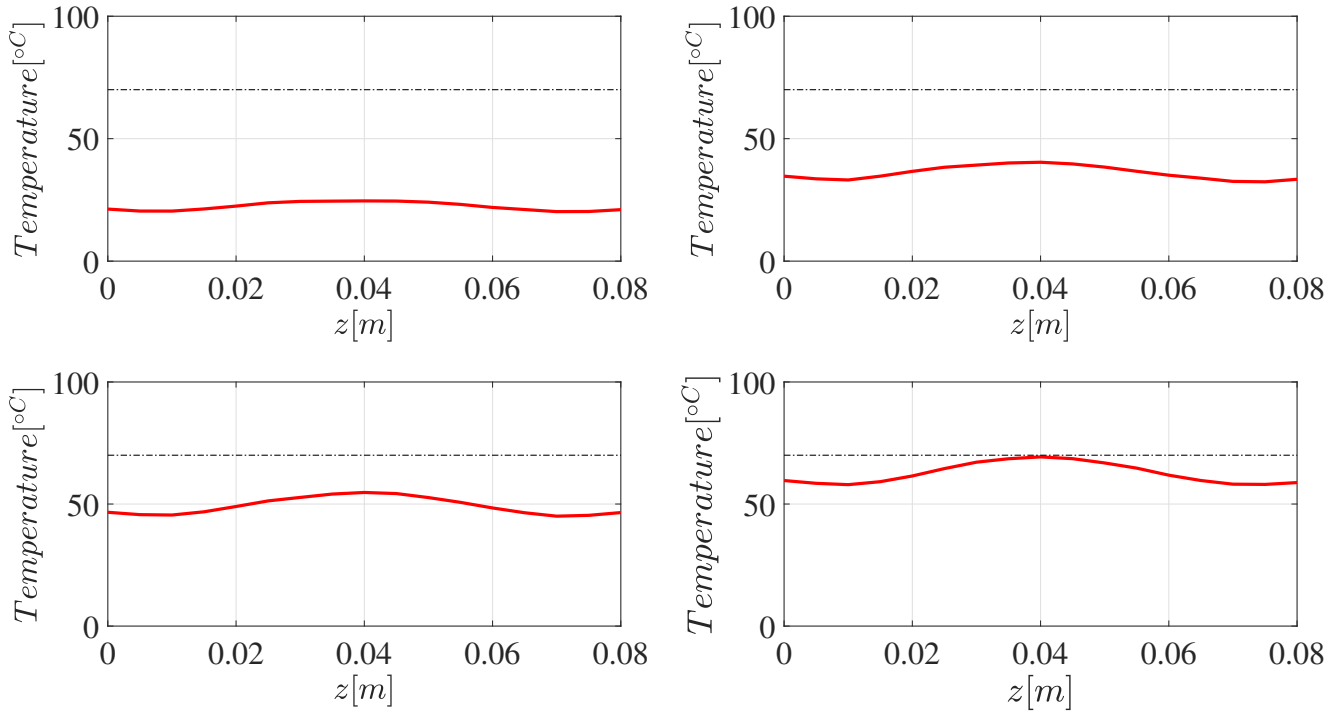


Figure 53: Representation of the temperature profile along the Cut Z , with a rotation of $\frac{2\pi}{5}$ radian every 2.5[s], after respectively 75[s], 150[s], 225[s] and 300 [s] of simulation. The black line represent the aimed temperature level of 70°[C].

This last observation can be explained by the fact that the axis of the bowl is aligned with the axis of rotation. Indeed, in such conditions, considering the revolution symmetry of the food around the axis of rotation and because no phase transition is considered here, the rotation will not induce any modification of the spatial distribution of the electromagnetic properties. Therefore, the spatial distribution of the heat source resulting from the electromagnetic calculation remains the same during the whole simulation. Consequently, the rotation process simply consists in rotating the bowl inside a fixed field of dissipated power. Therefore, if a high dissipated power appears initially close to the center of the bowl (which seems to be the case in FIGURE 49), this high value will remain close to the center during the simulation inducing a more important heating of this zone. An idea to enhance the homogeneity can therefore consist in breaking the revolution symmetry, for instance by pacing the bowl away from the center. This configuration is further discussed in the next section.

Finally, it is also interesting to analyse the time evolution of the temperature at the temporal probe for this case. Indeed, as it can be seen in FIGURE 54, the evolution now presents some small irregularities highlighting the modification of the heat source at this point when time evolves.

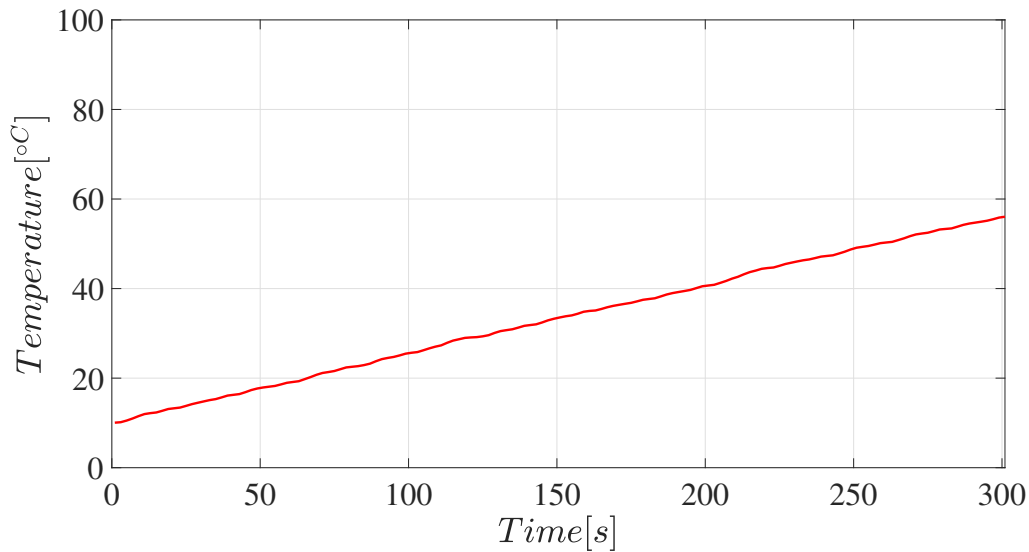


Figure 54: Time evolution of the temperature at the temporal probe placed inside the soup while considering a rotation of $\frac{2\pi}{5}$ radiant every 2.5[s].

4.2 Unfrozen soup not centred

In this section, the exact same bowl of soup is heated using the same microwave oven. The only difference with the previous considered case consists in the initial position of the bowl. Indeed, here the bowl is not centred, as shown in FIGURE 55:

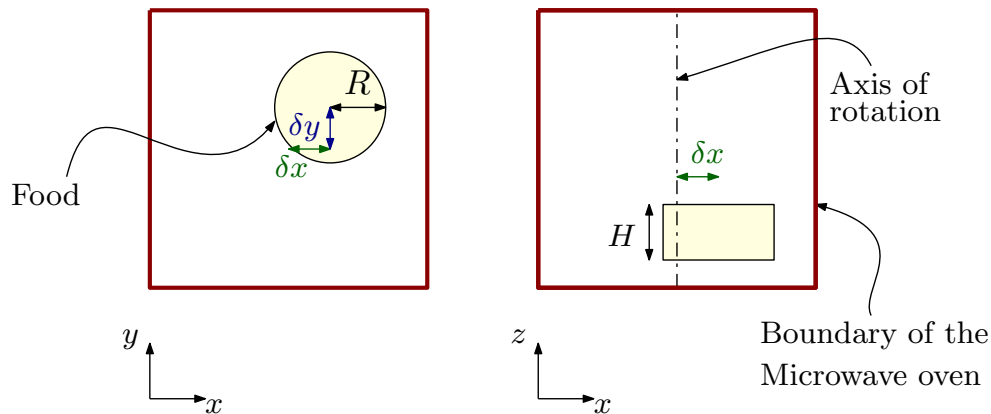


Figure 55: Representation of the geometry when the bowl of soup is not centred inside the microwave oven.

For this simulation the value of δx and δy are both set to 50[mm]. This small shift in the position of the axis of the bowl with respect to the axis of rotation changes quite a lot the way the heating process occurs. Indeed, in such conditions, the spatial distribution of the electromagnetic properties inside the microwave oven is continuously modified by the rotation. Therefore, the dissipated power pattern resulting from the electromagnetic calculation can change quite a lot from one spatial position of the food to the other. Consequently, the evolution of the heat source inside the food becomes quite complex to interpret.

Once again, the evolution of the temperature profile along the two cuts introduced previously is considered. These evolutions are presented in FIGURES 56 and 57

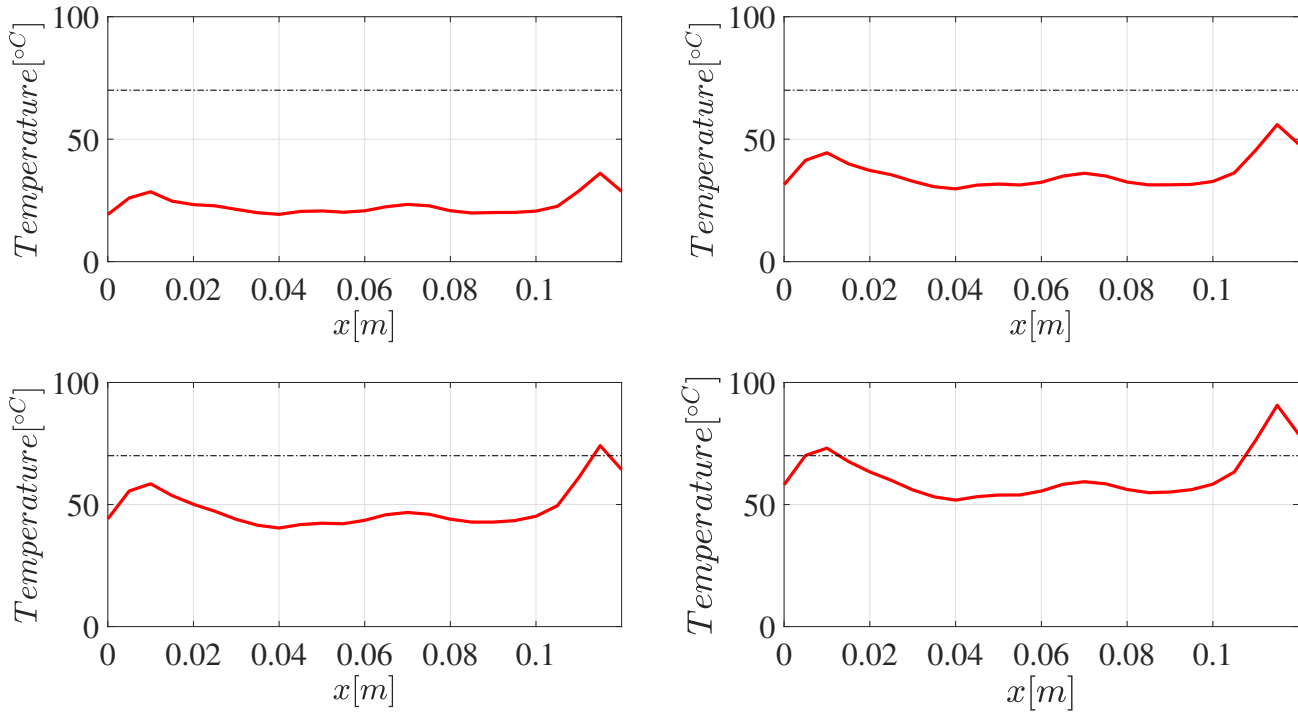


Figure 56: Representation of the temperature profile along the Cut X , with a rotation of $\frac{2\pi}{5}$ radian every 2.5[s], after respectively 75[s], 150[s], 225[s] and 300 [s] of simulation. The black line represent the aimed temperature level of 70°C.

As it can be seen, the temperature profile along the two cuts remains quite homogeneous during the whole simulation except for some points on the circumference of the bowl for which irregularities are still present. However, this time the temperature profile does not present a revolution symmetry.

Therefore, it appears that whatever the initial position of the bowl, heating it in a perfectly homogeneous way is rather difficult to perform using this numerical model of the microwave oven. Indeed, these irregularities could also find their origin in a too rough numerical discretization of the rotation.

Besides this, if these irregularities reveals to be physically correct, it should be highlighted that the temperature rise everywhere in the soup and that the irregularities appear only locally. Consequently, a bowl of soup with homogeneous warm temperature can easily be obtained by mixing the soup when taking the bowl out of the microwave oven.

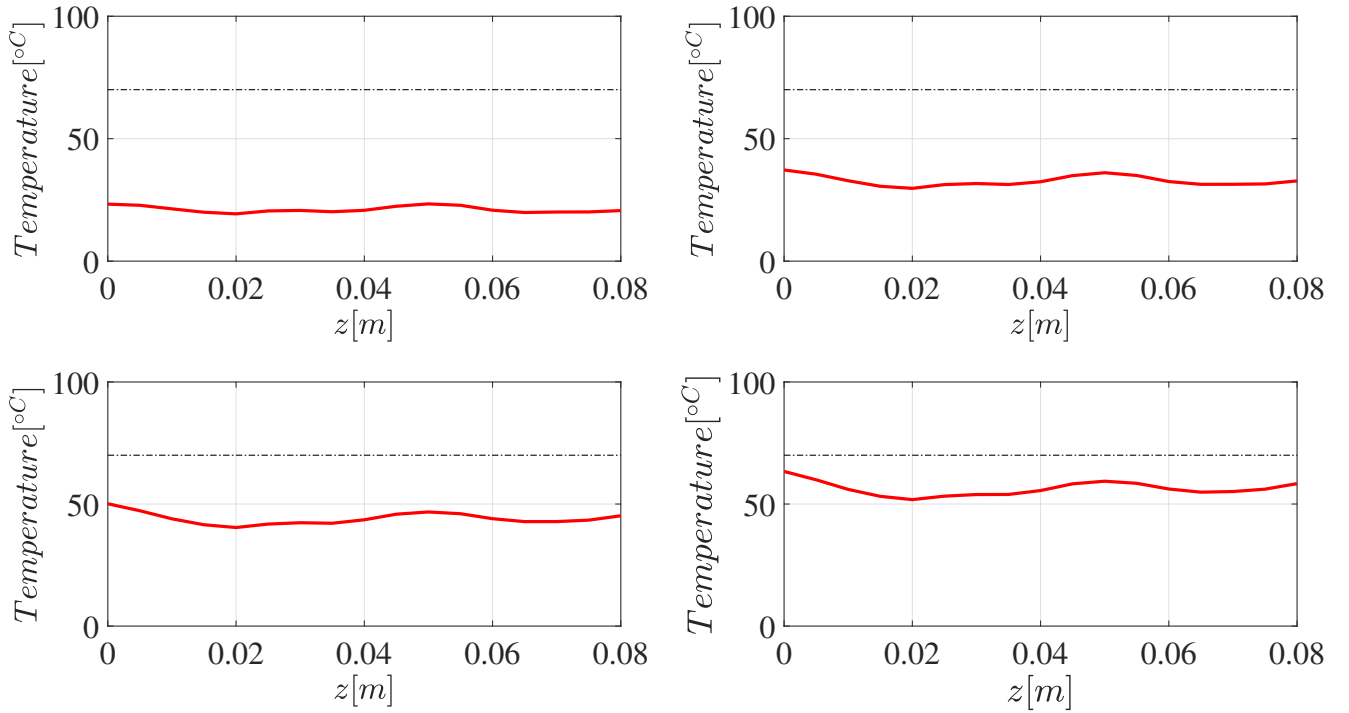


Figure 57: Representation of the temperature profile along the Cut Z , with a rotation of $\frac{2\pi}{5}$ radian every $2.5[s]$, after respectively $75[s]$, $150[s]$, $225[s]$ and $300[s]$ of simulation. The black line represent the aimed temperature level of $70^{\circ}[C]$.

4.3 Frozen soup

In this section, a cylindrical bowl of soup, placed in the centre of the microwave oven, as shown in FIGURE 47, will be studied. It is initially frozen at a temperature of $-5^{\circ}C$. In a similar way as in the previous sections, convective boundary condition are applied on the surface of the food, and the ambient air that surrounds the bowl is set at $20^{\circ}C$. The same input electric field is used. Moreover, the same numerical are used, expect that the simulation is now run for 600 seconds instead. This change is justified by the fact that the frozen soup will indeed heat slower than liquid soup. Furthermore, the order of magnitude of the properties used in the simulation is shown in TABLE 7. Note that, while those orders of magnitude are respected, they were considered to vary with temperature in the numerical simulation.

Frozen		Unfrozen	
ε'	$3.5 [-]$	ε'	$75.8 [-]$
ε''	$0.001 [-]$	ε''	$5 [-]$
ρ	$1000 [kg \cdot m^{-3}]$	ρ	$1000 [kg \cdot m^{-3}]$
c_p	$2000 [J \cdot kg^{-1} \cdot K^{-1}]$	c_p	$4200 [J \cdot kg^{-1} \cdot K^{-1}]$
k	$2.2 [W \cdot m^{-1}]$	k	$0.6 [W \cdot m^{-1}]$

Table 7: Order of magnitude of the electromagnetic and thermal properties of the soup placed in the microwave oven.

From those properties, it can be seen that the heating will be much lower when the soup is frozen. Physically, this can be explained by the fact that liquid water molecules are able to rotate freely due to the electric field, which will in turn lead to the power dissipation, whereas frozen water molecules are locked in the crystal, as shown in FIGURE 58 (rotation would require breaking the bonds between the molecules). Consequently, it is expected that the temperature will first increase near the surfaces, where convection takes place. Moreover, once parts of the food has reached a liquid state, it will heat faster, which will consequently lead to temperature imbalance inside the food, which will add up to the imbalance due to the fact that the soup is also centred in the oven. This behaviour can be recovered in the numerical model.

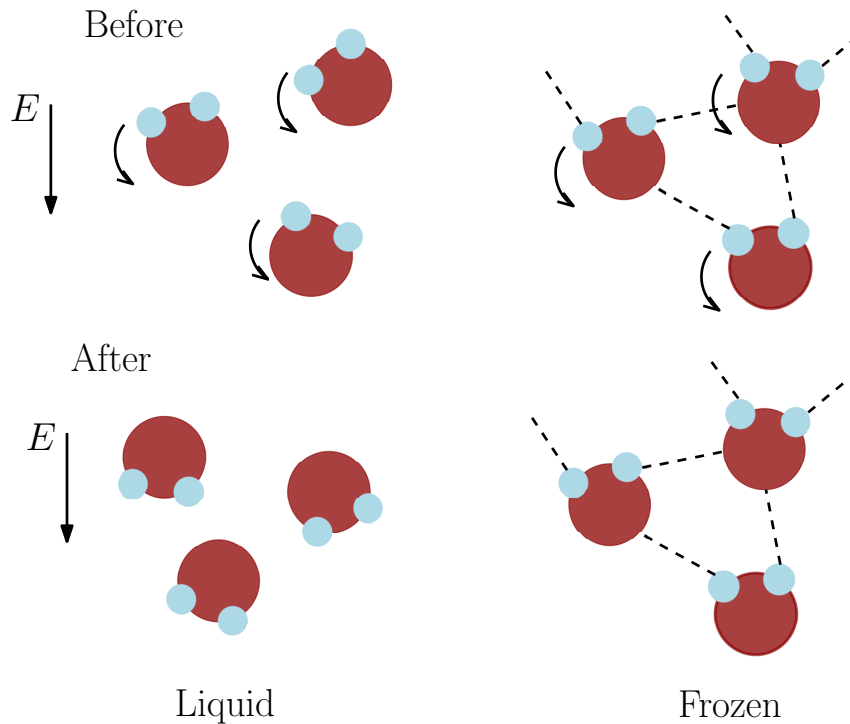


Figure 58: Water and ice molecules under a vertical electric field. The red spheres are hydrogen atoms and the blue spheres are oxygen atoms. The dotted line represents the bonds between the molecules.

FIGURES 59 and 60 show the temperature profile along a x cut and a z cut, respectively. Since the heating resulting from the dissipation inside the food in the frozen material is relatively small due to the thermal properties, the change in temperature is mainly due to convection with the ambient air inside the oven, which explains why the temperature only increases near the sides of the material. However, once phase transition has occurred, the power dissipated inside the food increases in a non negligible way, which explains the shape of the curve. Moreover, since the food is centred inside the oven, unevenness in term of heating of the food in liquid state also occurs, as studied previously.

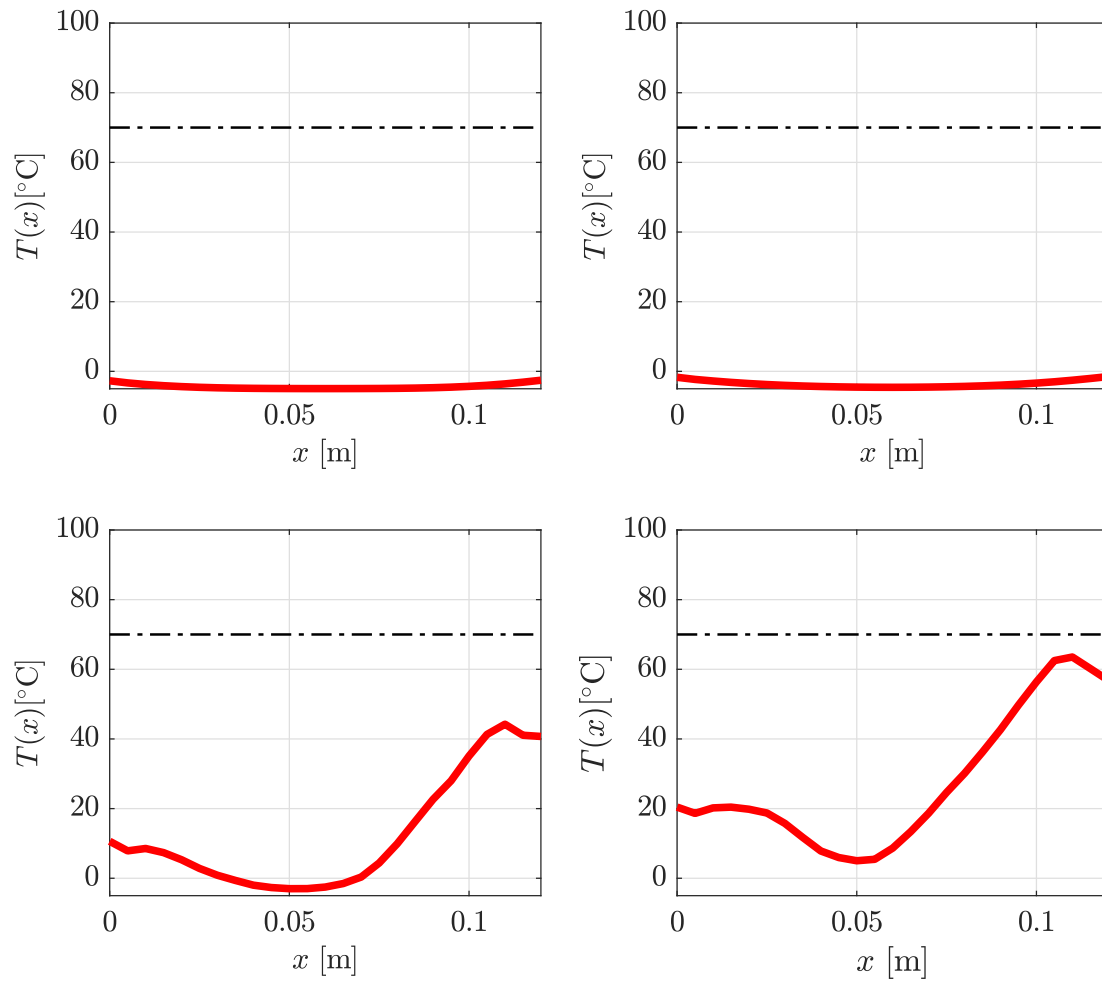


Figure 59: Representation of the temperature profile along the Cut X , with a rotation of $\frac{\pi}{5}$ radian every $5[s]$, after respectively $75[s]$, $300[s]$, $512[s]$ and $600[s]$ of simulation. The black line represent the aimed temperature level of 70°C .

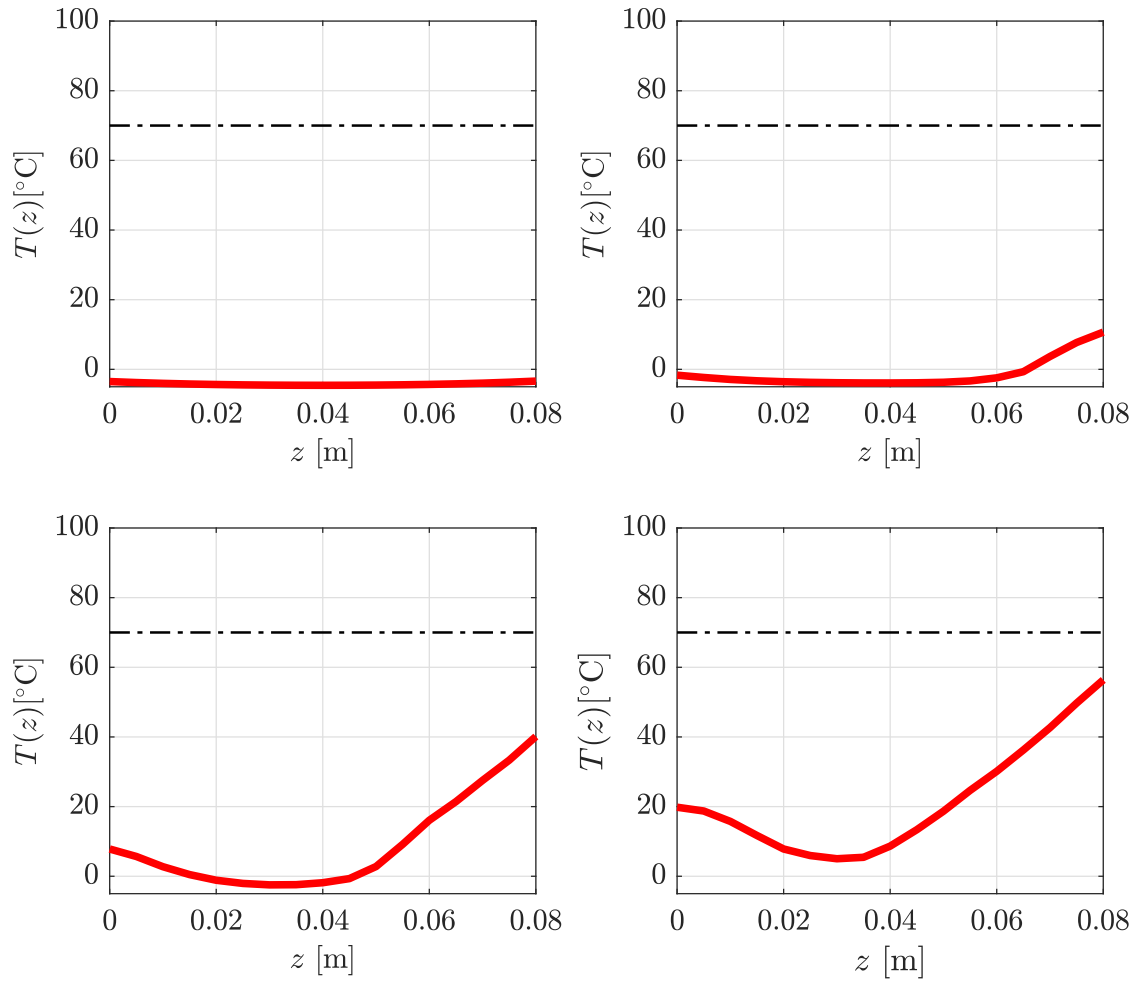
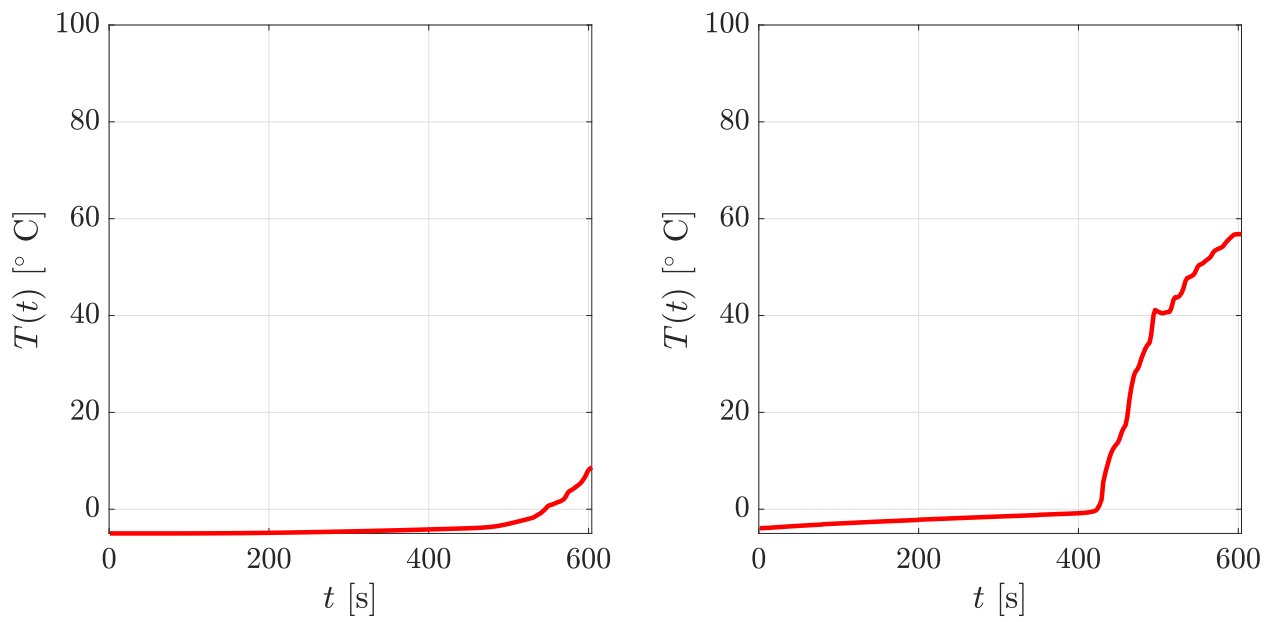


Figure 60: Representation of the temperature profile along the Cut Z , with a rotation of $\frac{\pi}{5}$ radian every 5[s], after respectively 75[s], 300[s], 512[s] and 600 [s] of simulation. The black line represent the aimed temperature level of 70°C.

For instance, FIGURE 61 shows the evolution of the temperature in time for a point located in the middle of the material, and for a point located at the far right. As expected, phase transition occurs faster in the side of the food, compared to a point in the middle, which will in turn results in a greater temperature.

In conclusion, heating frozen water (soup) inside a microwave oven does not work properly. Indeed, some part of the food will remain frozen, while some other will heat up fast due to the phase transition. This kind of result can easily be observed in "homemade" experiments by heating a glass of frozen water in a microwave oven: some parts will still be frozen, while others will already have reached the boiling temperature. In practice, microwave ovens possess a particular mode dedicated to the heating of frozen food, which, for instance, includes periodical stopping in the microwave heating to let the temperature homogenise inside the food.



(a) Point located in the middle of the material. (b) Point located in the right side of the material

Figure 61: Time evolution of the temperature at the temporal probe placed inside the soup while considering a rotation of $\frac{\pi}{5}$ radian every 5[s].

4.4 Heating of a chicken

Finally, a last section is dedicated to the simulation of the heating of a much more complex food.

Indeed, in this section, the food of interest placed inside the oven is a chicken whose geometry is more elaborated than the geometry of the bowl of soup. On the top of that, the electromagnetic and thermal properties are not constant inside the chicken. Indeed, it is considered that the chicken is made of fat, muscles and bones. The exact considered geometry and constitution of the chicken is presented in FIGURE 62:

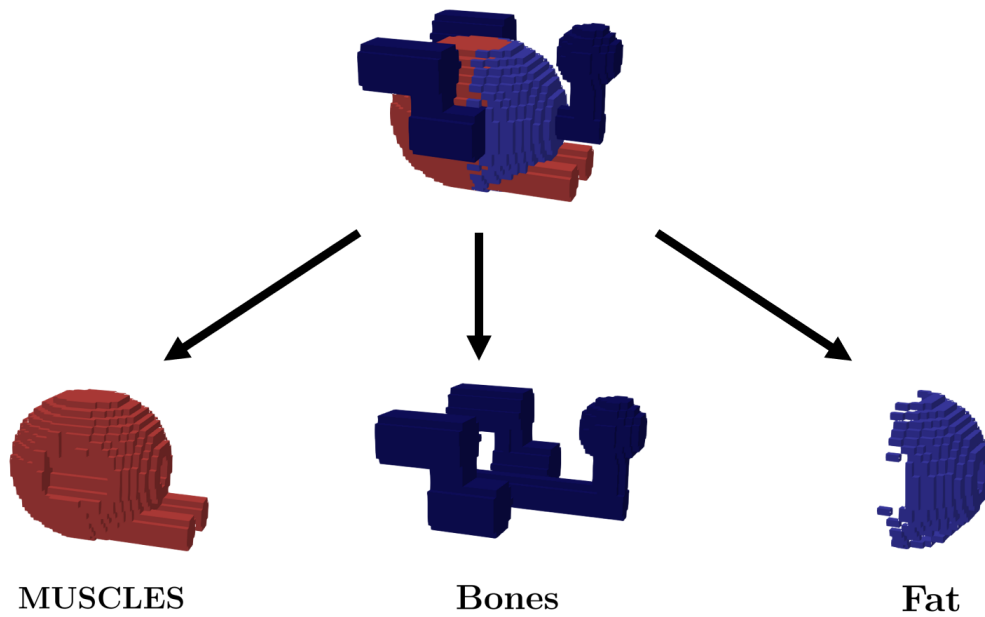


Figure 62: Representation of the geometry and constitution of the chicken.

It should be highlighted that this geometry and distribution of fat, muscles and bones have been obtained by assembling 10 cylinders and 4 spheres, which explains the quite rough approximation of the reality. Nevertheless, one could obtain a more satisfying geometry by dividing the chicken into more smaller geometries. However, the point here is only to highlight that the implementation is able to deal with such division of the geometry.

The parameters used for the fat, muscles and bones are presented in TABLE 8:

	ε' [-]	ε'' [-]	k [$W \cdot K^{-1} \cdot m^{-3}$]	ρ [$kg \cdot m^{-3}$]	c_p [$J \cdot kg^{-1} \cdot K^{-1}$]
Muscles	59.002	54.28	0.478	1059.9	3421
Bones	11.345	2.904	0.58	1750	440
Fat	5.56	2.29	0.201	909.4	2348

Table 8: Electromagnetic and thermal properties of the fat, muscles and bones.

A 300 [s] simulation was run using this geometry and properties, the chicken initial temperature was also set to 10 [°C]. The obtained temperature field at the surface and inside the chicken is presented in FIGURE 63:

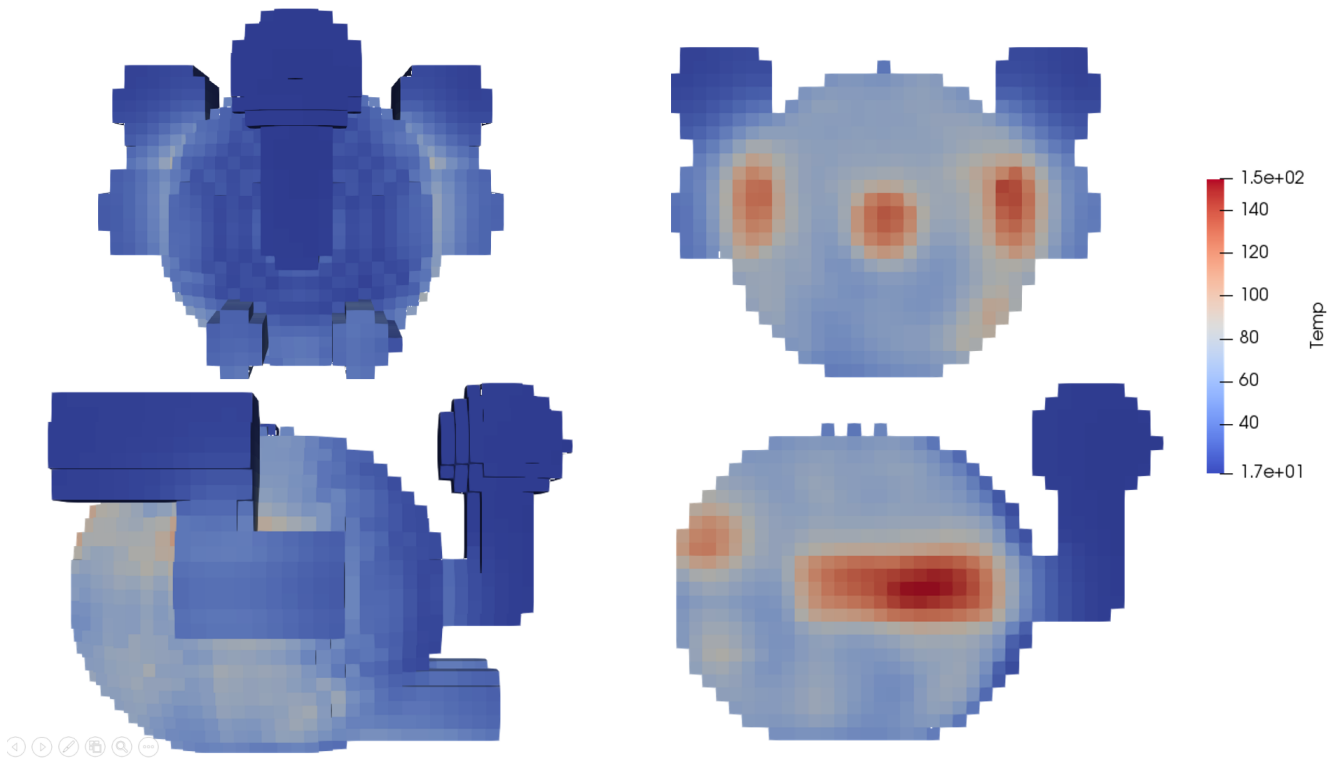


Figure 63: Temperature field at the surface and inside the chicken after a 300 [s] simulation.

Therefore, it appears that the whole chicken heat up during the simulation. However, it can also be observed that this heating is highly non homogeneous highlighting both the non homogeneity of the heat source and the non homogeneity of the food properties.

Conclusion

The goal of this project was to build a parallel solver able to model the behaviour of a microwave oven, under some assumptions (*e.g.* no Joule losses). It required going through three main steps that consisted in, respectively, building an electromagnetic solver that solves Maxwell's equations in a cavity, a thermal solver for the heat equation inside the food, and handling the rotation of the food inside the oven.

In the first part, an electromagnetic solver was developed using a FDTD method. The solver was tested and validated thanks to several test cases such as the propagation of a wave inside a cavity, or a wave going through two media. Those test cases were chosen because they are relevant for the physics inside a microwave oven while allowing the validation of the model. Finally, performances and stability of the model were also studied. An acceptable speed up was found using MPI, although the speed up with OpenMP is not optimal.

In the second part, a solver for the heat equation was developed using a semi implicit finite difference scheme. The stability, as well as the order of convergence of the scheme were studied. Furthermore, several test cases involving, for instance, transient heat conduction inside a body. Finally, performances of the model were analysed. It was found that the speed up obtained by increasing the number of MPI processes is rather bad, which seems to be caused by MUMPS.

The last part of the development was the coupling between the two solvers. It consisted in computing the dissipated power inside the food using the electromagnetic solver, and using this information as a heat source in the heat equation solver. In order to achieve this calculation, a steady-state criterion was established. Moreover, since the properties of the matter change, the coupled solver was also given the ability to handle phase transition, or more generally, temperature dependant properties. Finally, to correctly model the behaviour of a microwave oven, the rotation of the food was implemented.

Finally, test cases involving the two physics were run. In particular, the heating of a bowl of soup (modelled as water for convenience), as well as a chicken were studied.

All in all, the coupled solver yields convincing results despite some simplifying assumptions. Improvements could be made by relaxing some of those assumptions. For instance, by taking into account Joule losses, which is discussed in appendix. Further improvement in the complexity of the geometry inside the oven could also be made.

Appendix

Dissipative electromagnetic numerical scheme

As it has been mentioned in the development of the electromagnetic solver, the chosen numerical scheme does not take into account any dissipation of the electromagnetic energy. As it has also already been said, this assumption is equivalent to consider that the electrical conductivity of the medium in which the electromagnetic signal propagates is equal to zero.

Therefore, the electromagnetic solver can possibly be improved by introducing the Joule losses in the numerical scheme. In order to do this, a convenient hypothesis consists in considering that the medium is a conductor of conductivity σ (possibly non constant in space and time). Therefore, it allows us to write:

$$J = \sigma E.$$

If this term is not neglected anymore in Maxwell's equation, the update equation for the electromagnetic fields needs to be modified and become more complex. As an illustration, the update equation z component of the electric field [3]:

$$Ez_{i,j,k+\frac{1}{2}}^{n+1} = \frac{2dt}{(2\varepsilon + \sigma dt) \cdot dx} \left[\left(Hy_{i+\frac{1}{2},j,k+\frac{1}{2}}^{n+\frac{1}{2}} - Hy_{i-\frac{1}{2},j,k+\frac{1}{2}}^{n+\frac{1}{2}} \right) - \left(Hx_{i,j+\frac{1}{2},k+\frac{1}{2}}^{n+\frac{1}{2}} - Hx_{i,j-\frac{1}{2},k+\frac{1}{2}}^{n+\frac{1}{2}} \right) \right] \\ + \frac{2\varepsilon - \sigma dt}{2\varepsilon + \sigma dt} Ez_{i,j,k+\frac{1}{2}}^n,$$

Therefore, it appears that the update equations are not modified that much as the term involved remain the same and only the coefficient are slightly different. Nevertheless, it should be highlighted that a new grid for σ will be required if this quantity is not constant over the spatial domain.

Running a test

Several input files are required in order to run a test. To simplify things, only the directory containing those files is needed as an argument when launching the solver. Note that output files are saved in the current working directory. For instance, if the `bin` directory contains the executable, as well as a directory called `InputFiles` and `Results`, one should launch the test from the `Results` directory as follows:

```
mpirun -np 8 ../CoupledSolver ../InputFiles
```

Description of the input files

`Interface.dat`

L_x – length (cavity)
 L_y – width (cavity)
 L_z – height (cavity)
 f – frequency
 Δx – electromagnetic grid spacing
 Δt – electromagnetic time increment
 t_f – Final time of the whole simulation
 P – (1: waveguide; 2: only E_y variable; 3: only E_y constant; 4: 'waveguide' with only E_y)
Sampling rate
 $L_{a,x}$ – length of the antenna
 $L_{a,y}$ – width of the antenna
 $L_{a,z}$ – height of the antenna
 x_a – x coordinate of the antenna's center
 y_a – y coordinate of the antenna's center
 z_a – z coordinate of the antenna's center
Number of sphere
Number of cylinder
Number of cube
 E_0 – input electric field
 $\Delta\theta$ – Angle increment for the rotation
Solve electro ? – 0 = no; 1 = yes

`param_heat.dat`

L_x – length (thermal domain)
 L_y – width (thermal domain)
 L_z – height (thermal domain)
 Δx – thermal grid spacing
 Δt – thermal time increment
 t_f – Final time of the thermal simulation

Number of sources
 Number of objects (sphere, cube, cylinder)
 Boundary condition: y_0
 Boundary condition: y_1
 Boundary condition: z_0 – 1 if Dirichlet, 0 if Neumann
 Boundary condition: z_1
 Boundary condition: x_0
 Boundary condition: x_1
 TEMP Dirichlet Y0
 TEMP Dirichlet Y1
 TEMP Dirichlet Z0 – If there is no Dirichlet BC, the value does not matter
 TEMP Dirichlet Z1
 TEMP Dirichlet X0
 TEMP Dirichlet X1
 TEMP initial – Not used, set it to 0
 k_e – heat conductivity of environment
 ρ_e – density of environment
 $c_{p,e}$ – specific heat capacity of environment
 Sampling rate
 θ – determine if the scheme is explicit of implicit, $\theta \in [0, 1]$
 Number of sphere
 Number of cylinder – not used since the coupling, it is done in Interface.dat
 Number of cube
 $T_{f,i}$ – initial temperature of the food
 h_{air} – convective coefficient of air
 x_{\min} –
 y_{\min} –
 z_{\min} –
 Δx_e – electromagnetic grid spacing L_x – length (cavity)
 L_y – width (cavity)
 L_z – height (cavity)
 Solve thermo ? – 0 = no; 1 = yes
 Transient ? – 1 if transient; 0 if steady state

Prop_cube.dat

L_x – length (cube)
 L_y – width (cube)
 L_z – height (cube)
 x – x coordinate of the centre
 y – y coordinate of the centre
 z – z coordinate of the centre
 Material ID

Prop_cylinder.dat

Axis of the cylinder : (0-> x ;1-> y ;2-> z)
 x - x coordinate of the centre
 y - y coordinate of the centre
 z - z coordinate of the centre
 R - radius
Material ID
 H - height/length

Prop_sphere.dat

x - x coordinate of the centre
 y - y coordinate of the centre
 z - z coordinate of the centre
 R - radius
Material ID

Spatial_cut.dat

Cut along x ? - no = 0; yes = 1
 y - y coordinate of the cut
 z - z coordinate of the cut
Cut along y ? - no = 0; yes = 1
 x - x coordinate of the cut
 z - z coordinate of the cut
Cut along z ? - no = 0; yes = 1
 x - x coordinate of the cut
 y - y coordinate of the cut
Number of cuts
Time for cut 1
 \vdots
Time for cut n

Spatial_cut_temp.dat

Cut along x ? - no = 0; yes = 1
 y - y coordinate of the cut
 z - z coordinate of the cut

Cut along y ? – no = 0; yes = 1
 $x - x$ coordinate of the cut
 $z - z$ coordinate of the cut
 Cut along z ? – no = 0; yes = 1
 $x - x$ coordinate of the cut
 $y - y$ coordinate of the cut
 Number of cuts
 Time for cut 1
 \vdots
 Time for cut n

prop_source_heat.dat

L_x – length of the source
 L_y – width of the source
 L_z – height of the source
 $x - x$ coordinate of the centre
 $y - y$ coordinate of the centre
 $z - z$ coordinate of the centre
 Q – value of the heat source [W/m³]

Temporal_probe.dat

Number of probe(s)
 $x_1 - x$ coordinate of the first probe
 $y_1 - y$ coordinate of the first probe
 $z_1 - z$ coordinate of the first probe
 \vdots
 $x_n - x$ coordinate of the n^{th} probe
 $y_n - y$ coordinate of the n^{th} probe
 $z_n - z$ coordinate of the n^{th} probe

temp_probe_electro.dat

Number of probe(s)
 $x_1 - x$ coordinate of the first probe
 $y_1 - y$ coordinate of the first probe
 $z_1 - z$ coordinate of the first probe
 \vdots

x_n – x coordinate of the n^{th} probe
 y_n – y coordinate of the n^{th} probe
 z_n – z coordinate of the n^{th} probe

Save_Data.dat

Export E_x ?
 Export E_y ?
 Export E_z ? – export vti files for Paraview
 Export H_x ? – no = 0, yes = 1
 Export H_y ?
 Export H_z ?

List of materials

ID	Material
0	Air
1	Water
2	Basil fried chicken [4]
3	Non-physical material $\alpha = 1$
4	Non-physical material $\alpha = 2$
5	Non-physical material $\alpha = 1$
6	Chicken bones
7	Chicken fat
8	Chicken muscle
9	Non-physical material $\alpha = 0.0002$
10	Non-physical material $\varepsilon' = 9$

Table 9: List of materials and their associated ID that is used in the input files

Bibliography

- [1] Kane S. Yee. Numerical solution of initial boundary value problems involving maxwell's equations in isotropic media. *IEEE*, AP-14(3), 1966.
- [2] Vanderheyden B. *Electromagnétisme*.
- [3] Umran S. Inan and Robert A. Marshall. *Numerical Electromagnetics: The FDTD Method*, pages 88–91. Cambridge University Press, 2011.
- [4] Waraporn Klinbun and Phadungsak Rattanadecho. An investigation of the dielectric and thermal properties of frozen foods over a temperature from -18 to 80 °c. *International Journal of Food Properties*, 20(2):455–464, 2017.
- [5] Olver P. *Introduction to Partial Differential Equations*, pages 121–179. 2014.
- [6] Incropera F. Dewitt D. Bergman T. and Lavine A. *Foundations of Heat Transfer*. 2013.
- [7] Aarnst M. and Boman R. *Modelling with partial differential equations*.
- [8] H.P. Schwan. Complex permittivity of water at 25° c. *Physics today*, 64(5), 1976.
- [9] Subbiah J. Jones D. Pitchai K., Birla S.L. and Thippareddi H. Coupled electromagnetic and heat transfer model for microwave heating in domestic ovens. *Journal of food engineering*, 112, 2012.
- [10] Charmon S. *Développement d'un four micro-ondes monomode et frittage de poudre céramique et métallique*. Mécanique [physics.med-ph]. Institut National Polytechnique de Grenoble - INPG, 2009. Français. <tel-00579922>.
- [11] Holmes K. *Thermal properties*. <http://users.ece.utexas.edu/~valvano/research/Thermal.pdf>.
- [12] Davidson S. James D. *Medical Engineering Physics Volume 22, Issue 10, December 2000, Pages 741-747*. <https://www.sciencedirect.com/science/article/pii/S1350453301000030>.
- [13] Andreuccetti D. *Calculation of the Dielectric Properties of Body Tissues in the frequency range 10 Hz - 100 GHz*. <http://niremf.ifac.cnr.it>.
- [14] US National Library of Medicine Medical Subject Headings. *Bone density*. https://en.wikipedia.org/wiki/Bone_density.

- [15] Yang J. *Densities of Different Body Matter: Fat density*. <http://www.scrollseek.com/training/densitiesofdifferentbodymatter.html>.
- [16] ITIS Foundation. *Tissue properties*. <https://www.itis.ethz.ch/virtual-population/tissue-properties/database/heat-capacity/>.
- [17] Evans P. *Specific heat capacity of materials*. <http://theengineeringmindset.com/specific-heat-capacity-of-materials/>.
- [18] Rungnaphar Pongsawatmanit, Osato Miyawaki, and Toshimasa Yano. Measurement of the thermal conductivity of unfrozen and frozen food materials by a steady state method with coaxial dual-cylinder apparatus. *Bioscience, Biotechnology, and Biochemistry*, 57(7):1072–1076, 1993. PMID: 27280988.
- [19] C Matzler and U Wegmuller. Dielectric properties of freshwater ice at microwave frequencies. *Journal of Physics D: Applied Physics*, 20(12):1623, 1987.